Three-Dimensional Simulation of Coating Build-up
In Suspension Plasma Spray Process

Siavash Ghafouri Azar

A Thesis

In

The Department

of

Mechanical, Industrial and Aerospace Engineering

Presented in Partial Fulfillment of the Requirements

For the Degree of

Master of Applied Science (Mechanical Engineering) at

Concordia University

Montreal, Quebec, Canada

December 2018

CONCORDIA UNIVERSITY
School of Graduate Studies

This is to certify that the thesis prepared

By: Siavash Ghafouri Azar

Entitled: Three-Dimensional Simulation of Coating Build-up In Suspension Plasma Spray Process

and submitted in partial fulfillment of the requirements for the degree of

<div align="center">

Master of Applied Science (Mechanical Engineering)

</div>

complies with the regulations of the University and meets the accepted standards with respect to originality and quality.

Signed by the final examining committee:

    _____ Chair

    M.Paraschivoiu

    _____ Examiner

    R.Wuthrich

    _____ Examiner

    A. Dolatabadi and C. Moreau

    _____ Thesis Supervisor(s)

    _____

Approved by _____

       Chair of Department or Graduate Program Director

_____

       Dean,

Date _____

Abstract

Thermal spray technology is widely used in many industries. The most important purposes of applying coatings are improving functional performance by the ability to work at higher temperature, increasing component life by protecting the surface against degradation, and repairing worn parts without changing the properties of the main part. Nano-structured coatings, which show improved characteristics as compared to conventional ones, have been extensively studied over the recent years. Suspension plasma spray (SPS) is a recently developed process that can produce nano-structured coatings on large surfaces. The technique involves spraying fine molten particles that solidify rapidly in contact with the substrate with grain size less than 100 nm. A suspension of sub-micron or nano-sized particles in a liquid carrier (water and ethanol) is injected in and atomized by the high speed high temperature plasma plume in a DC plasma spray torch. The SPS technique allows us to deposit micron-size particles more efficiently and creates fine grains, and small-sized pore microstructure. The microstructure of SPS coatings results from a series of complicated phenomena influenced by several parameters. Thus, depending on the suspension interaction with the plasma plume, powder types, solid concentration in suspension, substrate preparation method, plasma spray setup, spray distance, powder feed rate, etc. various microstructures can be obtained. Therefore, it is of great interest to predict the SPS coating microstructure within the context of particle conditions upon impact i.e. trajectory, size, and velocity. To understand how the microstructure of SPS coatings relates to particle conditions and predict coating attributes such as porosity, columnar structure, thickness and surface roughness, a three-dimensional predictive model for coating buildup on a

substrate has been developed.

In this model, the impact properties of each particle that comprise size, velocity, temperature, as well as particle's location near substrate are obtained from a computational fluid dynamics (CFD) model simulating the SPS process using a commercial Oerlikon Metco 3MB plasma torch.

Subsequently, the trajectory of each particle close to the substrate surface is calculated to determine its final impact location on the substrate or previously deposited particles. It is assumed that particles stick at the impact location according to some prescribed scenarios. The coating structure is specified using a variable f(i,j,k) which is zero when the cell is empty and equals unity when the cell is filled with the spray material. The numerical results can capture the columnar structures observed in SPS coatings due to the shadow effect.

Acknowledgments

First of all, I would like to express my special appreciation and thanks to my advisors, Professors Ali Dolatabadi and Christian Moreau, who taught me dedication and hard work. It was a privilege for me to work under your supervision with your impressive support and encouragements throughout my studies at Concordia University and also helped me along my path to a professional life that words   could never be enough to express my gratitude. I would also like to express my appreciation to my colleagues and friends, Dr. Ghobad Amini, Dr. Mehdi Jadidi, Sara Mamani, and Mohammad Karamzadeh, for their support and precious friendship. Last but not least, my deepest thanks goes   to my parents Majid and Lili for their unconditional support in my life. You are awesome. Also,   I must thank my lovely brothers and sister.

Dedicated to my parents

Majid & Lili

My sister & brothers

Arezou & Dariush & Reza

Contents

List of Figures

List of Tables

Nomenclature

SPS	Suspension plasma spray
APS	Air plasma spray
$\rho_l v_l^2$	Momentum flux of liquid
$\rho_g v_g^2$	Momentum flux of plasma jet
Re	Reynolds number
We	Weber number
ρ_l	Droplet density
μ_l	Kinematic viscosity
v	Velocity
D	Diameter
γ	Surface tension
St	Stokes number
μ_g	gas kinematic viscosity
K	Sommerfeld number
a	Ratio of the maximum flattening velocity to the impact velocity
ξ	Ratio of the maximum diameter to initial diameter
D_{MAX}	Maximum diameter
$D_{initial}$	Initial diameter
P	Impact number
$v_{\parallel}$	Lateral velocity
$v\perp$	Normal velocity
t	Time
e	Coating thickness
D	Coating mean diameter
d_p	Mean particle diameter
h	Mean disk thickness
$f_{i,j,k}$	Color code variable

1 Introduction

1.1 Thermal spray

Coating technologies have been widely employed in many industries including aerospace, biomedical, oil, and gas, nuclear, etc. The most important purposes of applying coatings are improving functional performance by the ability to work at higher temperature, increasing component life by protecting the surface against corrosion, and repairing the worn parts without changing the properties of the main parts [1]. There are numerous coating technologies among which our focus is on thermal spray. ASM Thermal Spray Society defines the thermal spraying term as "a group of processes in which finely divided metallic or non- metallic surfacing materials are deposited in a molten or semi-molten condition on a substrate to form a spray deposit in which the surfacing material may be in the form of powder, rod, cord, or wire" [2]. The torch, as the main system component provides the energy required for heating, melting, and accelerating the material by heating the stream of gases.

The torch energy source could be, combustion, electrical discharge or high–pressure gases [1]. An electrical discharge is the energy source for heating the gas in plasma-based processes comprising plasma spraying, plasma transferred arc, and wire arc spraying. Due to few limitations on used materials and substrate shapes, plasma spray is the most flexible method among other thermal spray methods [1]. Figure 1-1 illustrates the thermal spray process using a plasma spray torch. As depicted, the plasma gas is heated by an electric arc which is struck between the electrodes consisting of a cylindrical copper anode and a rod-type or button-type thoriated tungsten cathode. Depending on operating parameters and torch design, the plasma gas at the exit of the torch can reach temperatures and velocities between 12000 and 15000 K

and between 500 to 2500 m/s, respectively. The plasma gas is typically a mixture of two or three pure gases such as Ar, He, H2 or N2 comprising usually a primary heavy gas (e.g. Ar) for flow and catch the particle and a secondary gas (e.g. He or H2) to enhance heat transfer to the particles [3].
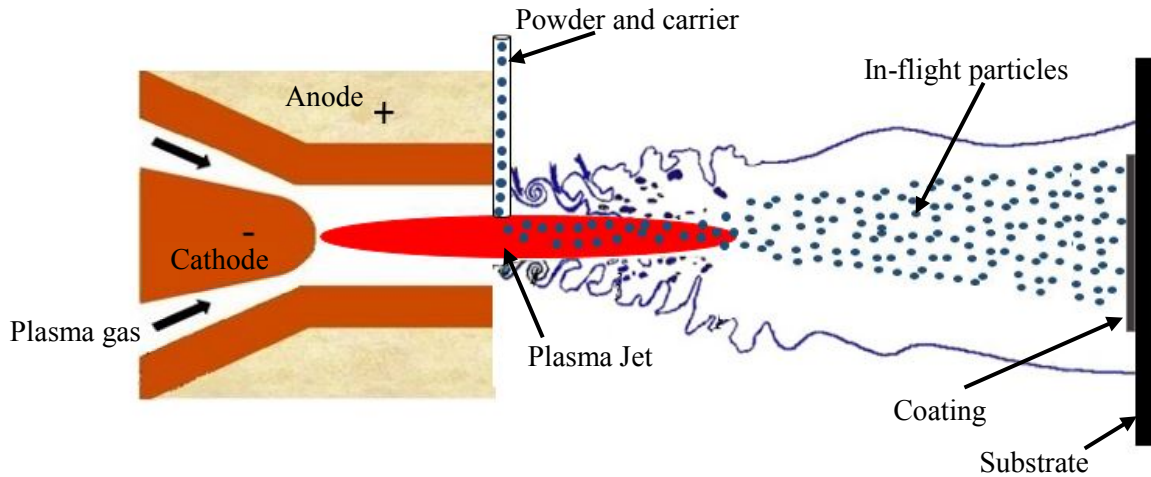
Figure 1-1 Schematic of a typical plasma torch.

The injected powder size at the exit of the plasma torch is an influential factor for the coating quality and should be chosen based on the type of materials and their melting points. Powder size is typically in the range of 10 to 110 μm depending on the application. The powder is injected into the plama jet radially or axially [1].

1.2 Suspension plasma spray (SPS)

The two conventional techniques used for thermal barrier coatings are electron-beam physical vapor deposition (EB-PVD) process and air plasma spray (APS). The coatings structure produced by both of these methods are different due to different deposition principles. In comparison to APS, the EB-PVD technique offers better mechanical properties and durability, as it produces columnar-structured coatings and these columnar grains are separated by inter-columnar gaps. On the

2

other hand, compared to EB-PVD coatings, APS offers coatings with lower cost and better process flexibility. Thus, developing a new process which fabricates the coatings with columnar structure similar to EB-PVD and lower thermal conductivity similar to APS is necessary [4].

Since the nano-structured coatings have lower thermal conductivity and higher thermal stability relative to conventional methods, it has been dramatically used over recent years [1]. Decreasing the powder size improves the properties of TBC. However, it is very difficult to use the conventional technique in spraying the fine particle less than 5 μm due to poor flowability, clogging in the feed lines and difficult to inject in plasma flow. The suspension plasma spray (SPS) as one of the techniques to overcome this problem is based on the suspension of the sub-micron or nano-sized particles in a liquid carrier (water and ethanol) and injecting to the plasma jet or flame. The SPS technique allows us to deposit sub-micron particles more efficiently and create fine grains as well as small-sized porosity microstructure [5]. Due to the low mass of such particles, the carrier gas should be replaced by liquid one. In fact, liquid carrier gives the required momentum to droplets in order to penetrate into the plasma. If the momentum flux of liquid ($\rho_l v_l^2$) is larger than the momentum flux of plasma jet ($\rho_g v_g^2$), the drops penetrate inside the plasma [6].

The nano-structured coatings can be fabricated using liquid carrier based process so called suspension plasma spray (SPS). The structure layers involved in SPS form thinner splats. Therefore, the number of lamellas is higher than that produced by APS, as illustrated in Figure 1-2 which can result in decreasing the thermal conductivity of the coatings produced by SPS process [7].
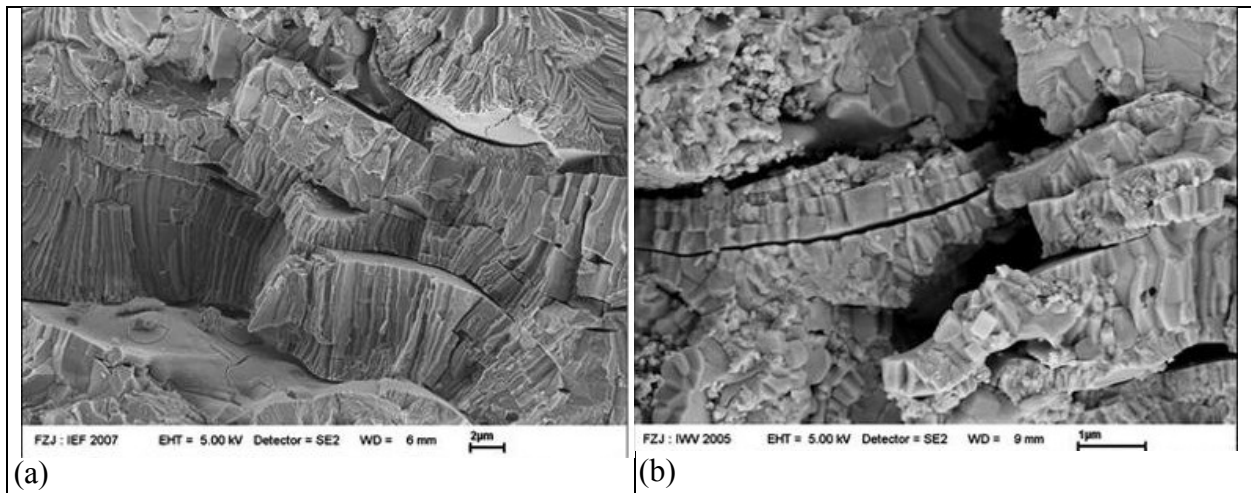
Figure 1-2 Standard coating structure of, (a) air plasma spray (APS), (b) suspension plasma spray (SPS) [8].

The transport of the suspension into the plasma flow and suspension droplet evolution are complex phenomena as illustrated in Figure 1-3. After the injection of suspension and its fragmentation from a continuous liquid jet to large drops (primary break-up) and atomization of the large drops to smaller ones (secondary break-up), the droplet diameter starts to decrease due to the evaporation of liquid. The interaction of the suspension with the plasma jet leads to the local reduction of the flame temperature. Then, the submicron particles are accelerated, heated up and melted by the flame prior to impact on the substrate as seen in Figure 1-4 [9]. The standoff distance in SPS relative to APS is significantly smaller in order to prevent re-solidification of the molten particles before their impact on the substrate [10].
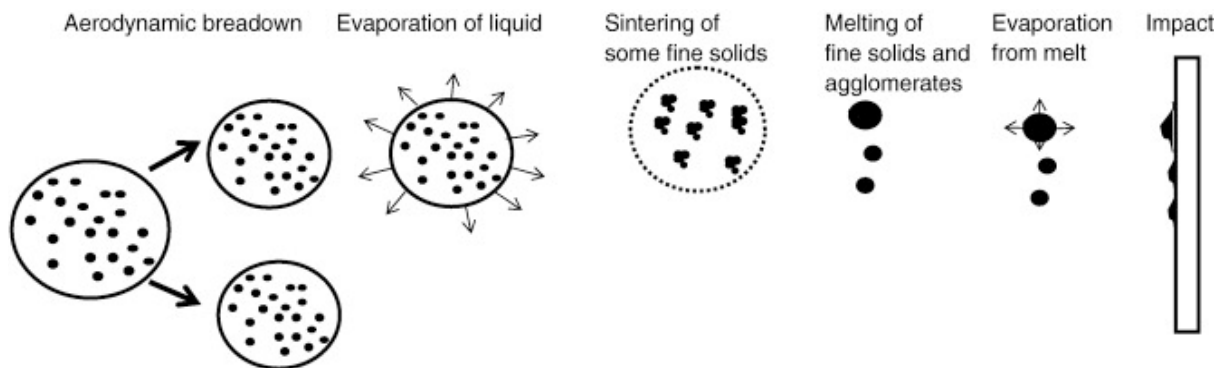
Figure 1-3 Suspension droplet evolution in plasma [9].

Moreover, the secondary break-up happens as soon as suspension droplets penetrate inside the jet, which results from the shear of the liquid droplets by the drag force between plasma and droplets. The aerodynamic break-up time depends on droplet Weber number [9]. Furthermore, the coating structure is directly influenced by the particle properties upon impact, which are determined by the plasma torch operating conditions, feedstock parameters, and suspension characteristics [11]. Therefore, controlling the particle state (temperature, velocity, and size) is very important. The injection method and injection location are a key factors for the resultant particle velocity and trajectory, which affects the residence time of the particles within the plasma flow and their temperature [1].
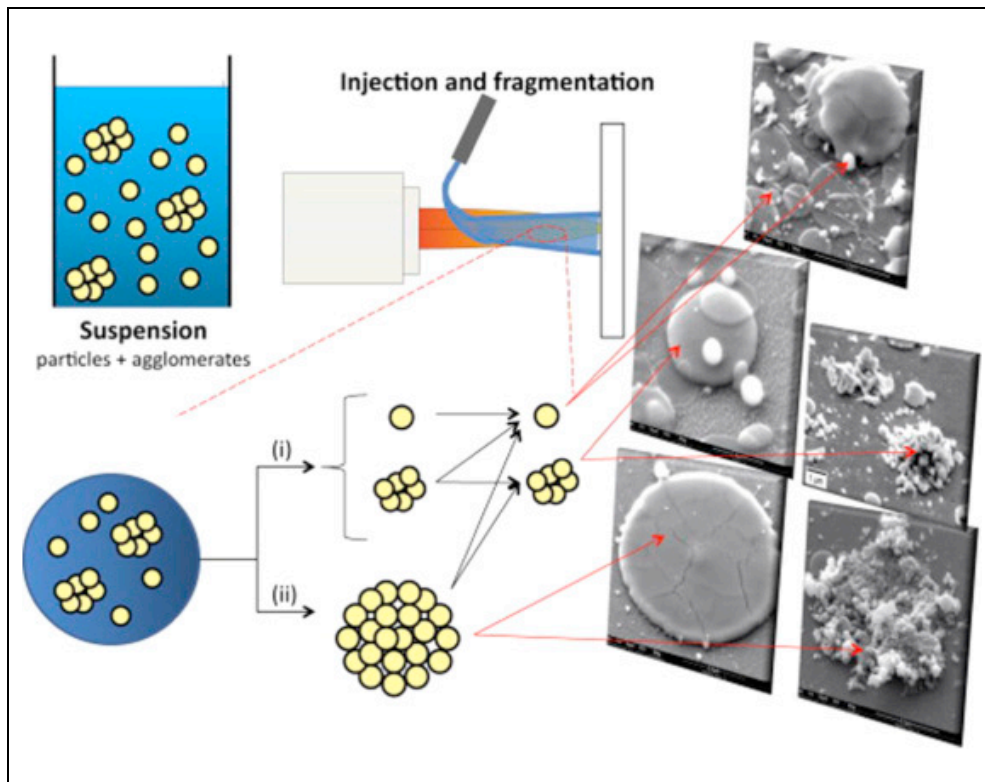
Figure 1-4 Schematic of SPS coatings deposition mechanism [4].

1.3 **Previous work**

Generally, the deposition process of a single droplet consists of three stages occurring

sequentially before impact: 1) transport from plasma gun to substrate, 2) touchdown on the substrate and 3）impinging, flattening and solidification, as illustrated in Figure 1-5.
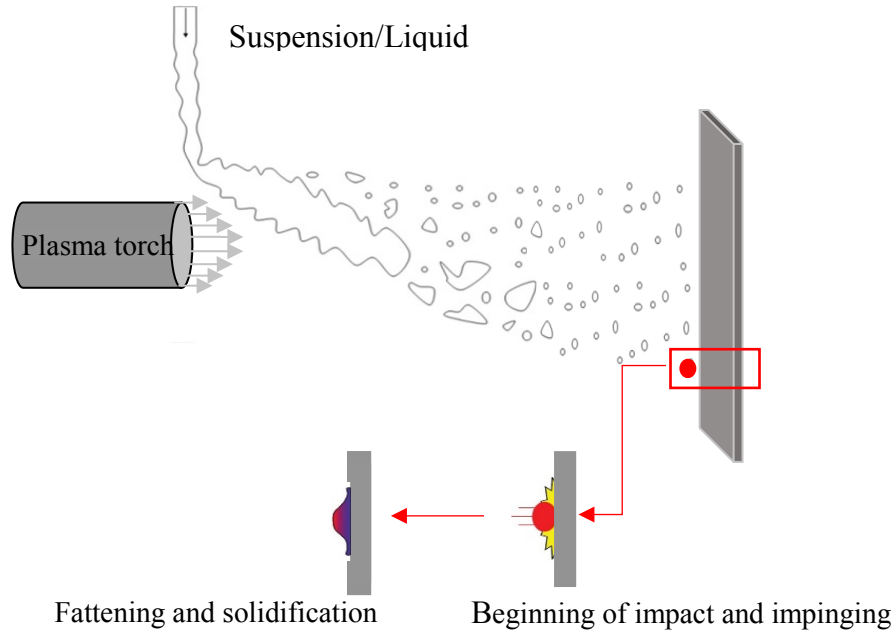
Figure 1-5 Schematic of single droplet deposition process

1.3.1 In-flight particle behavior

Particle conditions upon impact (size, velocity, temperature) affect the coating quality. Generating the desirable coating depends predominantly on the plasma jet characteristic, injection parameters, and interaction between plasma and injected particles. In-flight particle diagnostic systems, such as DPV-2000, AccuraSpray, SprayWatch, etc., are applied for measurement. However, there are application limits related to small particle size and small stand-off distance [12]. The bright plasma jet core, drops fragment speed, droplet evaporation rate, condensed phase size, the number of particles in condensed phases, and velocity gradient within plasma make these experiment methods very complex [6]. Apart from experimental methods, numerical methods have been developed to model the process in spite of its complexity in order to better understand the dominant phenomena occurring during spraying.

In fact, in steady-state mode, two main approaches are used to simulate the plasma flow. In the first one, the velocity and temperature profile are considered as an input [13] and, in the second one, plasma heat is generated by a volumetric heat source inside the torch [14]. Regarding the fact that the formation of the plasma jet is an unsteady phenomenon, the steady-state approach could not capture completely the flow behavior through the process. Two main methods are applied to simulate a transient plasma jet. The first one captured the arc movement by coupling the electromagnetic and fluid equations [15]. In [15], the three-dimensional transient oscillating plasma jet in restrike mode for different arc current was investigated. The second method uses the Joule effect model by considering the energy volume source without electromagnetic effect to take into the account the arc movement [16]. Since the flow behavior through the process is turbulent, choosing the suitable turbulent model is very important. The RANS models, specifically the K-E model, has been used in most of the simulations in comparison with other complex models. For example, Ramesh et al. [17] studied the influence of the carrier gas flow rate on in-flight particle properties. They reported that, on the torch centerline, particle mean velocity and temperature increase by 16% and 10%, respectively by increasing the carrier gas flow rate from 2 to 4 slm. But, by further increasing the carrier gas flow rate from 4 to 6 slm, the velocity increases by 20% and the temperature stays constant. In another study by Shan et al. [18], the effect of drop break-up and collision on particle property distribution were investigated by simulation of a three-dimensional plasma jet. Since the droplet break-up decreases the mean particle size and the droplet collision increases the mean particle size, the dominant effect should be the determinative factor in final particle size and velocity distribution. Vincent et al. [19] proposed a three-dimensional numerical simulation of a turbulent interaction between plasma flow and injected water.

Throughout the literature, it has been shown that the primary atomization is an influential factor in SPS process. The suspension atomization, evaporation, and break-up were simulated in a three-dimensional CFD model by Jabbari et al. [20] to analyze the effect of injection velocity on penetration depth. They reported that the penetration depth increases by increasing the injection velocity. However, if velocity is too high, the number of high-temperature particle decreases. Also, by decreasing the injector distance from nozzle exit, the penetration depth increases leading to an increase of the quantity of higher velocity and higher temperature particles.

It has been known that the presence of a substrate in front of the plasma affects the plasma flow and particle behavior in the vicinity of the substrate. Kang et al. [21] investigated the effect of the presence of a flat substrate on the plasma flow field and behavior of zirconia particles with size ranging between 22 µm and 125 µm. The authors have shown that the plasma flow was considerably influenced by the presence of substrate, but the particle trajectories were unaffected. In another study with the same conditions used in [20] and Jadidi et al. [13], the effect of the presence of substrate at different standoff distances on submicron particle properties near the substrate was investigated. It was concluded that the penetration depth left unaffected by standoff distance. Furthermore, it was described that, due to the stagnation region near the substrate, the trajectory of small particles were deviated as they tend to follow the trajectory of the plasma flow. The effects of the curved substrate as well as flat one were discussed in Pourang et al. work [14]. They reported around 50 % higher deposition rate on a flat substrate in comparison with a curved one.

1.3.2 Single droplet impact

SPS coating layers are formed by the consecutive impingement of sub-micron or few-micron sized particles and coating properties are influenced by the actual arrangement of nature of

the resulting splats. In fact, splat shape is the building block of coating structure. Hence, an understanding of single droplet flattening, solidification, splat microstructure is essential. In addition, it will help us to better understand the underlying mechanisms and control the coating microstructure. The developments in droplet impact on solid surface as well as splat formation process from individual molten particles are discussed below including experimental results and numerical simulations.

In spite of the fact that the study of droplet impact was started by Worthington 1876 [22] (Figure 1-6), the explanation of the impact process has not been fully understood until the recent years because of the complex impact dynamic. Recent development of high-speed video technology let us have time resolved observations [23] that help improving our understand of these complex phenomena. Also, increasing computational power with improved numerical methods allow us to have more reliable axisymmetric simulations [24].
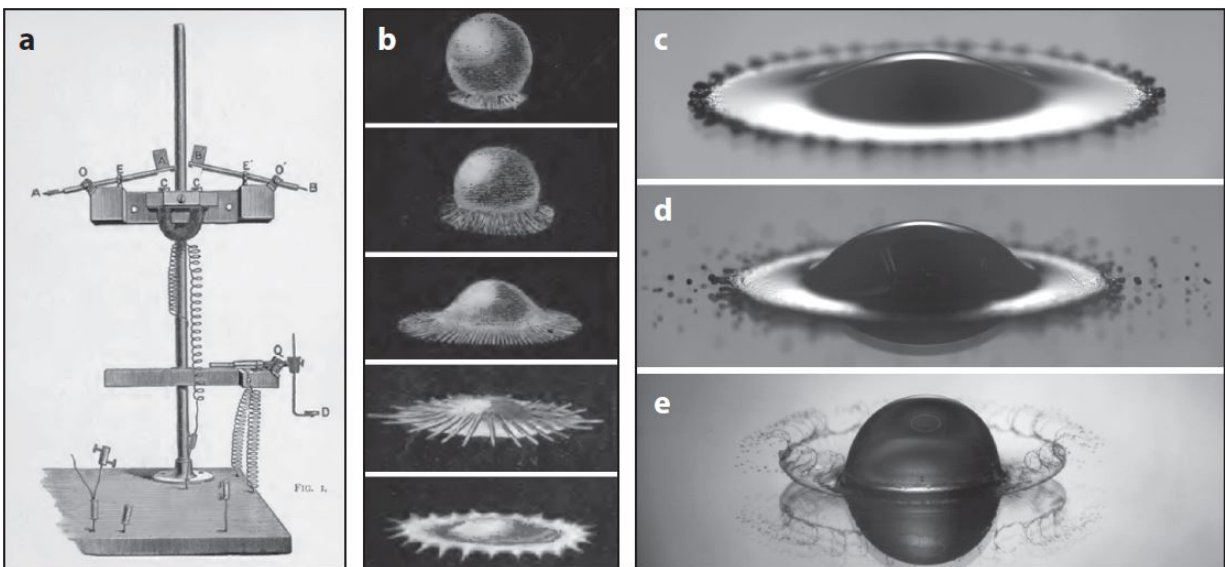
Figure 1-6. (a) Worthington's drop-release setup and (b) mercury drop impact sketches by Worthington's. Using modern video technology to, (c) reproduction of Worthington's work on glass, (d) prompt splash for mercury drop impacting superhydrophobized glass, (e) and corona splash for ethanol drop on the glass. [25].

Droplet impact phenomena depends mainly on two dimensionless parameters; Reynolds number,

Re, representing the inertia to viscous forces and Weber number, *We*, which represents the ratio of the inertia to capillary forces.

$$Re = \frac{\rho_l D v}{\mu_l} \qquad\qquad 1\text{-}1$$

$$We = \frac{\rho_l D v^2}{\gamma} \qquad\qquad 1\text{-}2$$

Where, ρ_l, μ_l, v and D are droplet density, kinematic viscosity, velocity and diameter, respectively. γ is surface tension in Eq. 1-2.

Additionally, Stokes number, St, describes the influence of gas on droplet before impact as shown in Eq. 1-3:

$$St = \frac{\mu_g}{\rho_l D v} \qquad\qquad 1\text{-}3$$

$$St = \frac{\mu_g}{\mu_l} \cdot \frac{1}{R_e}$$

Where, μ_g is the surrounding gas kinematic viscosity.

Finally, there are two other dimensionless parameters that may affect the outcome of droplet impact; aspect ratio of the droplet at impact, the contact angle related to droplet shape and substrate properties respectively.

The behavior of particle after impact depends on particle impact conditions as well as substrate properties. After a particle impact on the surface, various phenomena could happen including spreading, rebounding, and splashing while the latter is resulted from the fine liquid break up. Also, the deposition and bouncing are dependent on the wetting properties of surface. Most of the studies focused on two types of splat as shown in Figure 1-7, such as splash splat and disk-like splat. The splash splat is splash fingers which is connected by one central splat and disk-like splat is one central disk.
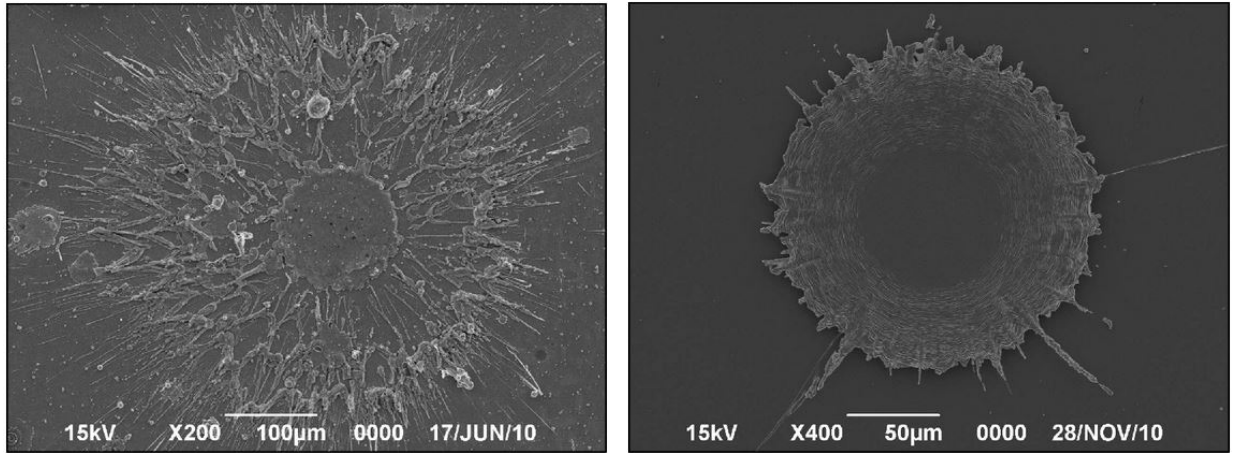
(a)   (b)

Figure 1-7 Typical splat morphology: (a) splash splat and (b) disk-shaped splat [26].

To characterize the transition between spreading and splashing regime, the splashing parameter, K

(Sommerfeld number), was proposed by Mundo et al. [27] as Eq.1-4:

$$K = We^{1/2} Re^{1/4} \qquad\qquad 1\text{-}4$$

For
$$\begin{cases} K{<}3 & \text{splat rebounds} \\ 3{<} K{<}57.7 & \text{deposition} \\ K{>} 57.7 & \text{splash regime} \end{cases}$$

It seems that the traditional K model (Eq.1-4) is independent of particle properties. To address this

problem, Fukumoto et al. [28] [29] considered the in-flight particle information as well as substrate

temperature as shown in Eq.1-5:

$$K_f = 0.5a^{1.25} Re^{-0.3}K \qquad\qquad 1\text{-}5$$

Where a is the ratio of the maximum flattening velocity to the impact velocity of the particle and

it depends on substrate temperature.

In the case of disk-like splat, the droplet spreads until it reaches a maximum diameter and deforms from a sphere to a disk shape. Then, depending on the impact conditions and surface properties, the lamella could recede or it either spreads more or does not change [30].

Bartolo et al. [31] performed some experiments to study the effects of three forces (i.e. the capillarity, viscous, and inertia forces) on liquid droplet retraction. For a specific case, they [32] reported that droplet impact on the superhydrophobic substrate can result in the jet formation and rebound of the droplet. In another study, Bayer et al. [33] showed the dependency of rebound and jetting dynamics on textured surface wettability.

Wettability of surface depends on chemical and physical (nanotexture) properties of the surface. Two main wetting theories, liquid penetrate to texture and move over the surface, was proposed by Wenzel (1936) and Cassie & Baxter (1944) respectively. Rebound and jetting dynamics were investigated by Antkowiak et al. [34] in droplet impact on the elastic surface.

In the case of disk-like splat, where no splashing and jetting is present, the maximum spreading diameter is the most important case to study. Different droplet impact regimes are presented in Figure 1-8.
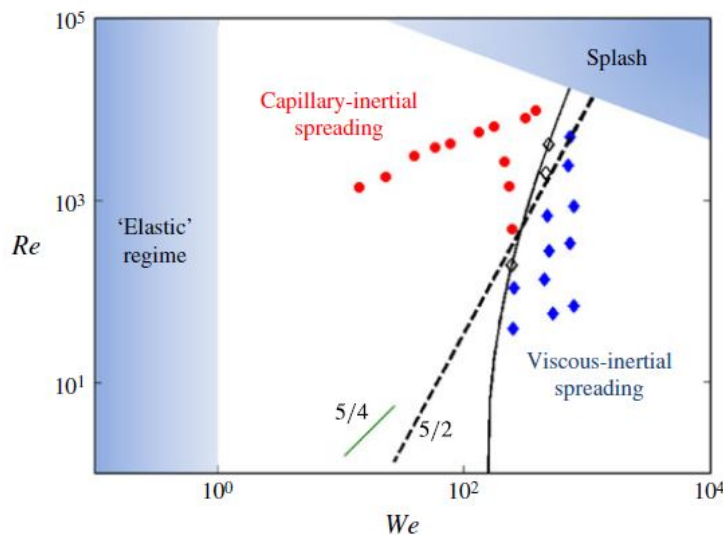
Figure 1-8 Different drop impact regimes [35].

Throughout the literature, maximum spreading diameter has been simulated based on the balance between inertia, capillarity, and viscous forces (Chandra & Avedisian 1991[36], Pasandideh-Fard et al. 1996 [37], Range & Feuillebois 1998 [38], Roisman et al. 2002 [29], Clanet et al. 2004 [39], Fedorchenko et al. 2005 [40], Ukiwe & Kwok 2005 [41], Roisman 2009 [42], Vadillo et al. 2009 [43], Eggers et al. 2010 [44]). The spreading ratio in Eq.1-6 is defined by the ratio of the maximum diameter, D_{MAX}, to initial diameter, $D_{initial}$:

$$\zeta = \frac{D_{MAX}}{D_{initial}} \qquad \text{1-6}$$

The impact number, P, given by Eq.1-7, was defined to separate two regimes, capillary regime expansion with low P and viscous regime expansion with high P:

$$\mathrm{P} = We\,Re^{\alpha} \qquad \text{1-7}$$

where, $\alpha < 0$ and We and Re are Weber and Reynolds number, respectively.

In the viscous regime, the maximum spreading diameter is deduced from a balance between the kinetic energy and viscous dissipation. While, in the capillary regime, the maximum spreading diameter is determined from a balance between the inertia and capillary force. It is difficult to differentiate between a model based on capillary selected pancake $P = We\,.\,Re^{\frac{-4}{5}}$ (Clanet et al. [39]) and based on surface energy balance $P = We\,.\,Re^{\frac{-2}{5}}$ (Eggers et al. [44]). Due to the limitation in the experimental and numerical modelling, none of the correlations give a precise result for a wide range of impact conditions. Table 1 summarizes the proposed correlations between experimental and numerical results from the literature.

Table 1 Different predictive models for maximum spreading diameter [25].

Model	Year	Expression	Comment
J.Madejski [45]	1975	$$\frac{3\,\zeta^2}{We} + \frac{1}{Re}(\frac{\zeta}{1.2941})^5 = 1$$	Based on energy balance flattening without solidification
Scheller & Bousfield	1995	$$\zeta \sim 0.61\,(Re^2 Oh)^{1/6} = 0.61\,Re^{1/5}(WeRe^{-2/5})^{1/6}$$	Based on experimental results
Pasandideh -Fard et al.	1996	$$\zeta = \sqrt{\frac{We+12}{(1-\cos\theta_a)+4(We/\sqrt{Re})}}$$	Based on energy balance, including advancing contact angle (θ_a)
Clanet et al.	2004	$$\zeta \propto We^{1/4}$$	Based on Mass balance, using the impact capillary length $(a = \sqrt{\frac{\sigma}{\rho g}})$
Ukiwe & Kwok	2005	$$(We + 12)\zeta = 8 + \zeta^3\left(3(1-\cos\theta_d) + 4\frac{We}{\sqrt{Re}}\right)$$	Extension of the Pasandideh-fard model, using the Dynamic contact angle (θ_d)
Roisman	2009	$$\zeta \sim 0.87\,Re^{1/5} - 0.4\,Re^{2/5}We^{-1/2}$$	Based on dynamic model, involving the rate of the growth of viscous boundary layer thickness
Eggers et al.	2010	$$\zeta = Re^{1/5}\,f(P)$$	Similar approach used in Roisman model; impact number P is defined by $P = WeRe^{-2/5}$

1.3.3 Coating build-up

Thermal spray coatings are built by successive accumulation of molten or semi-molten particles that reach on the substrate or previously deposited layers. Molten particles after impact turn into lamella in a form of pancake (disk shape) or flower (disk with splash). Due to the rather low *We*

number associated with SPS particles, observations show more particles in the form of pancake shape [9]. The microstructure of SPS coatings shows a multi-scaled porosity with different morphologies; vertically cracked, homogeneous, or columnar structure. The columnar structure build-up mechanism has been explained as a result of small particle deviation near the substrate and impinging at shallow angles [10]. In a recent study by Bernard et al. [10], the columnar structure is found to be influenced mainly by three parameters (Figure 1-9): substrate roughness, torch linear speed, and particle conditions upon impact. The vast distribution of column diameter is demonstrated by increasing the roughness. In addition, the columnar structure was found to be more compact in the case of higher torch velocity due to decreasing the coating growth at each torch pass. Additionally, the experiment conducted by Bernard et al. shows that an increasing the suspension load leads to inter columnar void reduction [10].
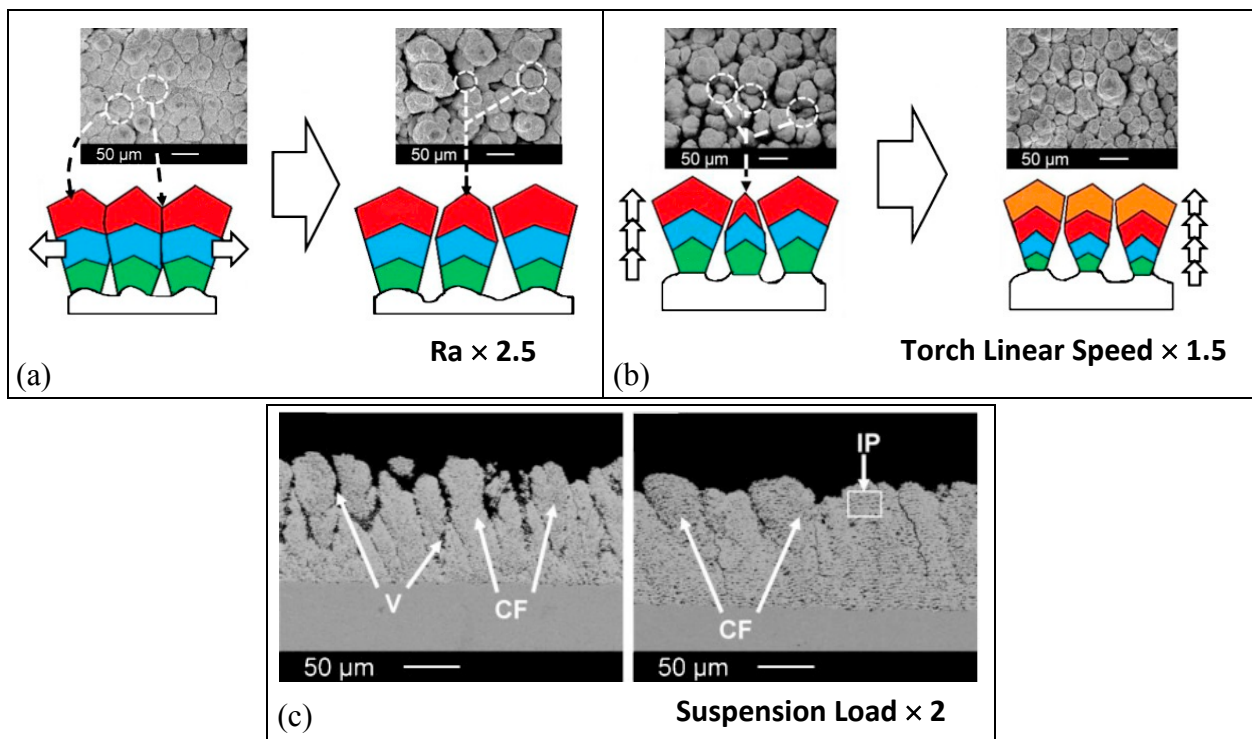
Figure 1-9 Columnar structure influential parameters, (a) roughness effect, (b) torch speed effect, (c) suspension load effect [10].

Sokołowski et al. [44] studied the effect of powder types, solid concentration in suspension, substrate preparation method, and plasma spray setup on the columnar structure in YSZ SPS coating. The author's work is summarized below and illustrated in the following figures.

In this work, the coating morphologies obtained with a SG_100 plasma torch (internal injection) and suspension concentration of 2.5 wt.% and 5 wt.% show the columnar structure for all types of substrates as shown in Figure 1-10 and Figure 1-11.
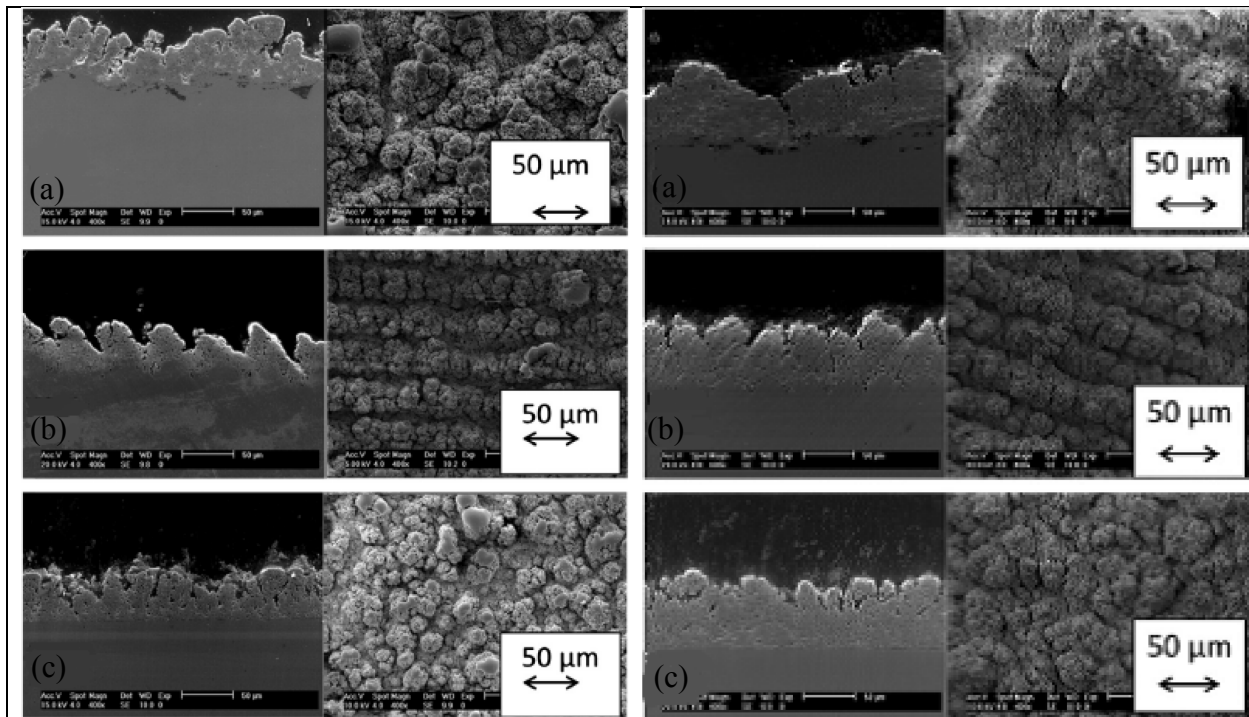
| Figure 1-10 Cross-sections (left side) and surfaces (right side) of SPS using SG-100 torch and 2.5 wt.% of fine powder onto substrates prepared by, (a) sand blasting, (b) laser treatment, (c) grinding [46]. | Figure 1-11 Cross-sections (left side) and surfaces (right side) of SPS using SG-100 torch and 5 wt.% of fine powder onto substrates prepared by, (a) sand blasting, (b) laser treatment, (c) grinding [46]. |

The columnar structure is more visible for 2.5 wt.% than 5 wt.% particularly in the case of grinded substrate. However, the columnar structure is formed for 10 wt.% only in laser treated surface as shown in Figure 1-12. Moreover, the coatings morphologies deposited using a Triplex plasma torch (external injection) and suspension concentration of 10 wt.% is dense and, like with the SG_100 torch, the columnar structure is formed only in laser treated surface as illustrated in

16

Figure 1-13. The coating porosity is lower using the Triplex torch as compared with the SG_100 torch. The porosity is found to decrease from lower suspension concentration to the higher suspension concentration for both torches. Furthermore, the use of a coarse powder leads to coatings without columnar structure for different types of substrates and torches as illustrated in Figure 1-14 and Figure 1-15.
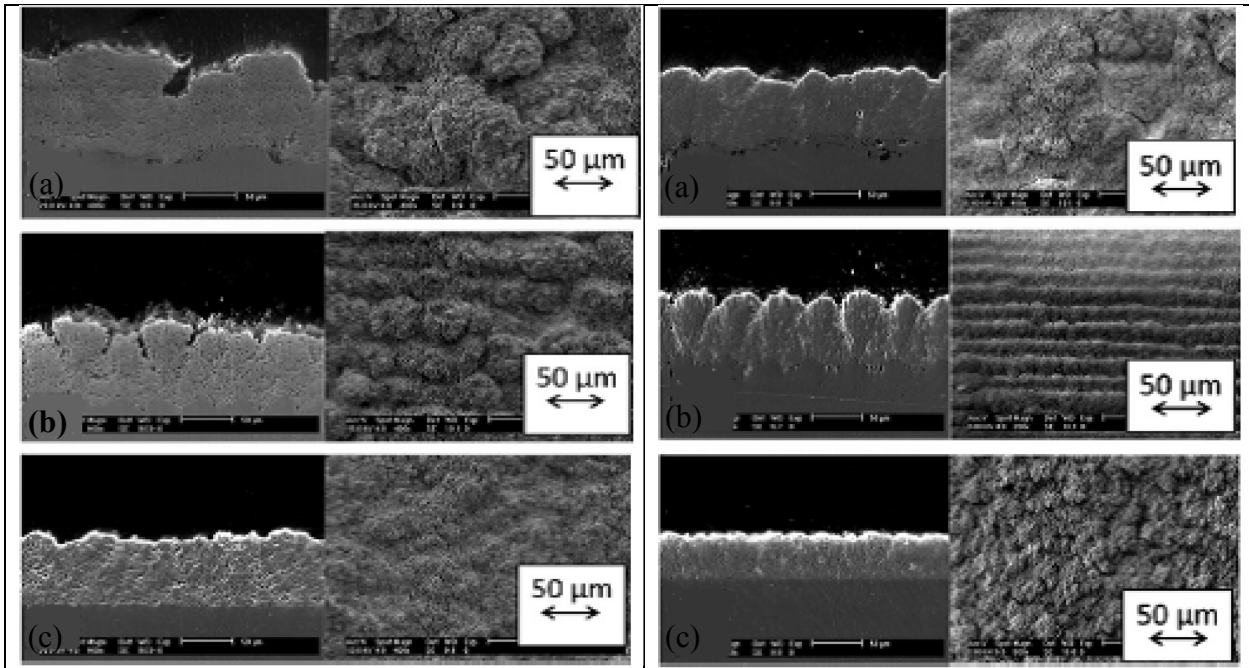
| Figure 1-12 Cross-sections (left side) and surfaces (right side) of SPS using SG-100 torch and 10 wt.% of fine powder on to substrates prepared by, (a) sand blasting, (b) laser treatment, (c) grinding [46]. | Figure 1-13 Cross-sections (left side) and surfaces (right side) of SPS using Triplex torch and 10 wt.% of fine powder on to substrates prepared by, (a) sand blasting, (b) laser treatment, (c) grinding [46]. |

| Figure 1-14 Cross-sections (left side) and surfaces (right side) of SPS using SG-100 torch and 10 wt.% of coarse powder on to substrates prepared by, (a) sand blasting, (b) laser treatment, (c) grinding [46]. | Figure 1-15 Cross-sections (left side) and surfaces (right side) of SPS using Triplex torch and 10 wt.% of coarse powder on to substrates prepared by, (a) sand blasting, (b) laser treatment, (c) grinding [46]. |
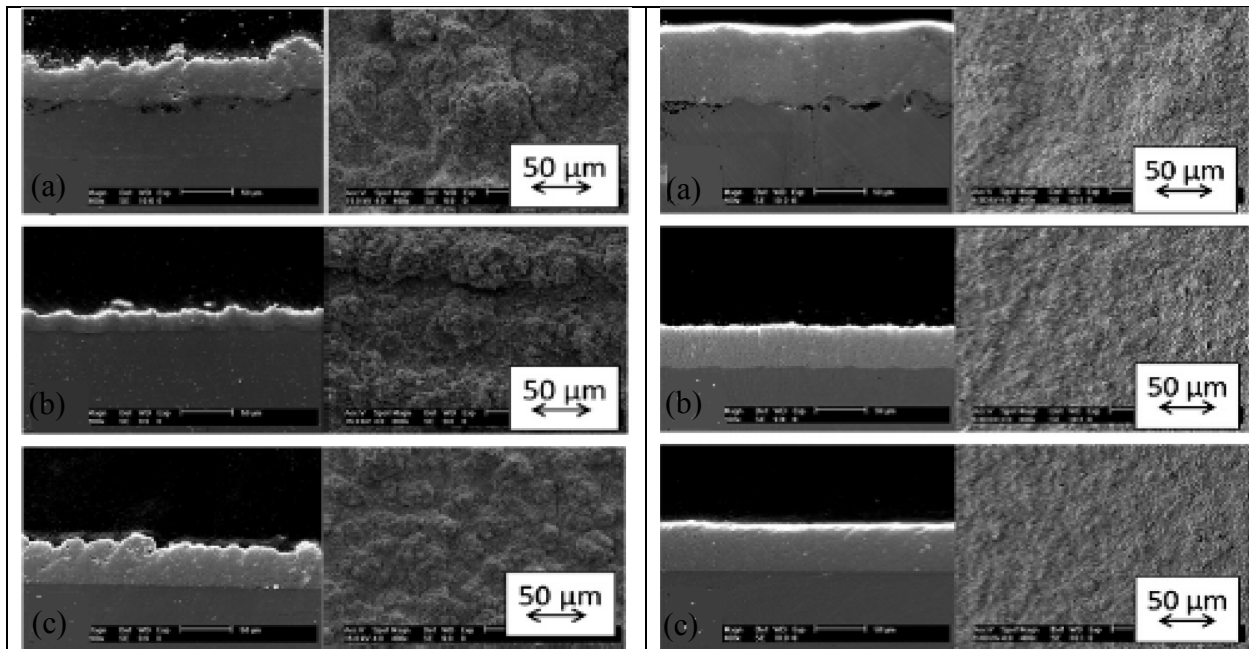
Furthermore, they showed that the coating porosity decreases by increasing the powder size in suspension. In addition, the substrate preparation shown in Figure 1-16 has an influence on the coating morphology. Only laser treated substrate enabled the formation of columnar microstructure independent of the type torched used. The machined substrate produced columnar structure only when SG_100 torch was utilized.
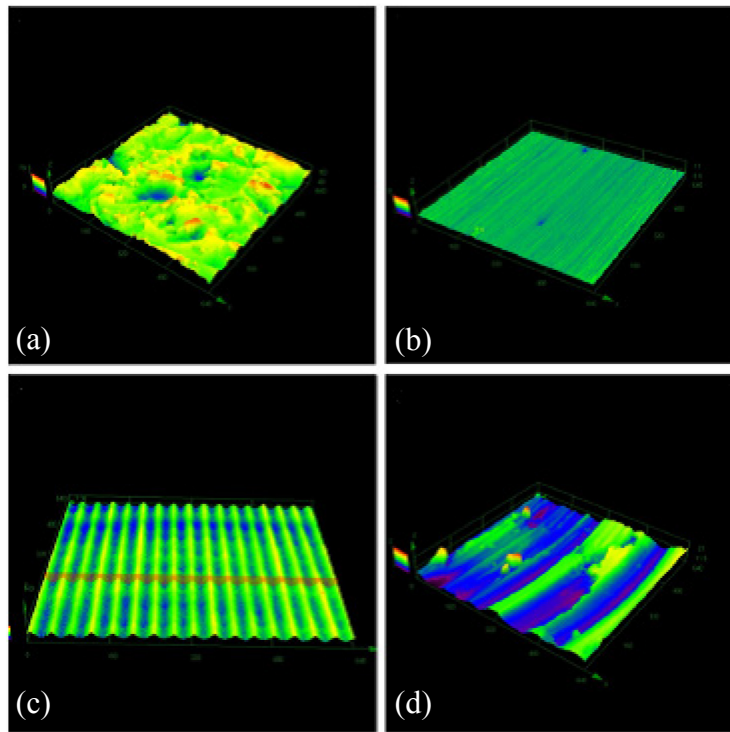
Figure 1-16 Different substrate structures used to deposit coatings, (a) grid-blasted, (b) grinded, (c) laser treated, and (d) turned [46].

In another study, Seshadri et al. [45] explained the relationship between microstructure and involved processing parameters such as plasma flow, and injection orientation. They showed that the plasma power and gas flow rates (plasma spray parameters) which control melting and fragmentation, are the most influencing factors in microstructure formation. The deposition rate effect was addressed by adjusting raster speed while particle state effect was addressed by varying plasma power, injection angle, and plasma gas flow rate. As can be seen in Figure 1-17, the inter-columnar space increases and microstructure density decreases by increasing the plasma flow rate. It is assumed that by increasing the primary gas flow, the plasma flame velocity increases, which in turn, decreases particles residence time in the plasma. This resulted in reduction of the particle temperature and less melting. Thus, at the higher flow rate, there obtained smaller droplets as a result of higher turbulence in particles and plasma flow interaction (resulting in better suspension

atomization), which cool faster and lead to feathery structure. Additionally, higher flow rate blows away particles from spray bead and extend inter-columnar space.
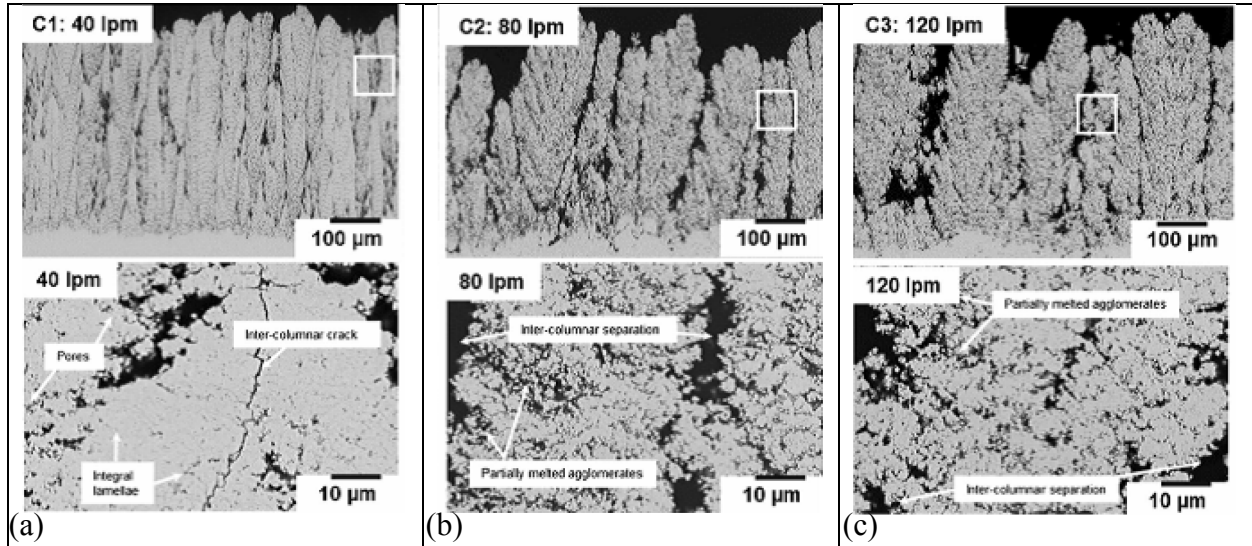
Figure 1-17 SPS deposited microstructure with: (a) low primary gas flow, (b) medium primary gas flow, (c) high primary gas flow [47].

The arc fluctuation pattern resulting from the arc flow-electrode interaction can be classified into three different modes as illustrated in Figure 1-18. It is obvious from the figure that the steady mode is with no fluctuation of voltage. However, the restrike mode is characterized by an anode arc movement with sudden restrike near the cathode creating a sawtooth-shaped voltage oscillation. The takeover mode is also characterized by a back and forth oscillation of the arc root in the flow direction (sinusoidal voltage oscillation) [48].
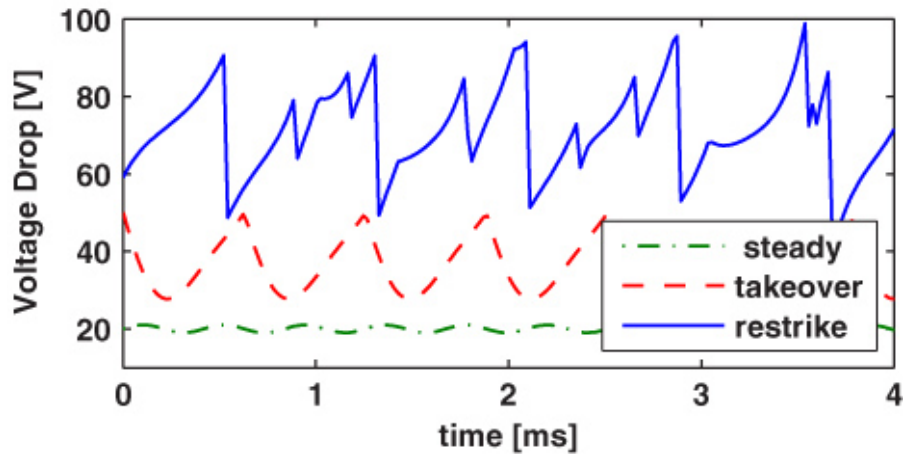
Figure 1-18 Various arc operation modes [49].

In the same study, Seshadri et al. [45] found that the effect of arc current is totally opposite to that of the plasma flow rate. As the arc current increases, the particle velocity remains the same but particle temperature increases which leads to better melting. Due to the better melting, the microstructure changes from porous to dense [45]. The effect of plasma current is shown in Figure 1-19 .
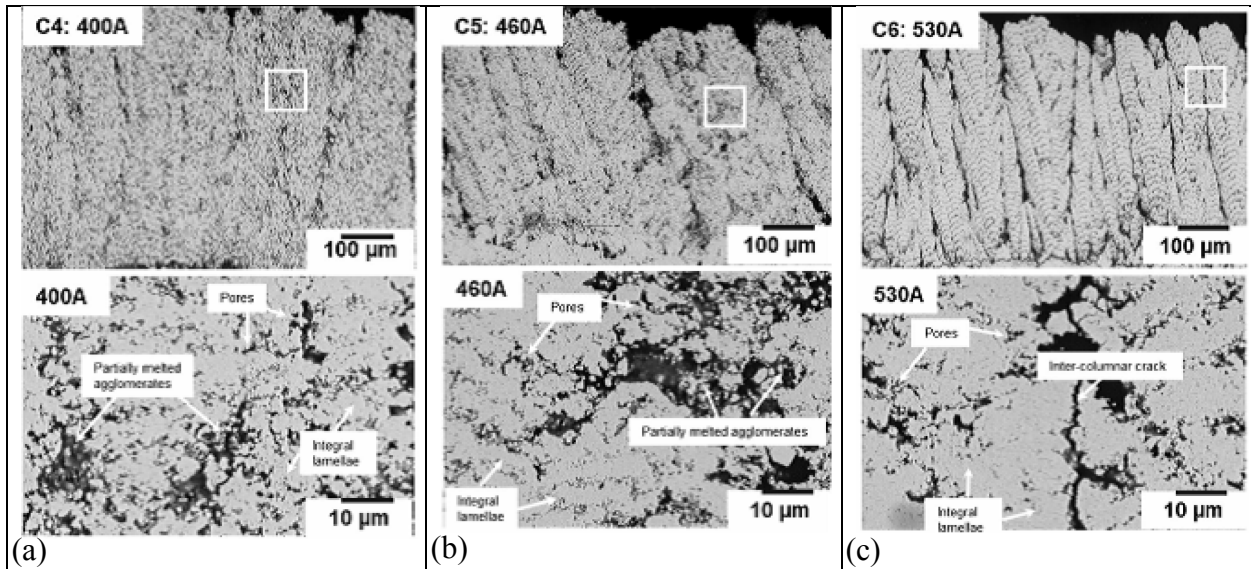
Figure 1-19 SPS deposit microstructure with, (a) low torch current, (b) medium torch current, (c) high torch current [47].

In fact, under low power, there are larger suspension droplets due to less effective atomization.

Therefore, available energy to heat the particles reduces resulting in larger particles at the substrate and porous microstructure. Furthermore, suspension injection to plasma plume is very challenging and changes the suspension penetration inside the plume. The particle temperature and velocity are higher, in the case of downstream injection (105°) than orthogonal (90°) and upstream injection (75°) which is contrary to our prediction. It is due to the ethanol combustion zone [45]. Figure 1-20 illustrates the schematic of suspension injection angle to plasma plume.
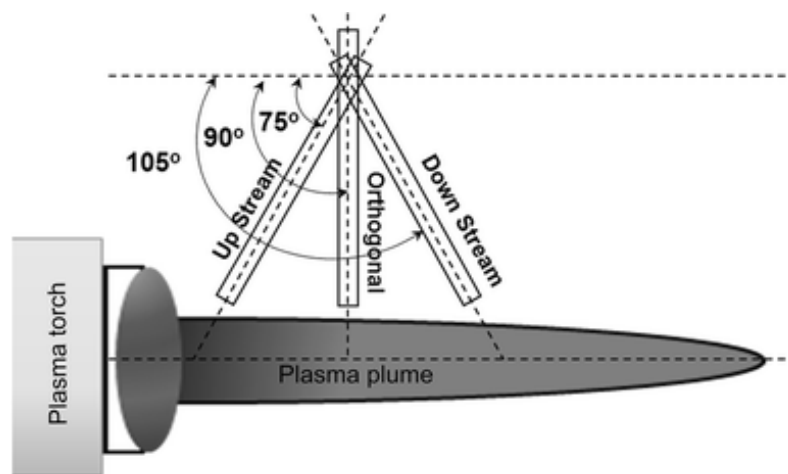
Figure 1-20 Schematic of injection configurations [47].

As can be seen in Figure 1-21, the columnar structure in orthogonal injection (90°) is denser than upstream injection (75°) since upstream injection is faced with higher shear drag force to penetrate to core. This leads to smaller droplets, in the case of downstream injection, as result of higher fragmentation of particles. The columnar structure in downstream injection (105°) is unique with wide column, inter-columnar void, and fanned columns. Moreover, SPS coating microstructure was found to vary with the raster speed. It can be seen in Figure 1-22 that the cracks and inter-pass bands become small by reduction in the deposition rate (thickness deposited per pass).
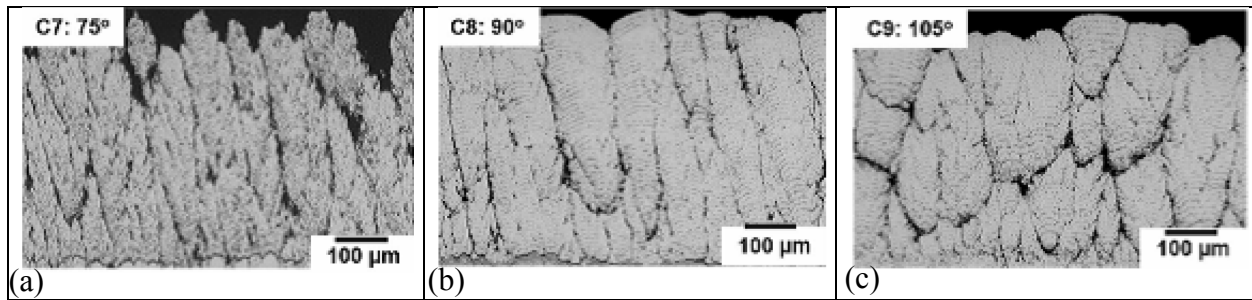
Figure 1-21 SPS deposit microstructure with, (a) upstream injection, (b) orthogonal injection, (c) downstream injection [47].
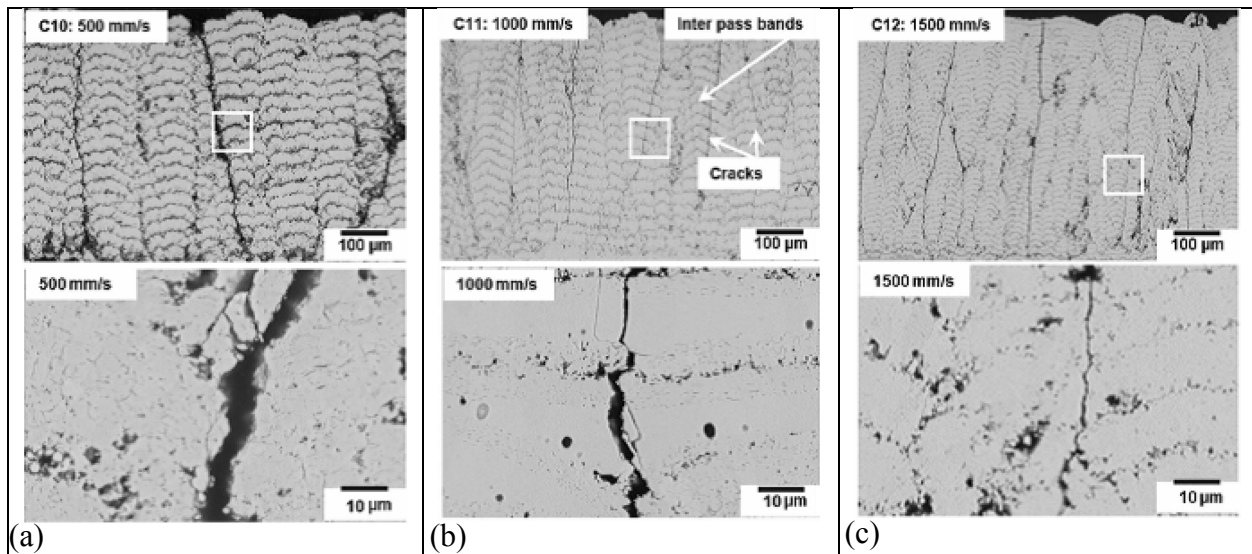
Figure 1-22 SPS deposit microstructure with, (a) low raster speed (deposition rate), (b) medium raster speed (deposition rate), (c) high raster speed (deposition rate) [47].

1.3.4 Modeling of coating build-up

Alongside the experimental works, considerable efforts have been done to simulate and model the coating and its structure in APS coatings, where the coatings micro-structure are formed by the impact and spreading of large particles, and physical vapor deposition (PVD). The analytical approach was proposed by Cai et al. [50] to investigate the porosity in coating microstructure by considering the solidification shrinkage as a porosity reason. In another study, Fukanuma et al. [51] proposed a mathematical model for porosity production as a result of molten particle deformation. Knotek et al. [52] simulated a two-dimensional model to predict the size and distribution of inter lamellar cracks by using the stochastic Monte Carlo method to deposit

particles with various size and velocity. More complex two-dimensional stochastic models presented by Cirolini et al. [53] and Harding et al. [54] show the interaction between splats. Kanouffet et al. [55] proposed a two-dimensional model to calculate the coating surface roughness with the off-normal spray angle, by using "string model" in which a uniform space nodes define the coating surface. In this model the splats thickness calculated with respect to surface normal direction. However, a numerous unrealistic roughness was captured. Hansbo et al. [56] derived a mathematical model of a layer build-up on a rotating curved surface to obtain desirable coating thickness regardless of internal microstructure. Although two-dimensional models are used in predicting coating structures, it has some limitation in capturing pore or crack networks since the process is inherently three-dimensional. Ghafouri-Azar et al. [57] and Mostaghimi et al. [58] and Xue et al. [59] simulated a three-dimensional stochastic model. The domain was considered as a voxel with an adaptive resolution of splat edge to improve accuracy. Splats were successively deposited on top of the already deposited ones. The maximum spread diameter and thickness were calculated by analytic expression [60]. Afterward, one of the four different scenarios was chosen based on the distance between inserted splat center. The idea comes from the observation of droplet imping on top of another one. Further, it was assumed that the splat boundary curl up was the only reason for the formation of porosity. Beauvais et al. [61] developed a three-dimensional random model to show interlamellar pores and interlamellar cracks. The splat shapes inserted randomly into voxel volume from the library of mathematical objects which are derived from experiments and measurement using confocal microscopy. Wiederkehr et al. [62] proposed a three-dimensional model using the Lattice-Boltzmann (LB) method by coupling single splat simulation and coating build-up for about 10000 splats. The model used the database from the previous single particle impact simulation on different

undergrounds and inserted suitable splats, which showed a good match to typical microstructures.

Moreover, Thomas Merkh et al. [63] developed a three dimensional Monte Carlo method to simulate film deposition under high pressure deposition conditions. The trajectory of upcoming particles was determined according to predefined probability distribution. Also, the two aggregation strategies, including solid on solid and ballistic techniques, were employed and investigated. By using the Monte Carlo method, the correlation between particles properties (size, velocity, temperature) are neglected. Since in the SPS method mostly the small particles have higher temperature and normal velocity in compare to the larger ones and impact close to the plasma torch centerline. In addition, in most film deposition simulation, particles are sequentially dropped and follow the path of the steepest descent on the surface. Once found a stable position, the particle is immobilized. However, in SPS technique, the upcoming particles stick on the surface at impact location.

To our best knowledge, no 3-dimentional coating build-up models have been developed to date. The main challenges associated with such models are the deflection of small size particles due to the presence of the substrate and shadow effect.

1.4   Objectives

Nano-structured thermal barrier coatings have been considered as one of the interesting subjects due to their ability   to decrease their thermal conductivity and increase their thermal stability. According to recent works, the simulation of thermal spray process such as plasma spray, particle and gas interaction, and single micro-droplet impact have been widely studied focusing on different materials, processes, and modeling techniques. However, the literature on stacking of thousands of particles and coating build-up simulation is relatively rare. Based on the previous studies on coating built-up simulation, some attempts were done to simulate coating build-up for APS with   particle size ranging between 20 µm and 80 µm at normal impact. However, in the SPS process, since the   mean particle size is less than 3 µm (low Stokes number) most of the particle trajectories are modified by the presence of a substrate resulting in impacts at oblique angles. Currently, there is no three-dimensional suspension plasma spray (SPS) coating build-up simulation.

Coatings structure depends on various variables such as torch speed, standoff distance, powder type and feed rate, solid concentration in suspension, substrate preparation method, suspension load and suspension injection orientation, plasma power, etc. Therefore, to achieve a desirable coating structure, proper values should be selected for these parameters by the operator. Making an optimized structure with the desired characteristics for any specific applications is a long process with many back and forth trials. Due to the aforementioned complexities associated with experiments and also   time and cost, coating build-up simulation would serve as a tool to overcome these limitations and   study the influence of numerous spray parameters on the resulting coating microstructure. In addition, it can help to anticipate coating quality regarding operating parameters to achieve a cost and time reduction of the process, increase the

accuracy and modifying coating parameters based on the application to achieve an optimum coating.

The aim of the present work is to develop a computational code to simulate SPS coating build-up by using a three-dimensional stochastic model to predict the coating microstructure and, in particular, the columnar structure observed in SPS coatings. The steps to achieve this objective include:

1. Development of an algorithm to include various possible impact scenarios in SPS with respect to the landing adjacent cells.

2. To simulate two-dimensional coating build up.

3. To simulate three-dimensional coating build up.

2 Methodology

In this chapter, an overview of the coating build-up mechanism is presented. Furthermore, assumptions, sample input data, defined variables and scenarios are presented.

First, in this study, from the CFD simulation of plasma spray gun, which was developed by Pourang et al. [14], the impact property values of each particle including size, velocity, temperature, as well as particle's location near substrate are obtained. Thereafter, the results from CFD simulation are used as a sample input to create a pool of the particles with different characteristics. The particles are selected randomly from this pool. The computational domain is created and divided into discrete control volumes (cell). Then, the trajectory of each particle upon impact is calculated and all the cells through the particle trajectory are examined by using the defined ($f_{i,j,k}$) variable to find out the final impact location. The particle is deposited in impinged location based on the prescribed scenarios.

2.1 Coating build-up mechanism in SPS

The Stokes number describes the behavior of in-flight particles which move through the plasma flow. Since a particle with small mass has small Stokes number, sub-micron particles in SPS track the flow field, which are affected by the presence of substrate, and turn and move across the surface. This change decreases the particle velocity component perpendicular to the substrate and increases the velocity component parallel to the substrate as seen in Figure 2-1.
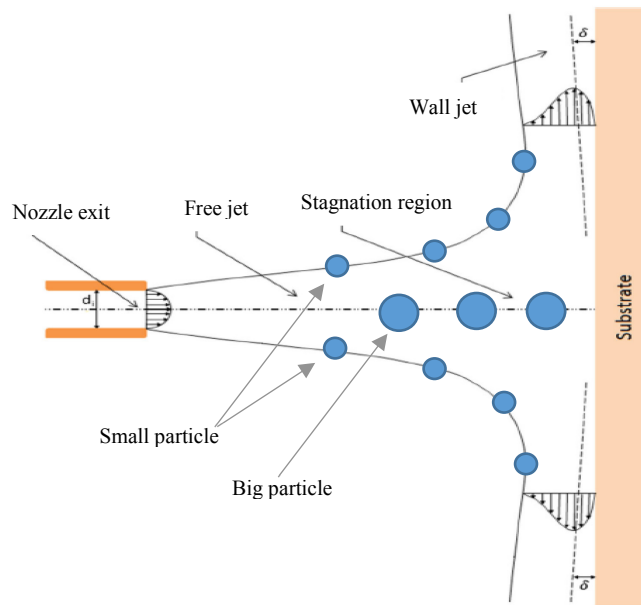
Figure 2-1 Schematic of the typical impinging gas-jet system [13].

Therefore, most of the particles impact the surface with the oblique angle and a few have normal impact. The aforementioned factors lead us to the idea that the columnar microstructural results from directional changes in particles trajectory near the substrate. To further understand this phenomenon, we explain below the theories which were formulated by Kent VanEvery, et al. [64] based on the deposition mechanisms. According to the authors, there are three different types of deposition mechanisms as can be seen in Figure 2-2.
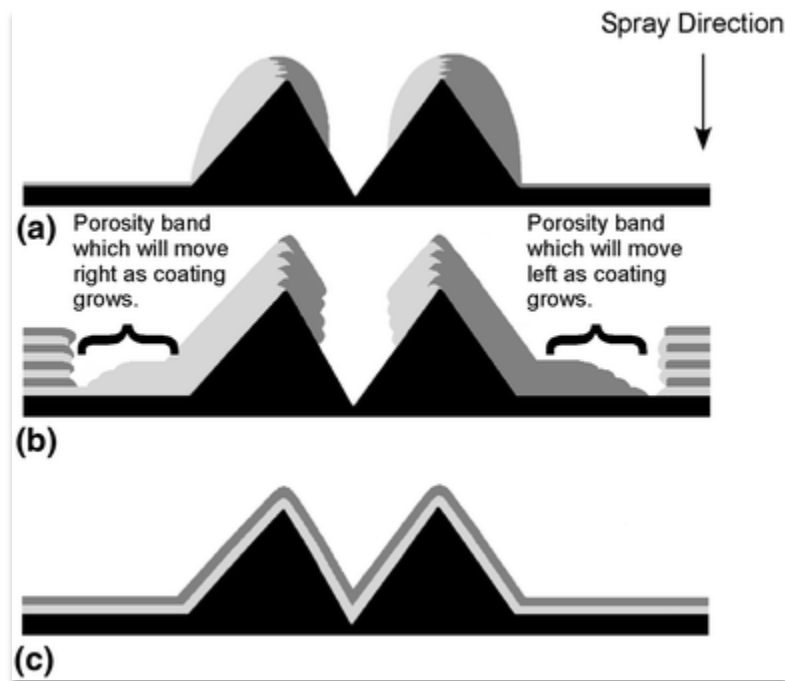
Figure 2-2- Schematics illustrating the deposition characteristics occurring on and away from substrate surface asperities during suspension deposition (a) Type 1, (b) Type 2, and (c) Type 3 [64].

Type 1:

In the first case, small particles follow the plasma trajectory upon impact. The parallel velocity component of these particles dominates the normal component to the substrate. As a result, most of the particles impact on the sides of surface asperities and the coatings grow vertically and laterally on the surface. Throughout the deposition process, the lateral growth of higher deposits may cover the lower deposits. At the time, the same height deposition, gradually the lateral growth stop and the inter-columnar void will be formed. As spraying continues, the columnar structure will be formed by proceeding lateral growth and inter-columnar voids.

Type 2:

In the second case, the normal velocity component dominates the parallel one, but particles trajectory are still influenced by the parallel velocity component. In comparison with type one, there are bigger particles which are affected less by plasma flow and some of them detached from

plasma trajectory. As a result, the deposition increases between surface asperities. However, surface asperities shadow the portion of substrate downstream from asperities.

Early in the coating process, due to the shadowing effect, the growing rate at the extreme right and left of asperities (unshadow parts) is almost twice faster than that at the substrate asperities. As the height differential between the unshadowing regions and asperities decreases, the deposition on the sides increases. So unshadow parts grow toward the asperities and overgrow above them. Consequently, in type two, we have a columnar structure as in the first type but less distinctive.

Type3:

In this case, there are massive particles in comparison to the two first cases. The plasma flow does not affect the particles, and most of them have a normal impact to the substrate. Thus, there is no columnar structure as there is no shadow effect.

It is realized that the evolution of the columnar structure is as a result of lateral growth velocity ($v_{\parallel}$) and normal growth velocity ($v_{\perp}$) combination around the substrate. As it is depicted in Figure 2-3, the lateral growth velocity ($v_{\parallel}$) and normal growth velocity ($v_{\perp}$) are defined in Eq.2-1.

$$v_{\perp} = \frac{de}{dt} \qquad\qquad 2\text{-}1$$

$$v_{\parallel} = \frac{dD}{dt}$$

where t, e, and D are spraying time, coating thickness and coating mean diameter.

It is assumed that the undeviated particles which have the larger size contribute to the normal growth velocity ($v_{\perp}$) and deviated particles usually with a smaller size contribute to the lateral Growth velocity ($v_{\parallel}$) [10].
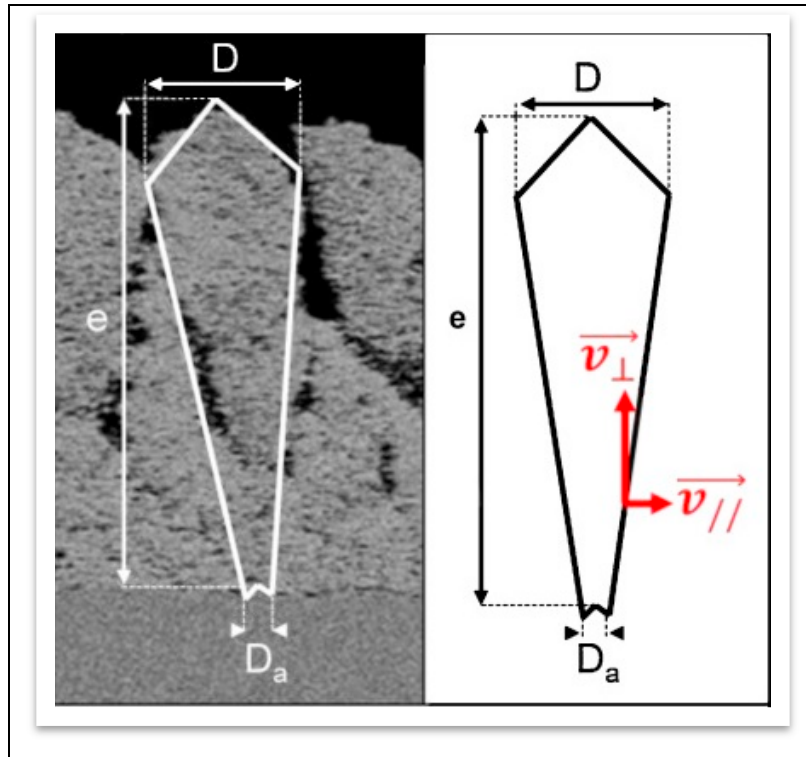
Figure 2-3- The normal ($v_\perp$) and lateral ($v_{||}$) velocities effect in columnar structure [10].

It is presumed that the small particles, which influence the lateral growth velocity have smaller impact angle and the large particles, which influence in the normal growth velocity have greater impact angle, as it is depicted in Figure 2-4.
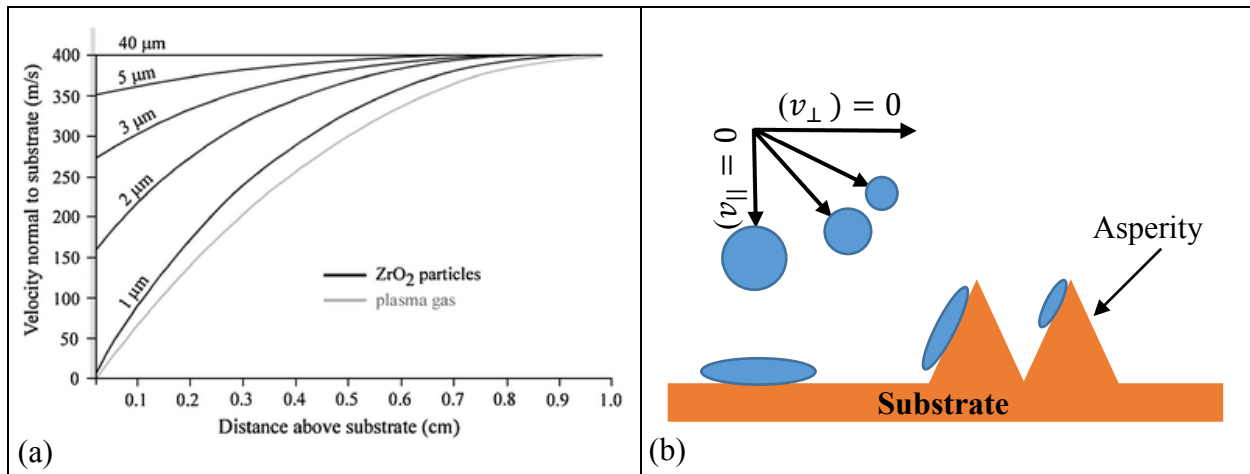
Figure 2-4 (a) The normal velocity component of different diameters of zirconia particles within the plasma [64] (b) and the particle trajectory stemming from particle velocity.

Therefore, later in the next section, different scenarios will be defined based on the impact angle which is a determinative factor in columnar structure evolution. Moreover, the molten particle takes one of the two pancake (disk shape) and flower (disk with splash) forms after impact. Since the Weber number associated with the sub-micron or even few micron-sized particles is rather low, most of the SPS coating particles do not reach the splashing regime and mainly form a pancake shape splats upon impact [9]. The particles will be assumed to solidify at the point of impact. The pancake shape forms after impacting of molten lamella on the substrate. It is assumed that the spherical particle transforms to the disk shape with uniform thickness. So the maximum spread diameter is defined in Eq.2-2 which is raised from a balance between the inertia and capillary force.

$$\zeta = \sqrt{\frac{2d_p}{3h}}$$

2-2

where, d_p and h are mean particle diameter before impact and mean disk thickness [9].

However, in this study, we assumed that the particles stick to the impinged location without spreading and deformation and keep their orginal shape. Also, the particles has the uniform cube shape with the size of $1*1*1$ μm^3.

2.2 Input data

The CFD simulation results of Pourang et al. [14] are used as a sample input data in our simulation. However, the developed algorithm has the capability to use other CFD or experimental data as an input. It is worth mentioning that using the CFD simulation result rather than generating random particle properties enables us to have more realistic results.

2.2.1 CFD simulation data

Pourang et al. [14] reported that the simulated plasma touch is a 3MB Oerlikon-Metco plasma torch gun with 60 % thermal efficiency. It was assumed that the gun has a 20 mm long node and a 6 mm diameter exit nozzle with constant volumetric heat source. Also, the plasma gas is considered as a mixture of Argon and Hydrogen. The plasma gun operating conditions are presented in Table 2.

Table 2 Plasma gun operating conditions.

Plasma gun operation conditions	
Nozzle diameter	6 mm
Arc current	500 A
Arc voltage	60 V
Thermal efficiency	60 %
Ar_H_2 mass flow rate	1.45 g/s

The suspension is injected radially with backward angle of $\theta = 14°$ with respect to the normal plane to the plasma plume as shown in Figure 2-5. It is noticeable that the suspension of yttria stabilized zirconia (YSZ) particles is used with the suspension mass flow rate of 0.5 g/s and suspension concentration of %10 wt., resulting in a suspension jet velocity of 30 m/s.
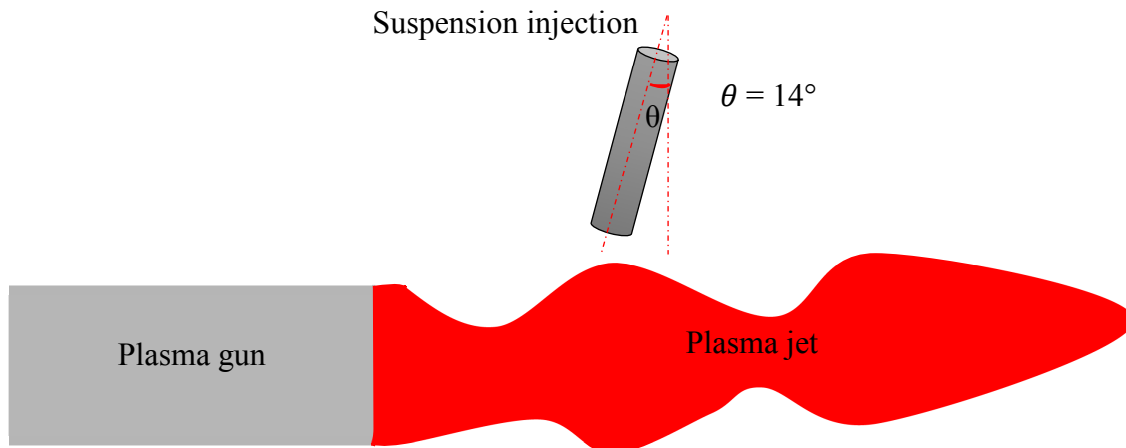
Figure 2-5 Schematic suspension injection into the plasma plume.

The particle's location, size, temperature, and normal velocity distributions at a standoff distance of 4cm are shown in Figure 2-6. It is obvious from this figure that the small size particles with higher temperature and higher normal velocity impact mostly close to the centerline. In order to record the data, the 25 mm ×25 mm plate is located at a standoff distance of 4 cm from the gun and on the front surface of the substrate (Figure 2-7). The probability density function of particle properties are illustrated in Figure 2-8. It is clear from Figure 2-8 d that the mean particle diameter size is around 1 to 1.5 µm and mostly impact with an oblique angle (less than 90º) above and close to the center line.
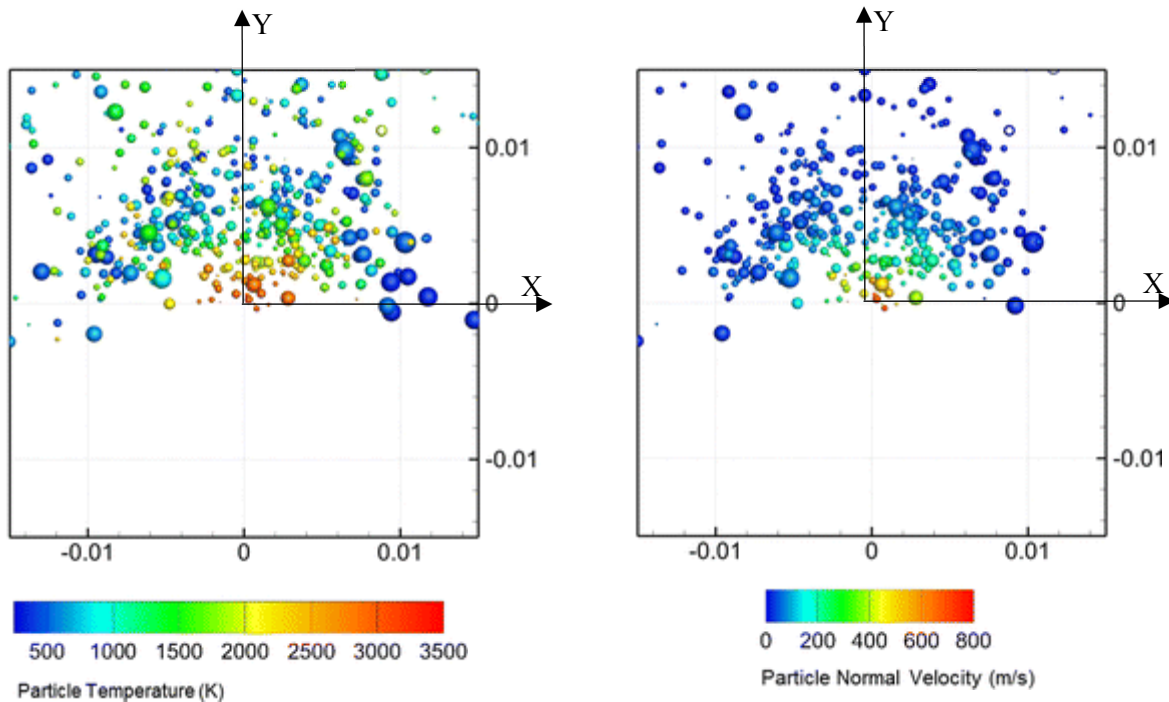
Figure 2-6 Landing location, particle size, temperature and normal velocity distributions at standoff distance of the 4 cm (dimensions are in meters) [14].

Pool of particles
near the substrate
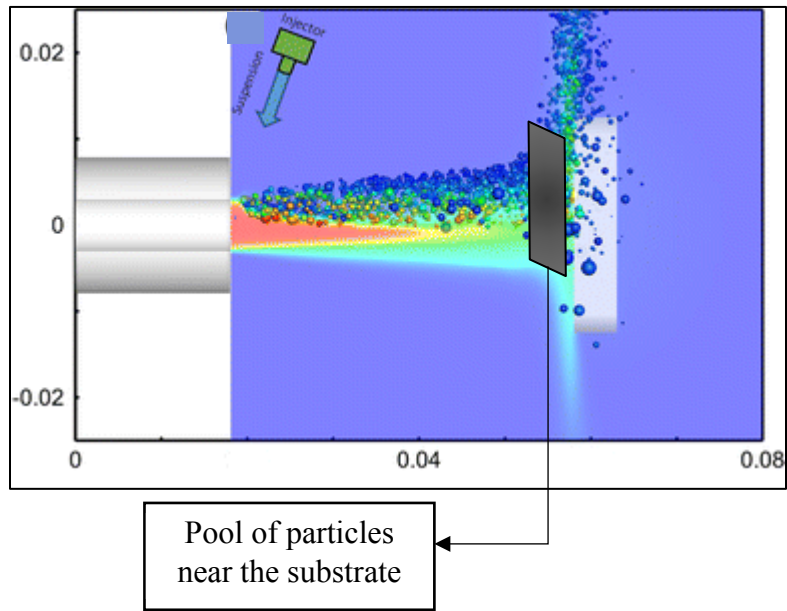
Figure 2-7 Plasma injection CFD simulation (dimensions are in meters) [14].

a) Particle footprint in Y direction (m)

b) Particle normal velocity (m/s)

c) Particle impact angle (degree)

37
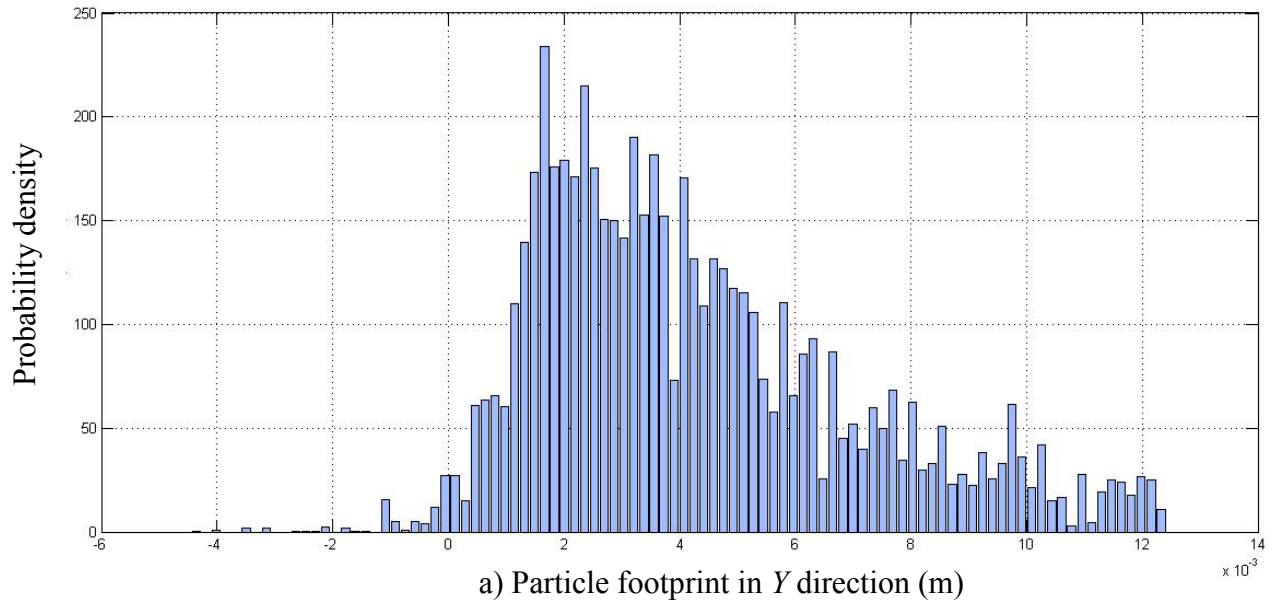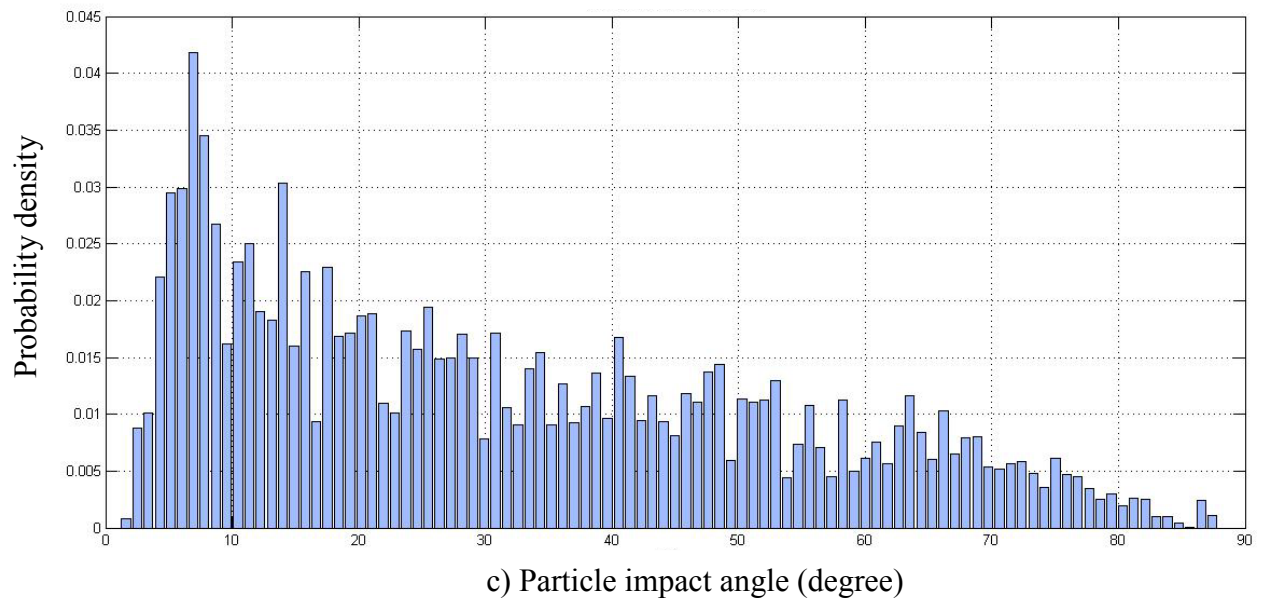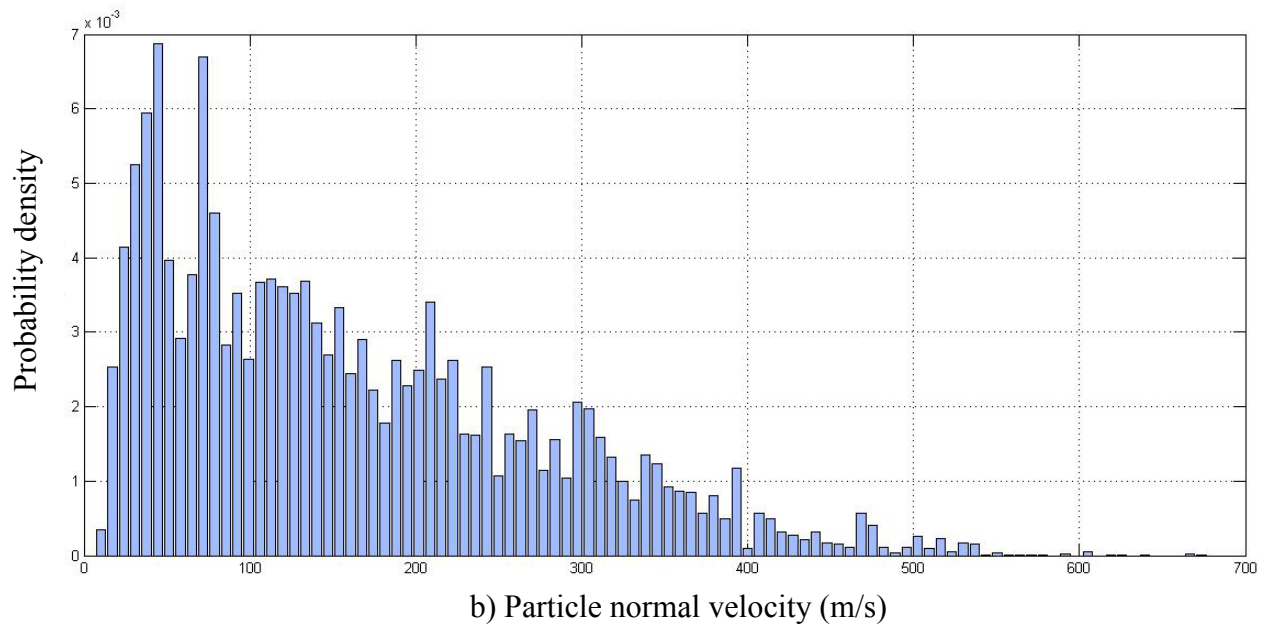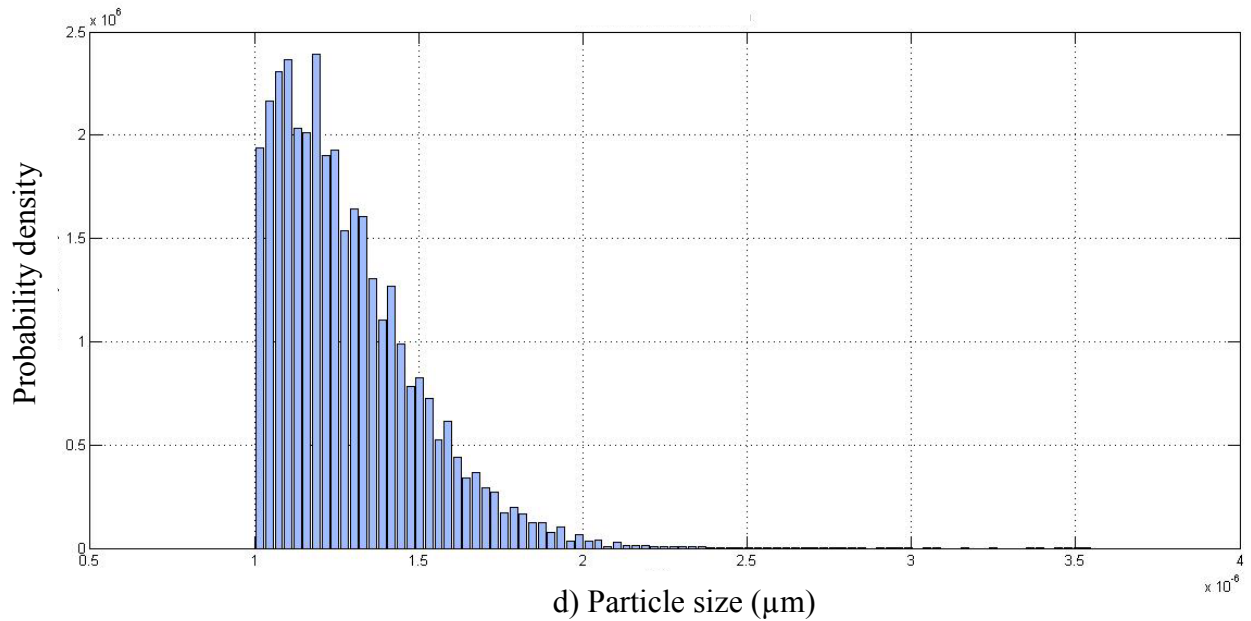
Figure 2-8 Probability density function of (a) particle footprint in *Y* direction, (b) particle normal velocity, (c) particle impact angle, and (d) particle diameter form the CFD simulation of Pourang et al. [14].

2.2.2 Random data selection

In this study, the obtained data from the CFD simulation is used to create the pool of particles at a standoff distance of the 4 cm from the gun and with a 100 µm distance prior to the impact on the substrate. In general, the small particles have higher velocity and temperature compared to the larger ones. The particles are chosen randomly from this pool one after another. The selected particle has specific properties such as size, velocity, impact angle, and temperature. The Pseudo Random Number Generator (PRNG) is used for particles random selection. The PRNG is an algorithm based on mathematical formulas to generate sequences of random numbers. It starts from a seed state which is arbitrary. The random number range is varied according to the number of particles inside our pool. The probability density distribution of particles inside the pool defines

their chance to be chosen as a random particle. The privilege of this method is that the selected particle and corresponding property values are real and are not generated artificially.

2.3 Computational building block

The three-dimensional Cartesian coordinate with hexahedral grid cell of $1*1*1$ μm^3 is used to define the computational building block. The x and y coordinates stand in the substrate plane and the z coordinate is perpendicular to xy plane. The variable $f_{i,j,k}$ is defined to identify the empty and filled cells during the process of coating build-up. It is equal to zero when the cell is empty and equals unity when the cell is filled with material.

$$f_{i,j,k} = \begin{cases} 0 & \text{Empty cell} \\ 1 & \text{Filled cell} \end{cases}$$

2.4 Impinging location

The particles trajectory is an important factor in the coatings structure and columnar morphology. A particle selected from the pool has its own size, x and y coordinates, and velocity. As mentioned above particles in the pool are located at the distance of 100 μm in the z direction from the substrate. The trajectory of particle is calculated based on the particle velocity and its origin location. All cells through the particle trajectory are examined one after another by checking the $f_{i,j,k}$ value. If the cell is empty and $f_{i,j,k}$ is equal to zero the next cell will be tested. The search process is followed until the particle reaches the cell with $f_{i,j,k}$ equals to one. That cell is the final impinging location as illustrated in Figure 2-9.
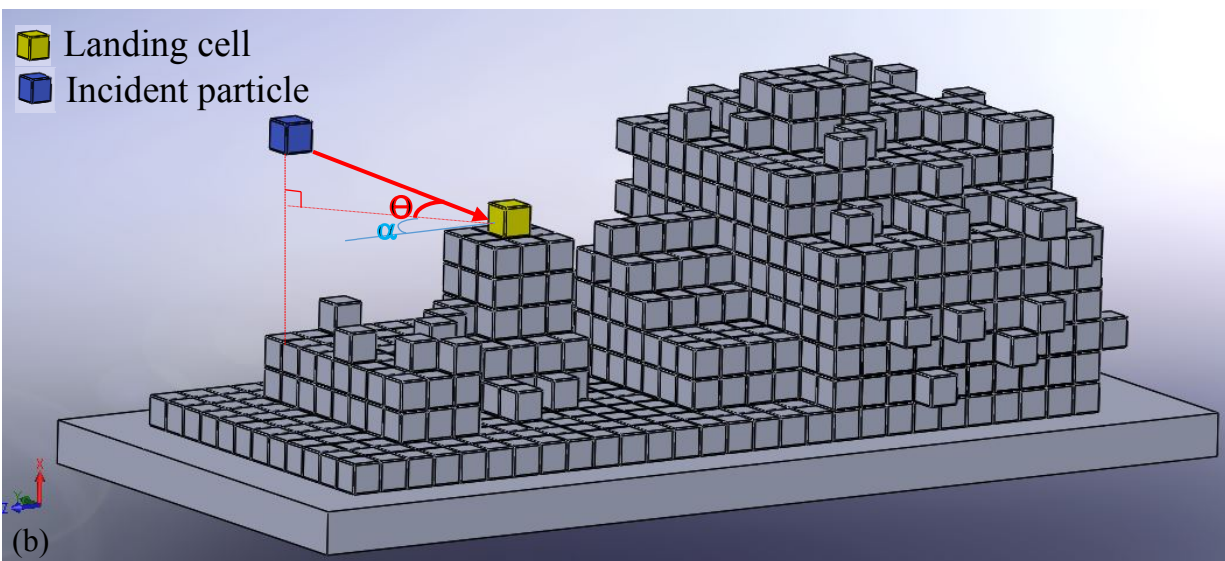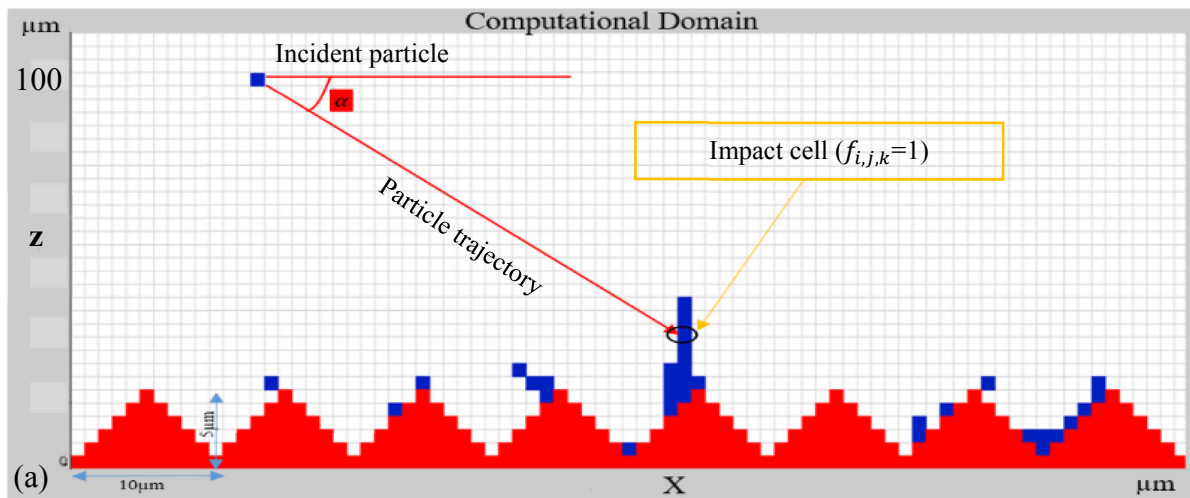
Figure 2-9 Schematic of particle trajectory and landing location in (a) 2D computational domain and (b) 3D computational domain.

Particles are deposited on the landing location based on the prescribed possibilities. Assuming that cell (i,j,k) is the landing cell, according to the different scenarios that will be discussed in the next section, the particle adds to one of the seventeen cells around the landing cell as illustrated in Figure 2-10.
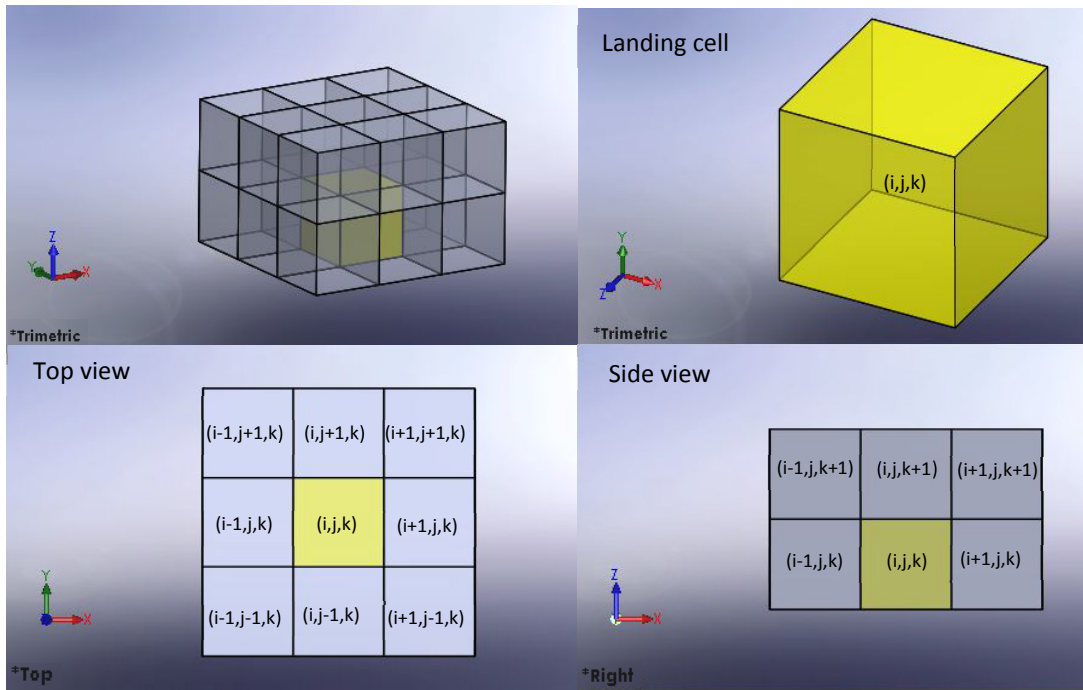
Figure 2-10 Potential cells around the landing cell to add upcoming particle.

2.5 **Scenarios**

To determine the deposited cell, we must first find the side of the landing cell on which the upcoming particle impacts.

As depicted in Figure 2-11, the velocity component in the *x*-direction and the *y*-direction are two determinative factors to find out impact side in the landing cell.
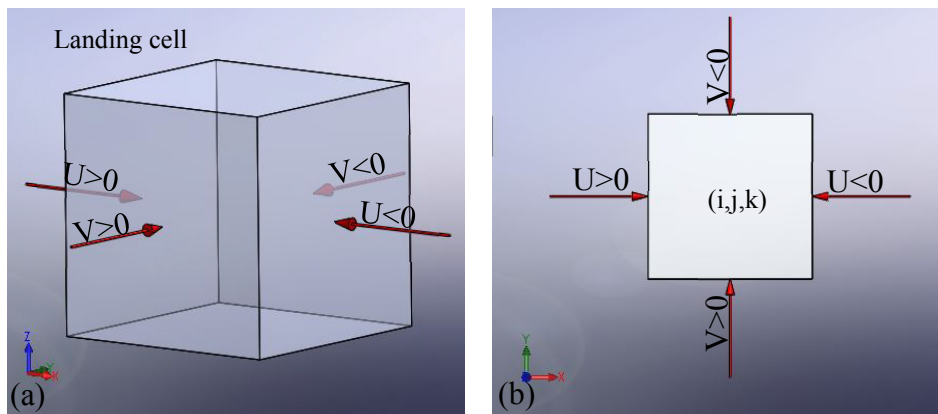
Figure 2-11 Velocity components to determine the possible impact sides in landing cell (a) isometric view, and (b) top view.

41

There are four different possibilities as follows:

Case 1: The velocity in the *x*-direction is larger than zero, and the velocity in the *y*-direction is larger than zero ($U>0$ & $V>0$). So the particle reaches the landing cell toward one of the two specified sides (green ones) as shown in Figure 2-12.
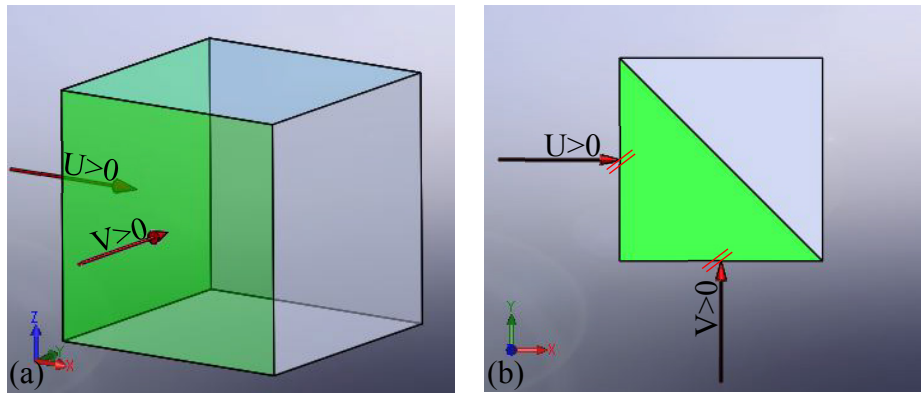
Figure 2-12 Possible impact sides for the case of $U>0$ & $V>0$ (a) isometric view and (b) top view.

Case 2: The velocity in the *x*-direction is larger than zero, and the velocity in the *y*-direction is less than zero ($U>0$ & $V<0$). Therefore, the particle reaches the landing cell toward one of the two specified sides (green ones) as shown in Figure 2-13.
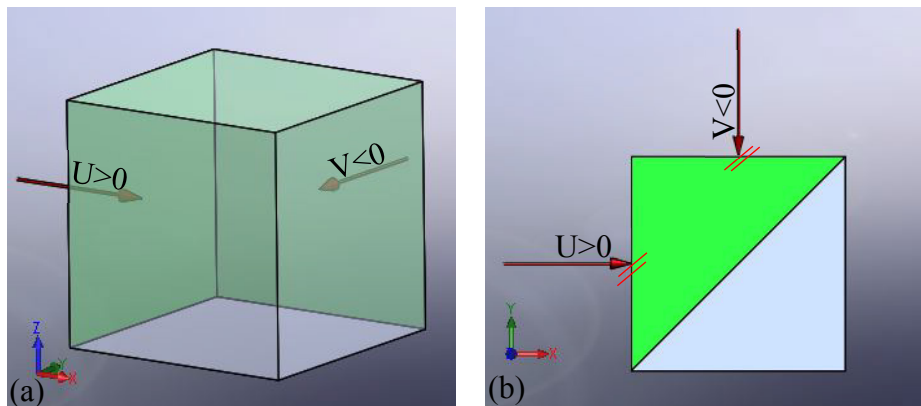
Figure 2-13 Possible impact sides for the case of $U>0$ & $V<0$ (a) isometric view and (b) top view.

Case 3: The velocity in the x-direction is less than zero, and the velocity in the y-direction is less than zero ($U<0$ & $V<0$). Therefore, the particle reaches the landing cell toward one of the two specified sides (green ones) as shown in Figure 2-14.
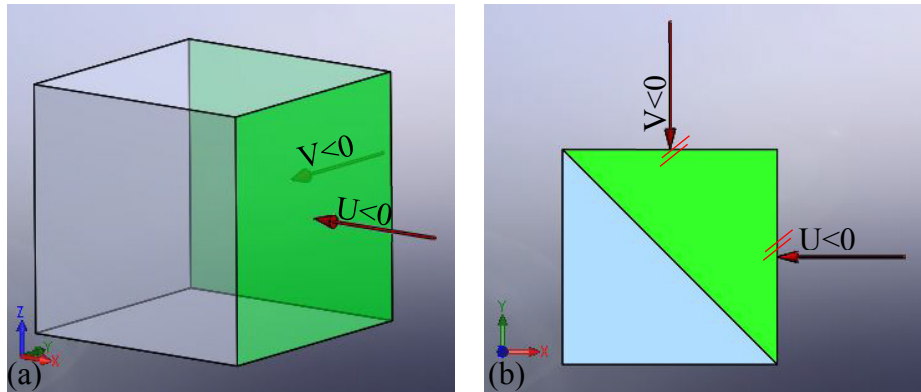
Figure 2-14 Possible impact sides for the case of $U<0$ & $V<0$ (a) isometric view and (b) top view.

Case 4: The velocity in the x-direction is less than zero, and the velocity in the y-direction is larger than zero ($U<0$ & $V>0$). Therefore, the particle reaches the landing cell toward one of the two specified sides (green ones) as shown in Figure 2-15.
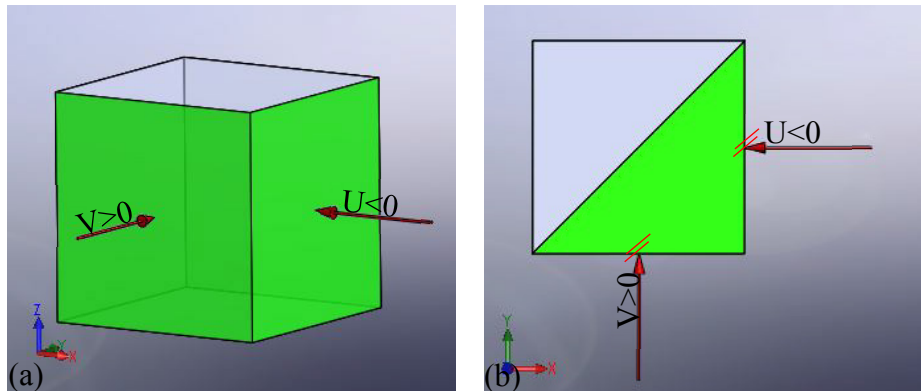
Figure 2-15 Possible impact sides for the case of $U<0$ & $V>0$ (a) isometric view and (b) top view.

In order to narrow down our choices and select one of the two possibilities in the above mentioned conditions, a variable should be defined as the ratio of velocity in the y-direction, v, to the velocity in the x-direction, u, as shown in Eq.2-3.

$$\text{Slope=tan } \alpha = \left| \frac{v}{u} \right| \qquad \qquad \text{2-3}$$

If the velocity in the *y*-direction is larger than velocity in the *x*-direction, the particle impacts on

the side normal to the *y*-direction and vice versa as shown in Figure 2-16 and Figure 2-17.
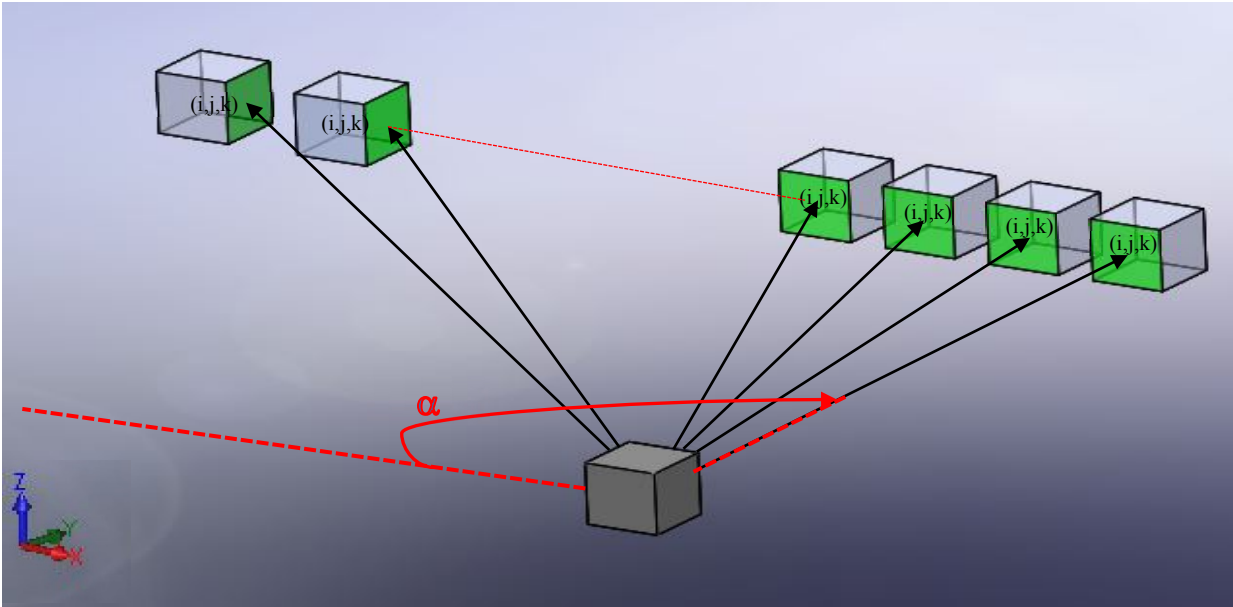
Figure 2-16 Final impact side regarding the velocity component relation (Isometric view).

Also, the top view is illustrated in Figure 2-17.
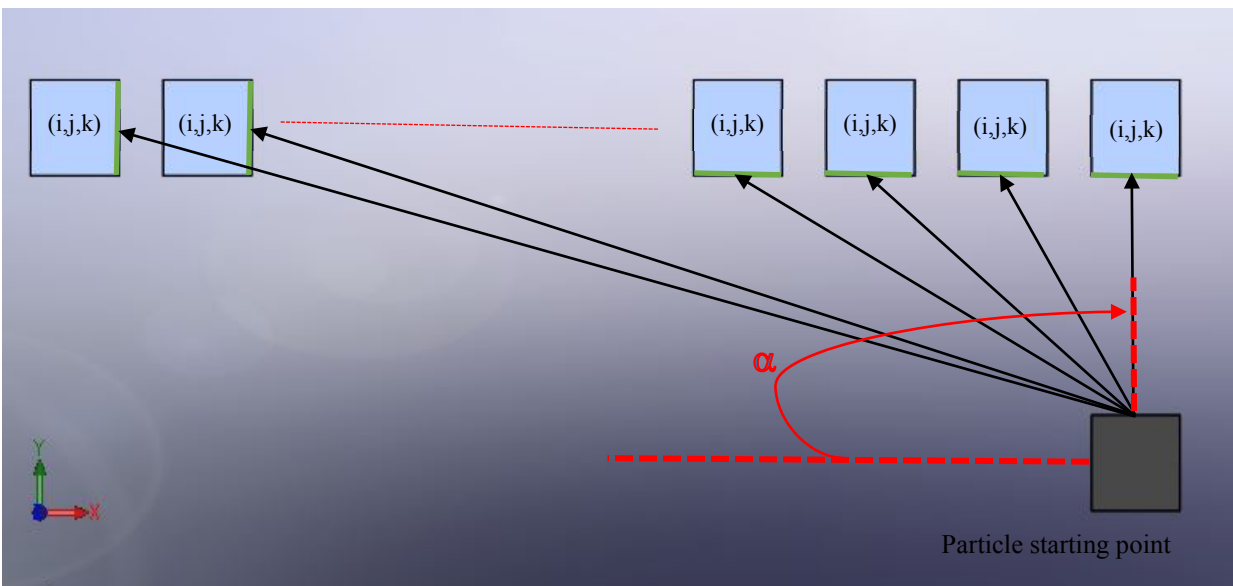
Figure 2-17 Final impact side regarding the velocity component relation (Top view).

For instance, it the velocity in the *x*-direction is less than zero, and the velocity in the *y*-direction is larger than zero (*U<0 & V>0*), there are three different possibilities:

1) If the ratio of velocity in the *y*-direction to that in the *x*-direction is between zero and 0.577 (0≤slope<.577, 0°≤α<30°), the particle reaches the landing cell from the right side. It sticks either to one of the next right column cells or on top of the landing cell as seen in Figure 2-18.
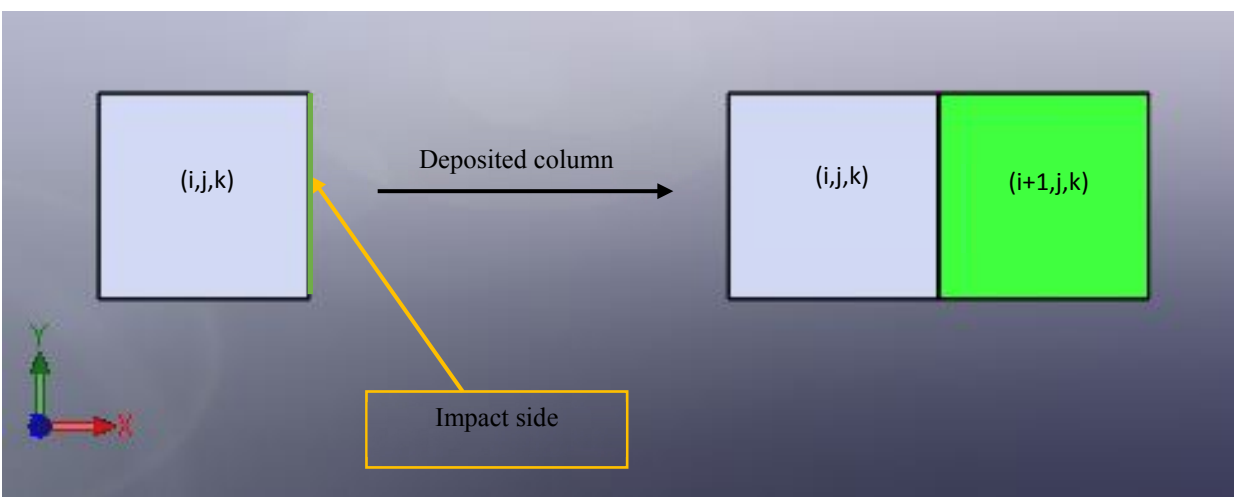
Figure 2-18 Impact side and possible deposited cells for the case of 0°≤α<30°.

2) If the ratio of velocity in *y*-direction to that in the *x*-direction is between 0.577 and 1.732 (0.577≤slope≤1.732, 30°≤α≤60°), the particle reaches the landing cell from the corner. It sticks either to one of the next bottom right corner column cells or on top of the landing cell as shown in Figure 2-19.
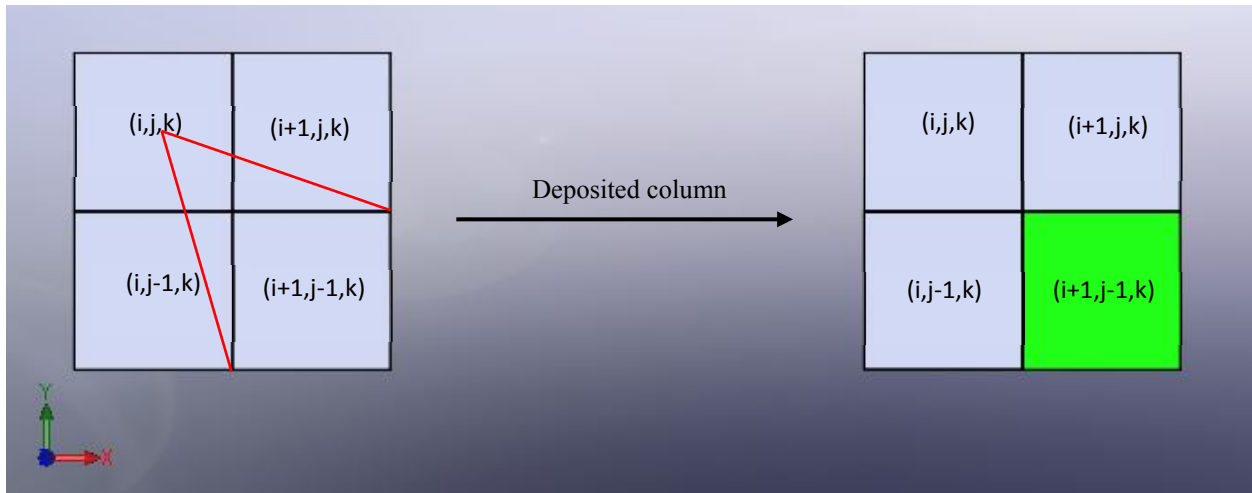
Figure 2-19 Impact side and potential deposited cells for the case of 30°≤α≤60°.

3) If the ratio of velocity in the *y*-direction to that in the *x*-direction is bigger than 1.732 (slope≥1.732, 60°<α≤90°), the particle reaches to the landing cell from the bottom. It sticks either to the next bottom column or on top of the landing cell as can be seen in Figure 2-20.
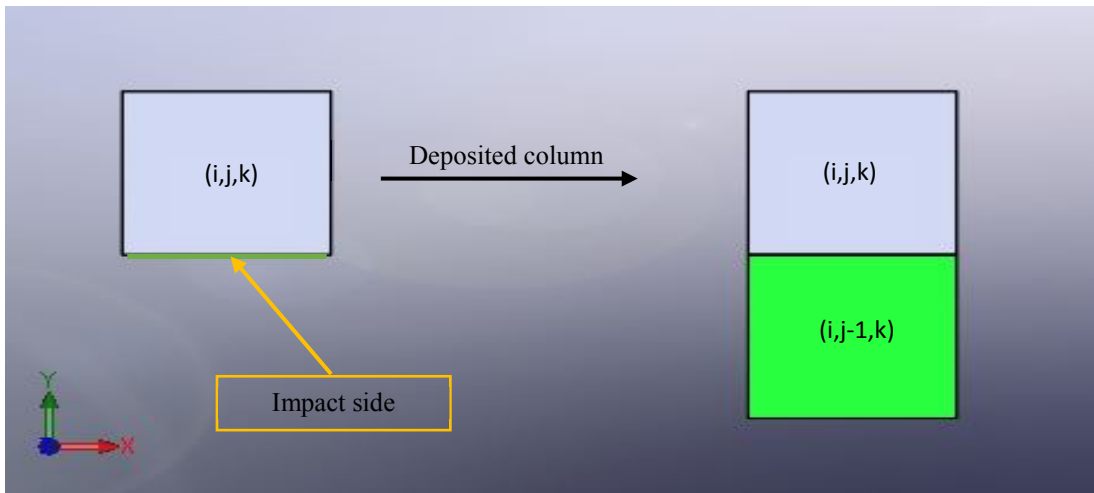
Figure 2-20 Impact side and potential deposited cells for the case of 60°<α≤90°.

In the final step, when the landing cell (cell (*i,j,k*)) and the impact side are known, we have to decide which cell to add the particle on that side. In this step, the coating thickness ($h(i,j)$) and the landing cell height (h_{impact}) as well as impact angel (Θ) are the determinative factors to define

the scenarios to add the particle on the impact side. The two possible conditions are; the coating thickness is larger than landing cell height (h(i,j)> h_{impact}) and equal to that (h(i,j) =h_{impact}).

To determine the deposited cell, these two conditions ($h(i,j)$ = h_{impact} and $h(i,j)$ >h_{impact}) in different impact angles for each twelve conditions discussed before must be evaluated separately. In the following section we only present one specific condition as an example, in which the velocity in the x and y-directions are less than zero, and their ratio is between zero and 0.577 (U<0, V<0, 0°≤α<30°).

i. $h(i,j) = h_{impact}$

If the coating thickness at i,j is equal to landing cell height illustrated in Figure 2-21, three conditions are defined based on the impact angle to define the deposited cell.
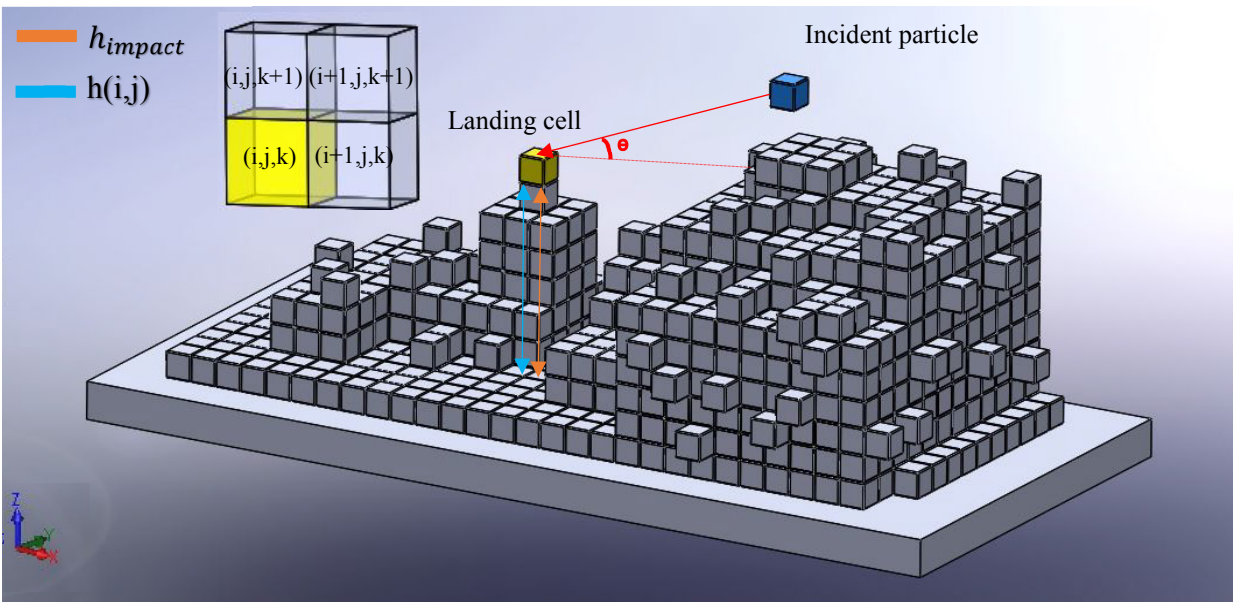
Figure 2-21 Possible deposited cells for the case of U<0, V<0, 0°≤α<30°, and $h(\mathrm{i},\mathrm{j})$ = h_{impact}.

47

a) Impact angle $0°\leq\theta<30°$

For $0°\leq\alpha<30°$, the particle impacts the landing cell from the right side in the same height. It sticks to that location and fills that cell as shown in Figure 2-22. If the landing cell is (i,j,k), then $f_{i+1,j,k}$ will be one or in fact cell $(i+1,j,k)$ will be filled.
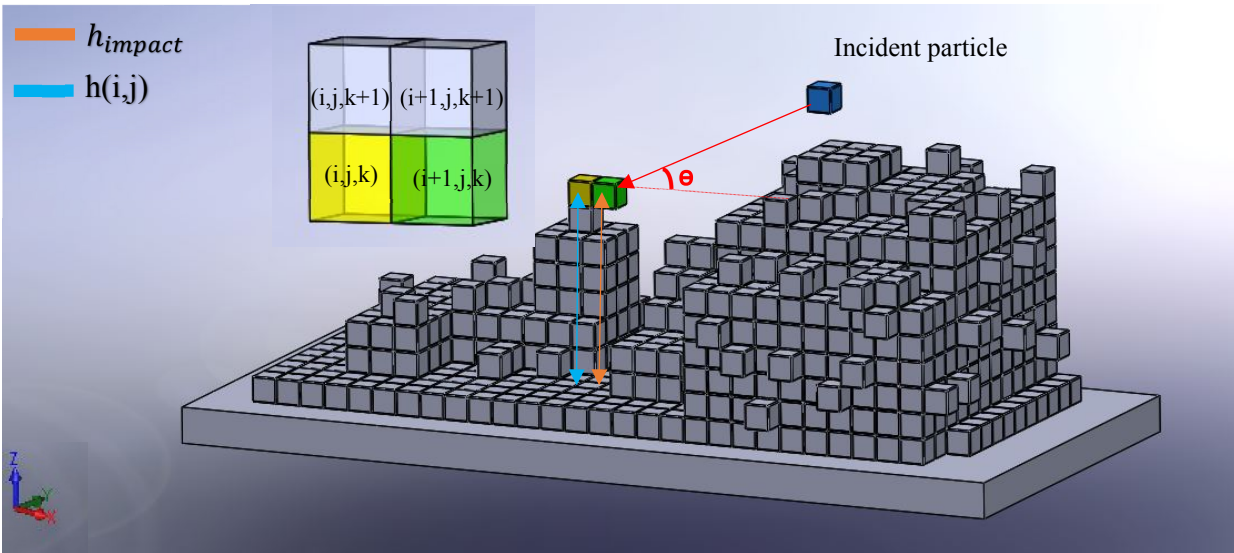
Figure 2-22 Deposited cell for the case of U<0, V<0, $0°\leq\alpha<30°$, $0°\leq\theta<30°$ and $h(i,j) = h_{impact}$.

b) Impact angle $30°\leq\theta\leq60°$

For $30°\leq\alpha\leq60°$, the particle impacts the landing cell from the top right side in the same height. It sticks to that location and fills that cell as shown in Figure 2-23. For the impact location of (i,j,k) in this case the cell $(i+1,j,k+1)$ will be filled i.e. $f_{i+1,j,k+1} = 1$.

48
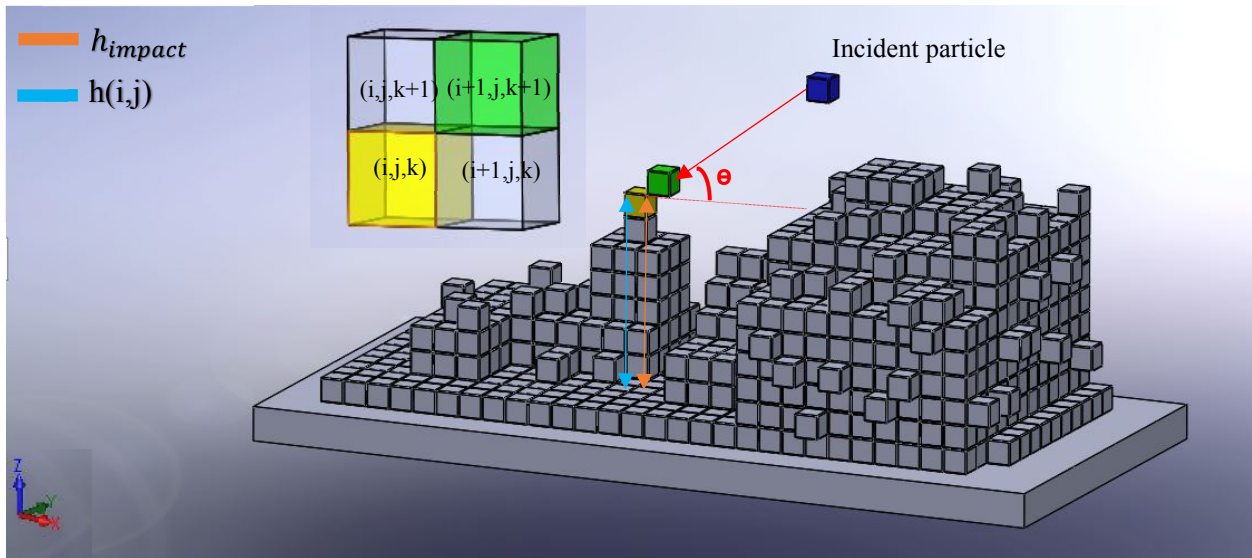
Figure 2-23 Deposited cell for the case of $U<0$, $V<0$, $0°\leq\alpha<30°$, $30°\leq\theta\leq60°$ and $h(\text{i},\text{j}) = h_{impact}$.

c) Impact angle $60°<\theta\leq90°$

For $60°<\alpha\leq90°$, the particle impacts the landing cell from top side in the same height. It sticks to that location and fills that cell as shown in Figure 2-24. For the impact location of (i,j,k) in this case the cell $(i,j,k+1)$ will be filled i.e. $f_{i,j,k+1} = 1$.
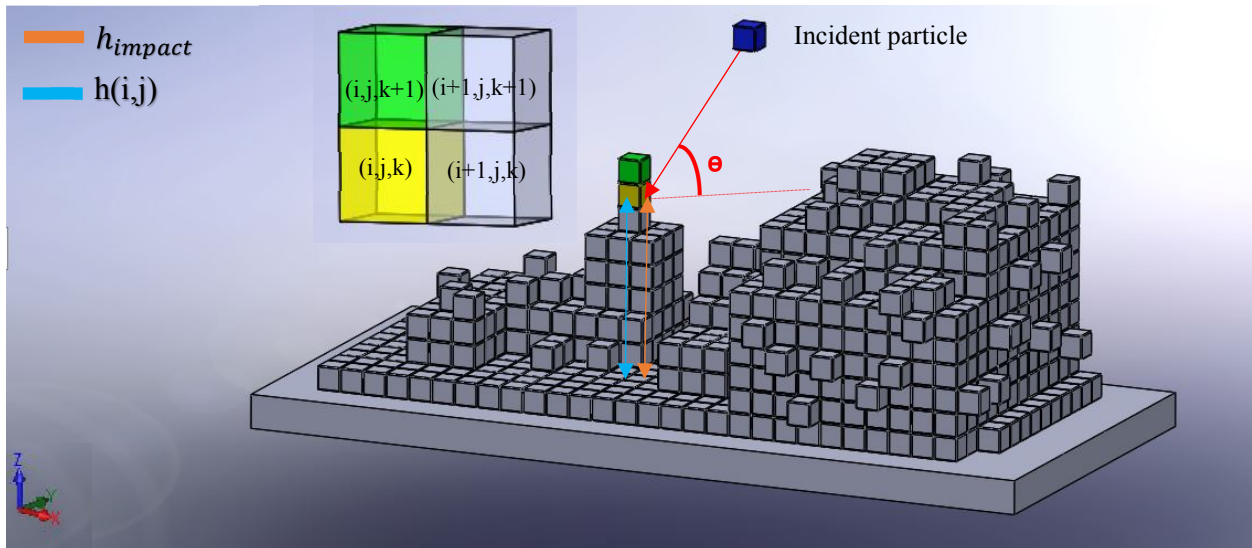
Figure 2-24 Deposited cell for the case of $U<0$, $V<0$, $0°\leq\alpha<30°$, $60°<\theta\leq90°$ and $h(\text{i},\text{j}) = h_{impact}$.

49

ii. $h(i,j) > h_{impact}$

If the coating thickness is larger than the landing cell height as seen in Figure 2-25, two conditions are defined based on the impact angle to determine the deposited cell.
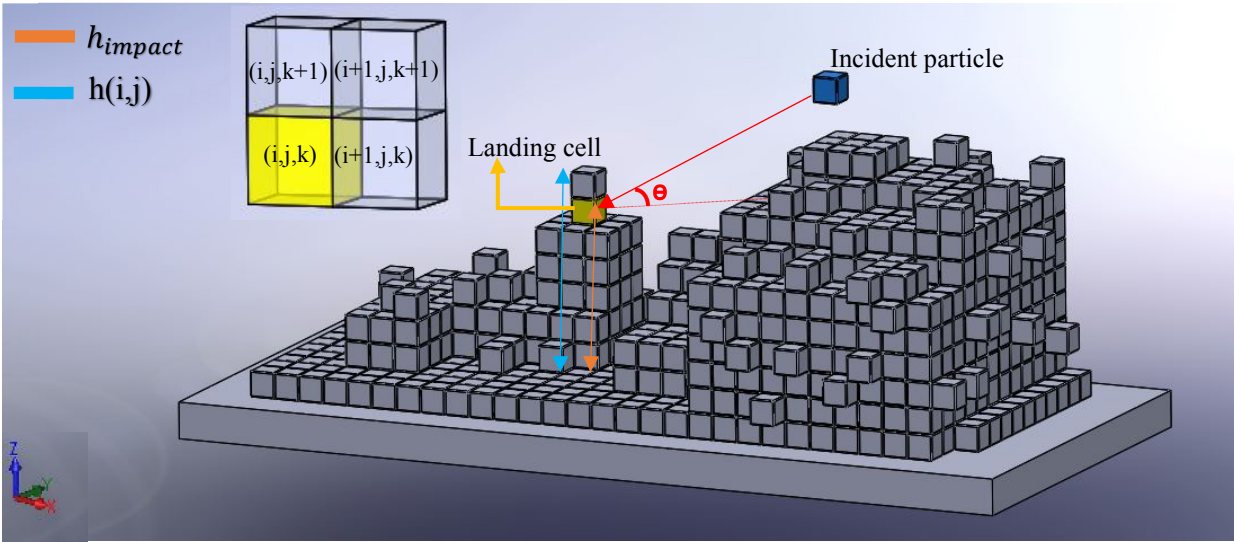
Figure 2-25 Possible deposited cells for the case of $U<0$, $V<0$, $0°\leq\theta<30°$, and $h(i,j) > h_{impact}$.

a) Impact angle $0°\leq\theta\leq45°$

For $0°\leq\alpha\leq45°$, the particle impacts the landing cell from the right side in a lower height. It sticks to that location and fills that cell as shown in Figure 2-26. For the impact location of (i,j,k) in this case the cell $(i+1,j,k)$ will be filled i.e. $f_{i+1,j,k} = 1$.
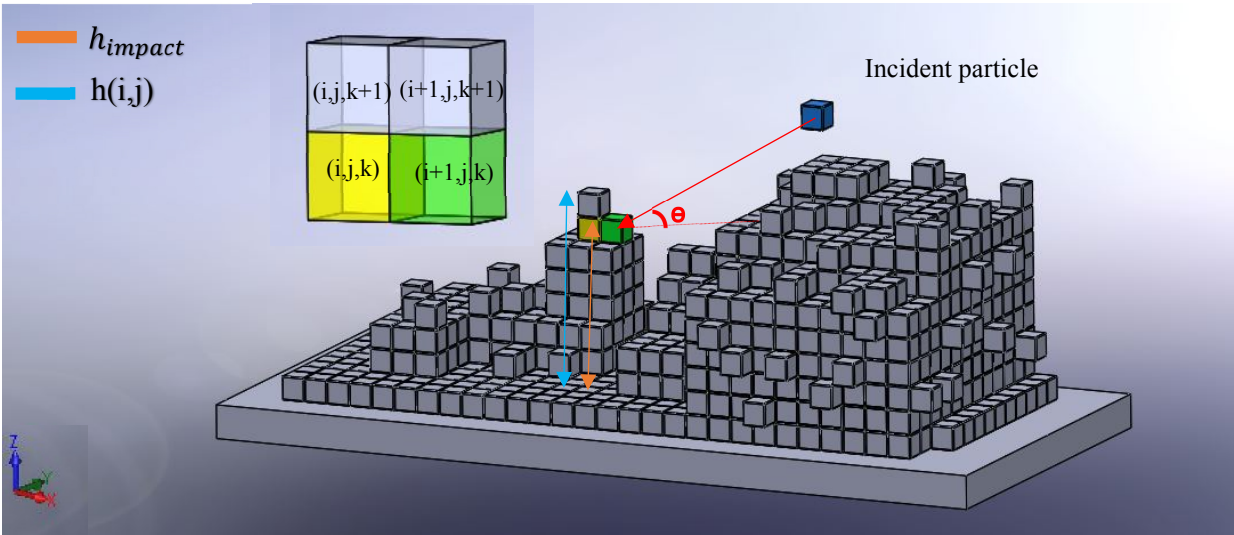
Figure 2-26 Deposited cell for the case of U<0, V<0, 0°≤α<30°, 0°≤θ≤45° and $h(i,j) > h_{impact}$.

b) Impact angle 45°<θ≤90°

For 45°< Θ ≤90°, the particle impacts the landing cell from the top right side in a lower height. It sticks to that location and fills that cell as can be seen in Figure 2-27. For the impact location of (i,j,k) in this case the cell (i+1,j,k+1) will be filled i.e. $f_{i+1,j,k+1} = 1$.
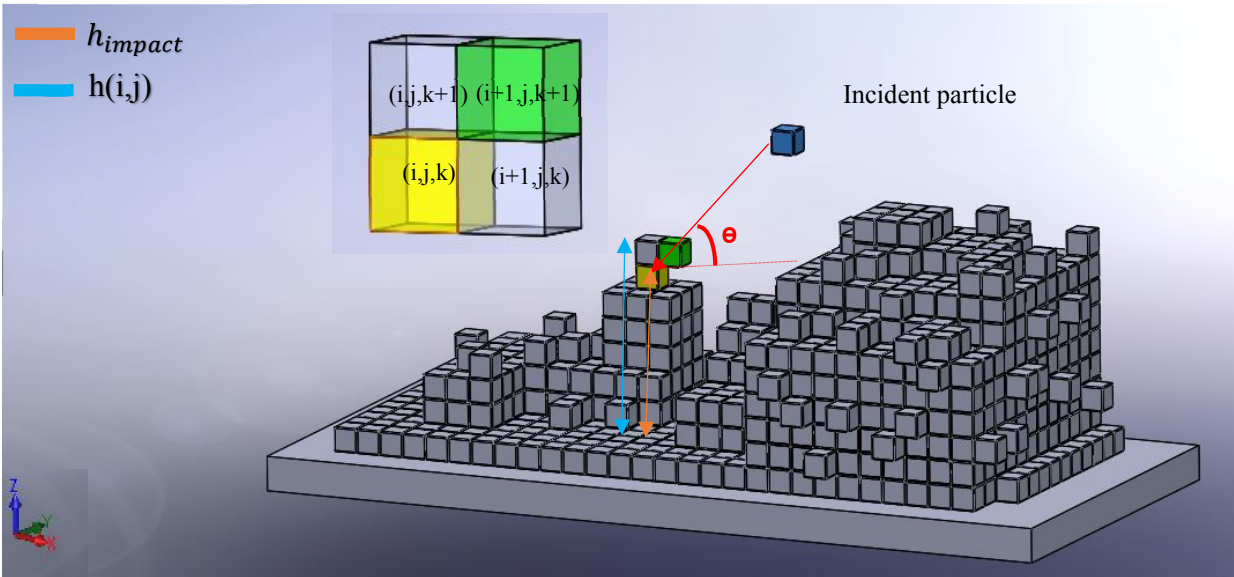
Figure 2-27 Deposited cell for the case of U<0, V<0, 0°≤α<30°, 45°<θ≤90° and $h(i,j) > h_{impact}$.

51

2.6 Substrate structure before coating

The initial substrate roughness typically produced by grid blasting is simulated by arrays of square pyramids in x and y directions with the height and width of 5 μm and 10 μm respectively as illustrated in Figure 2-28.
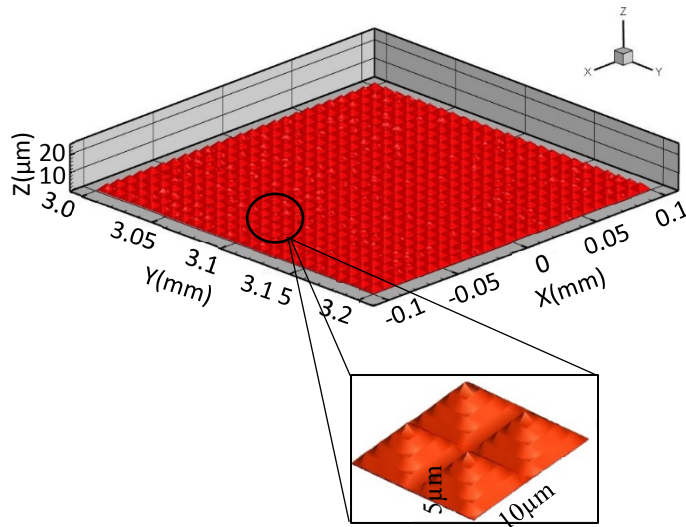
Figure 2-28 Substrate structure before coating.

2.7 Plasma gun movement

In general, during the suspension plasma spray coating process the gun moves continuously. To take into the account the plasma gun movement in our simulation it is assumed that the gun moves laterally in the x direction from left to right with a velocity of 1 m/s as illustrated Figure 2-29. The position of the particles (x_p) at each moment relative to the substrate is calculated by Eq.2-4:

$$x_p = x_{gun} + x_{pr} \qquad\qquad 2\text{-}4$$

where x_{gun} and x_{pr} are respectively the gun position at each moment and position of the particles (x_{pr}) defined in a frame of reference that moves with the gun.

The gun speed value is a user-defined value in the program and we could change it. It is assumed that the gun velocity is 1 m/s which is a typical value for the gun lateral speed.

To decrease the computational time we disregard the full scan, and only consider the gun movement in the x direction so the particles located outside of interest zone are discarded from the pool.
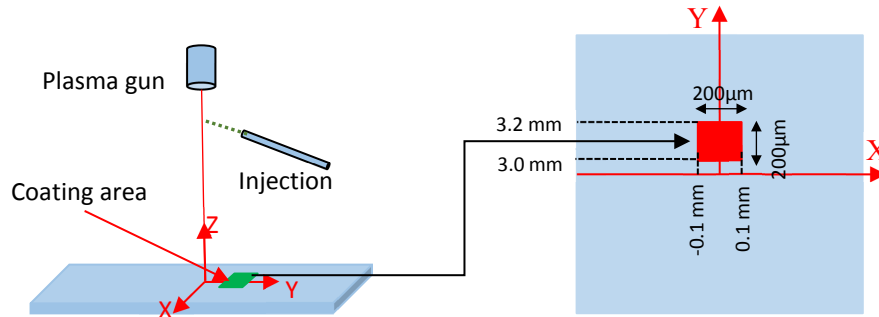
Figure 2-29 Schematic explanation of the gun movement and position and simulated area.

2.8 Computational domain

Since the suspension is injected radially to the plasma plume, the majority of particles impact above the centerline on the substrate as illustrated in Figure 2-6. Also, it is clear from Figure 2-8a that the probability density of particles is significant and more uniform between 2 to 4 mm in the y-direction. Thus, the simulated area is selected in this zone. In this work, the size of the substrate is 25 mm*25 mm. However, the coatings deposition is simulated in a smaller area with the dimension of 200*200 μm^2. This is to manage the size of stored data in a specific level and decrease the computational time. This area is centered along the gun x-axis and 3 mm in the $+y$-direction. In addition, in order to have a more precise simulation in the 200*200 μm^2 area (zone 1), a larger area with a dimension of 600*600 μm^2 (zone 2) is defined (Figure 2-30). This allows us to capture the deposition of those particles which their origin is outside of zone 1 but their impact location may occur in the zone of interest (i.e.zone 1) as shown in Figure 2-31(B.Kashfi). This figure shows the foot print of the particles on the substrate and their trajectories. The origin

53

of arrow and arrowhead represent the origin and the landing location of particle, respectively. It is notable that it would be possible the columnar formation outside of the zone 1 blocks the particles to enter to this zone.
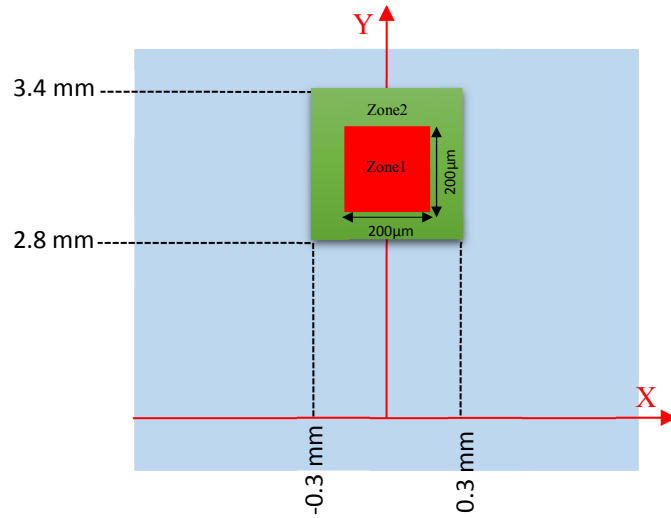
Figure 2-30 Schematic explanation of the area of simulation.
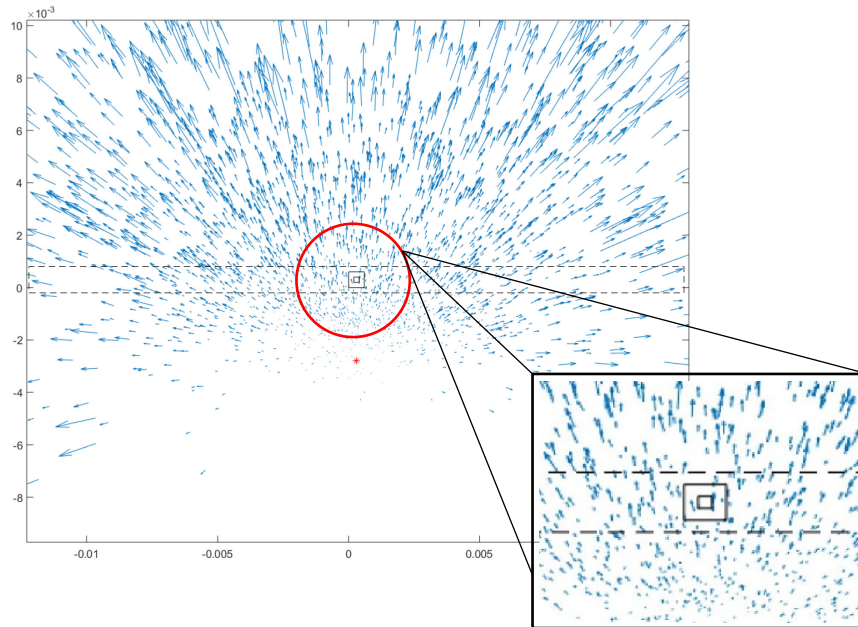
Figure 2-31 The footprint and trajectories of the particles on the substrate.

At each time step, by moving the gun, the location of the particles inside the pool are updated. Then we determine which particles are inside Zone 2. Subsequently, ten particles which are located inside the 600*600 μm^2 area are selected randomly at each time step and their trajectories are calculated to find the landing location to be deposited based on the prescribed scenarios. This process repeats until the gun reaches the end of substrate and this defines one gun pass. Based on the above, the calculations would be repeated for N number of gun passes.

Because of the limitation in the CFD simulation the output data of CFD contains a number of parcels. Each parcel is representative of many particles with the same characteristics. It is mostly possible that only few parcels which contains thousands of particles are located in the zone of interest. Therefore, all particles from one parcel land in the same location and by the gun movement in the x direction, scattered wall-like coatings are built parallel to each other. To tackle this problem, the location of the particles after impact are changed randomly in the y direction between 0 and 100 μm to have full dense coatings.

3 Results

In this chapter, the result of the yttria-stabilized zirconia (YSZ) particles deposition on the flat substrate are presented for the two and three dimensional cases considering the effect of gun movement.

3.1 Two-dimensional results

In this section, Firstly, a two dimensional model with uniform grid spacing in y and z directions is developed to predict the preliminary coating structure using the stationary gun. The Monte Carlo method was used to select each particle properties randomly but the correlation between particles properties is neglected. As can be seen in Figure 3-1 there is a thicker coating near the plasma centerline which is in agreement with Figure 2-8a. The needle like structure is due to parcel-based data resulting from the CFD simulation. Since each parcel contains particles with the same properties, the particles land on the same location resulting in formation of a needle like structure.
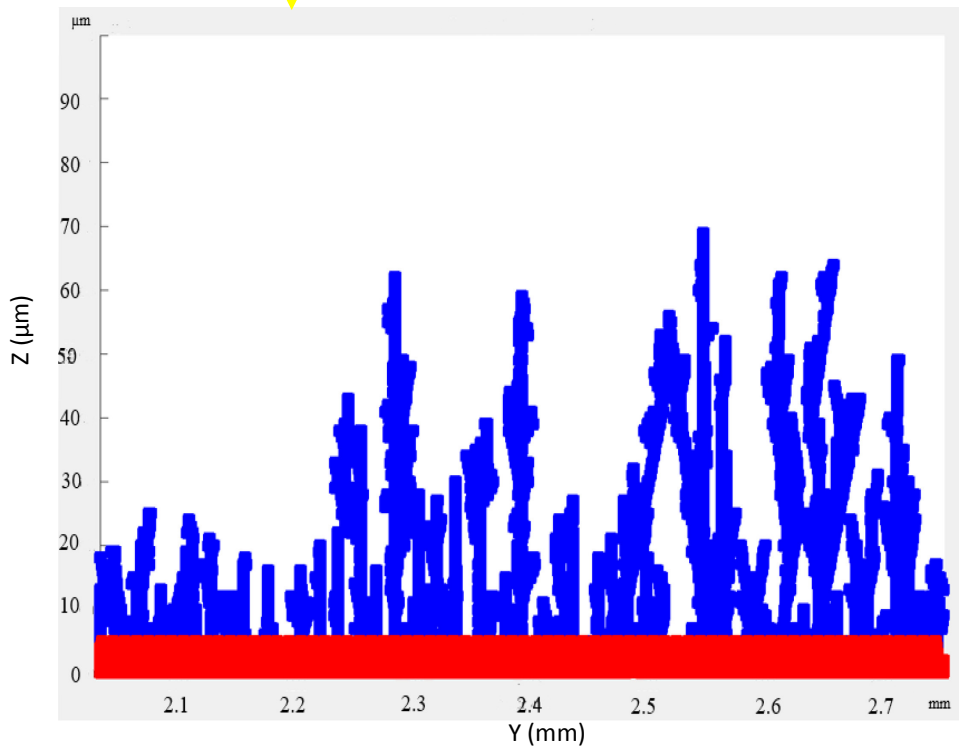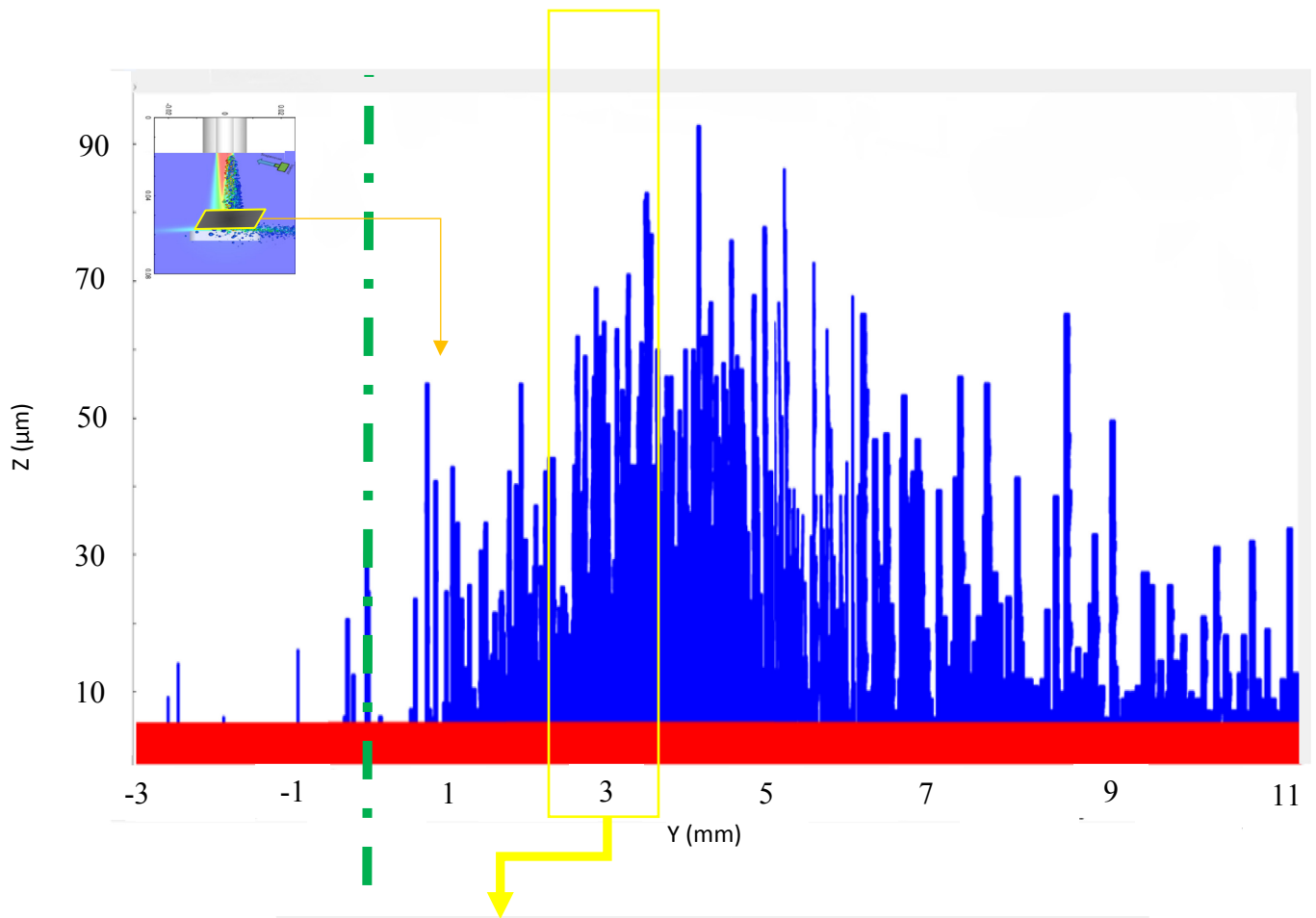
Figure 3-1 2D Coating structure by stationary gun.

Consequently, the simulation is extended to the two dimensional model using a moving gun. The gun moves with a constant velocity of 1 m/s in the x-direction for 3 passes. The gun has a linear movement from left to right, starting from one edge of the substrate to the opposite, to make one pass. The modeling condition and simulated area are presented in Table 3.

Table 3 Modeling conditions.

Modeling conditions	
Gun speed	1 m/s
Number of passes	3
Substrate dimension	25 mm * 25 mm
Time step	10^{-6} s
Simulated area	600 μm*600 μm
Simulated coordinate	X: From -4.60 mm to -4 mm
	Y: From 2.8 mm to 3.4 mm

Figure 3-2 Shows the two dimensional predicted coating structure after 3 passes by Metco-3MB plasma gun.
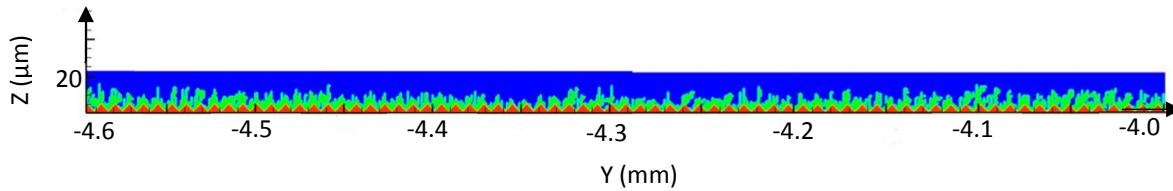
Figure 3-2 2D Coating structure developed by moving gun.

A higher magnification of the two-dimensional results from Figure 3-2 with moving gun is presented in Figure 3-3 a and b two different locations. As can be seen, the mean growth rate of coating thickness is 5 μm per pass which is not compatible with the spray conditions listed in Table 2. The CFD simulation output are in fact 3-D dimensional. However, in the 2-D simulation, a unique particle with x and y coordinates represents all the particles with the same y coordinate but different x coordinates. These particles land on the same location which result a thicker coating as shown in Figure 3-3. In addition, the columnar structure in a real coating structure grows in

different directions which would not be captured in a 2-D simulation. Therefore, it is clear that a two-dimensional model is not able to fully reveal coatings structure.
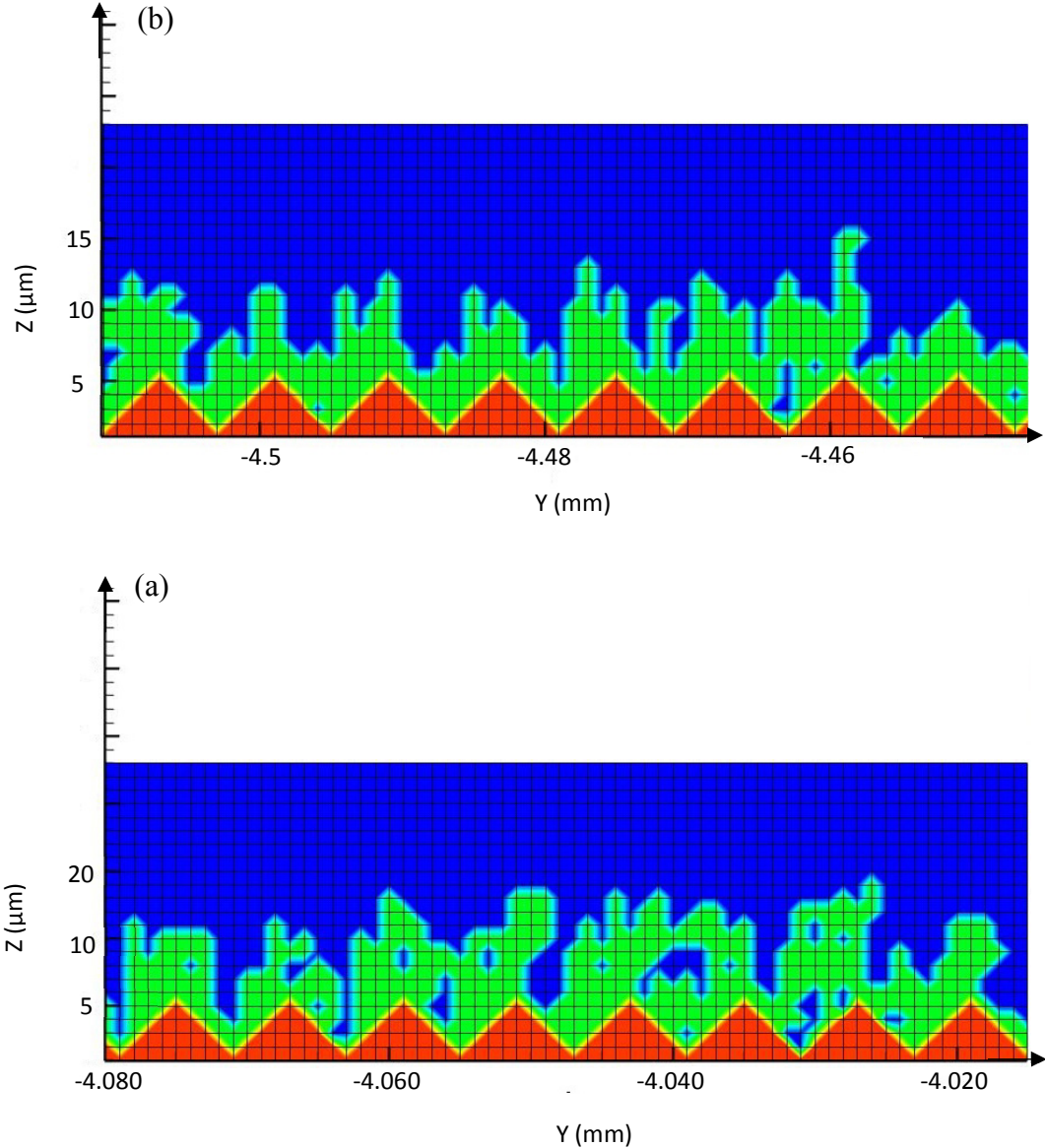
Figure 3-3 2D Coating structure by moving gun at two different locations.

3.2 Three-dimensional results

3.2.1 Coatings condition

Finally, the simulation was developed in the three-dimensional domain with uniform grid spacing in the *x*, *y*, *z* directions. The results of the yttria-stabilized zirconia (YSZ) particles deposition on the flat substrate with the moving gun is presented. The size of the substrate is 25 mm*25 mm. However, the coatings deposition is simulated in smaller area with the dimension of $200*200 \, \mu m^2$ as describe above. This is to manage the size of the stored data in a specific level and decrease the computational time. This area is centered along the gun *x*-axis and 3 mm in the +*y*-direction. The results is from a simulation in which the gun moves a constant velocity of 1 m/s in the *x*-direction for ten passes, with a stand of distance (SOD) of 4 cm. The gun has a linear movement from left to right, starting from one edge of the substrate to the opposite to make one pass. The modeling condition and simulated area are presented in Table 4.

Table 4 Modeling conditions.

Modeling conditions	
Gun speed	1 m/s
Number of passes	10,32
Substrate dimension	25 mm * 25 mm
Time step	10^{-6} s
Simulated area	200 μm*200 μm
Simulated coordinate	X: From -0.1mm to 0.1mm
	Y: From 3.0 mm to 3.2 mm
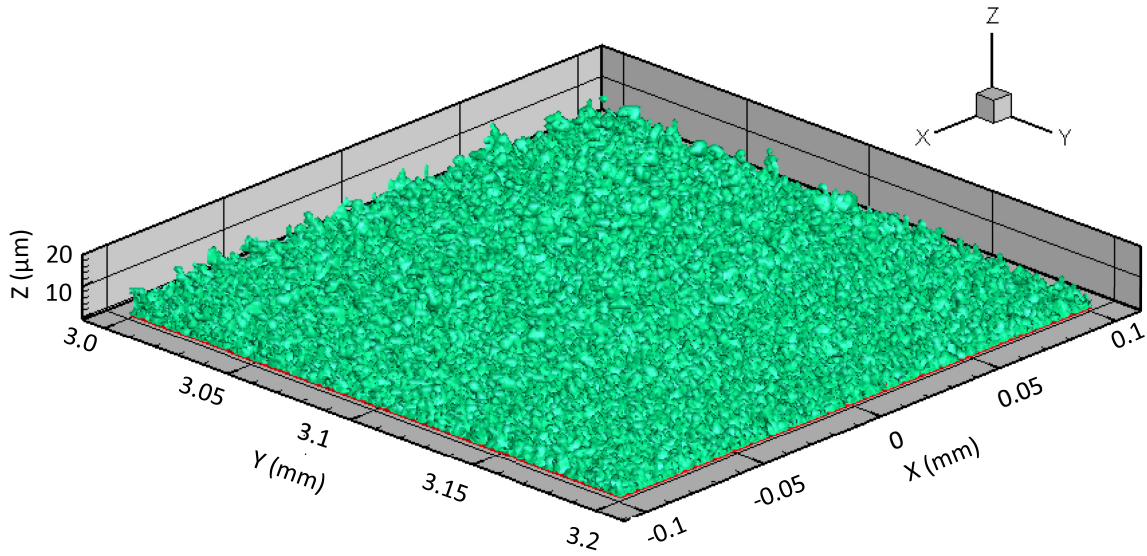
Figure 3-4 3-D Coating structure by moving plasma gun for ten passes.
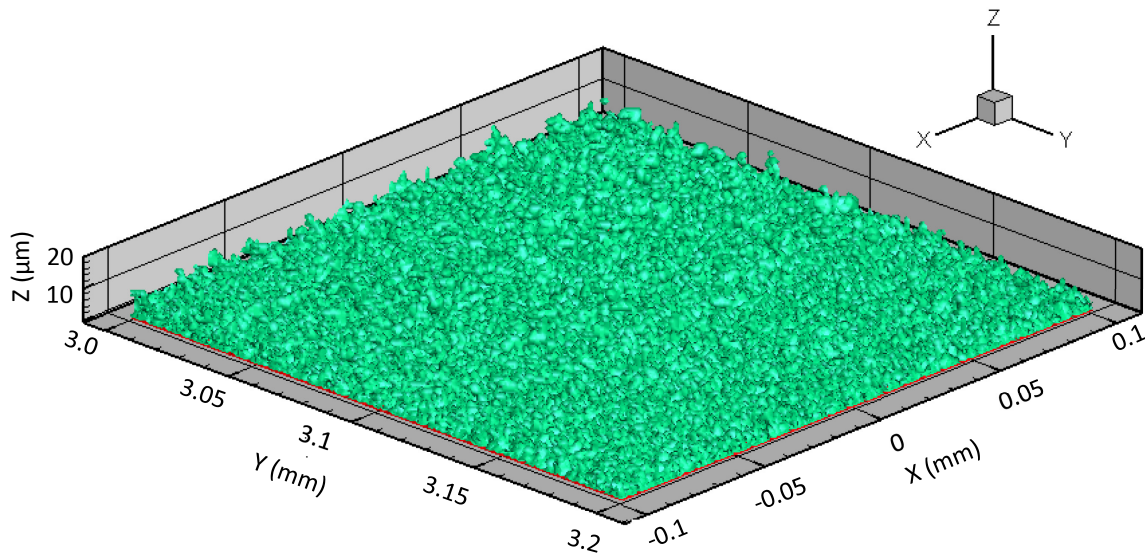
Figure 3-4 shows the three dimensional predicted coating structure after 10 passes. Figure 3-5 shows the *y*-plane and *x*-plane side view of the coating. It seems that the coating thickness is uniform in both directions.

(a)

(b)
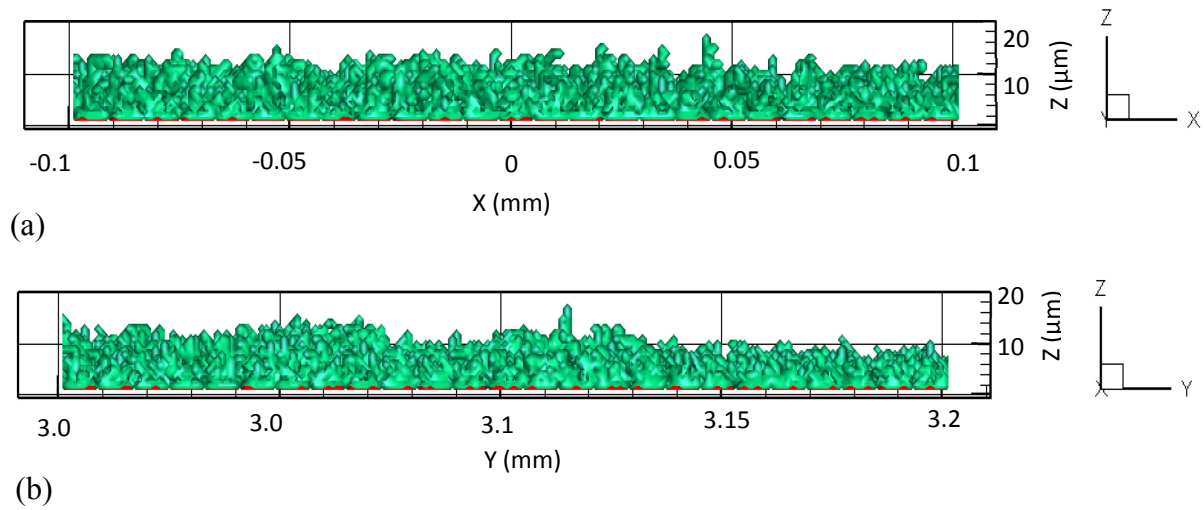
Figure 3-5 Side view of coating structure (a) Y-plane (b) X-plane for ten passes.

A three-dimensional simulation gives us the possibility to take a cross-section through the coating structure at different desired planes. Figure 3-6 shows the *x*-plane and *y*-plane cross-section views of the coating. As it can be seen, the columnar structures form in the *y*-direction from right to left.
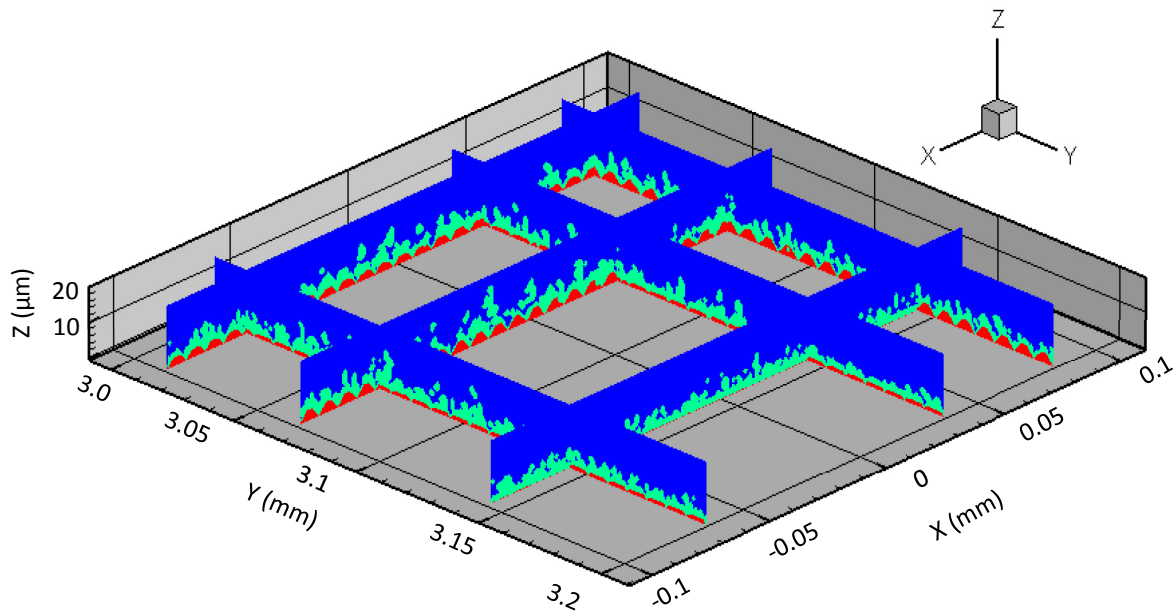
Figure 3-6 Cross-section view of coating structure for ten passes.

Figure 3-7 shows the horizontal cross-section view at various heights of 4, 6, and 9 μm above the substrate. As can be seen in Figure 3-7, the coating density decreased by moving up in *z*-direction. This is due to the fact that the coatings microstructure is formed from bottom to up by stacking of particles on top of each other.

(a)

(b)

(c)
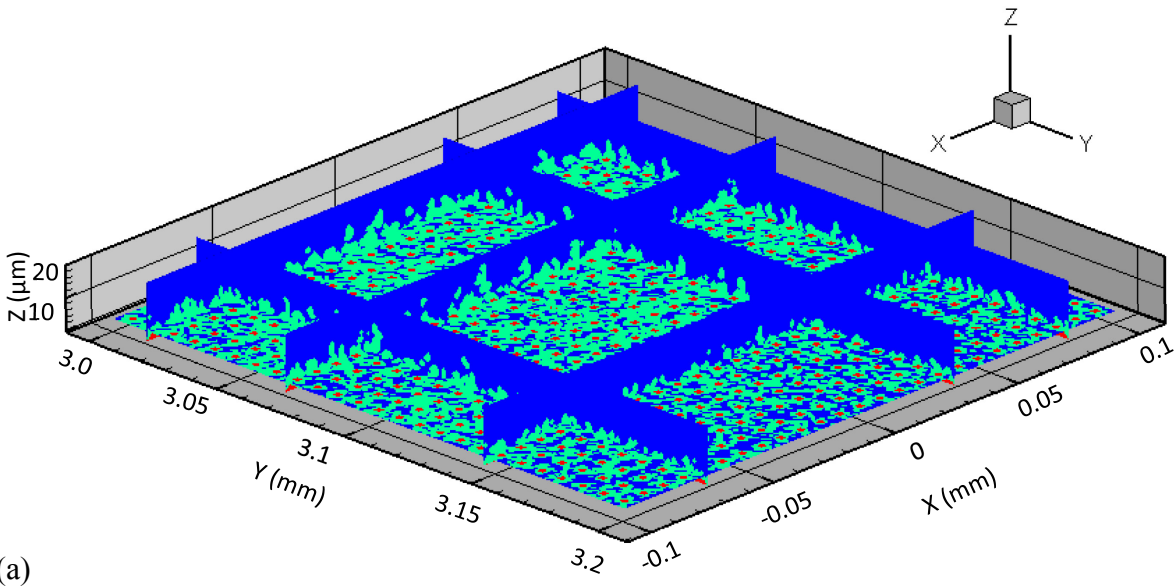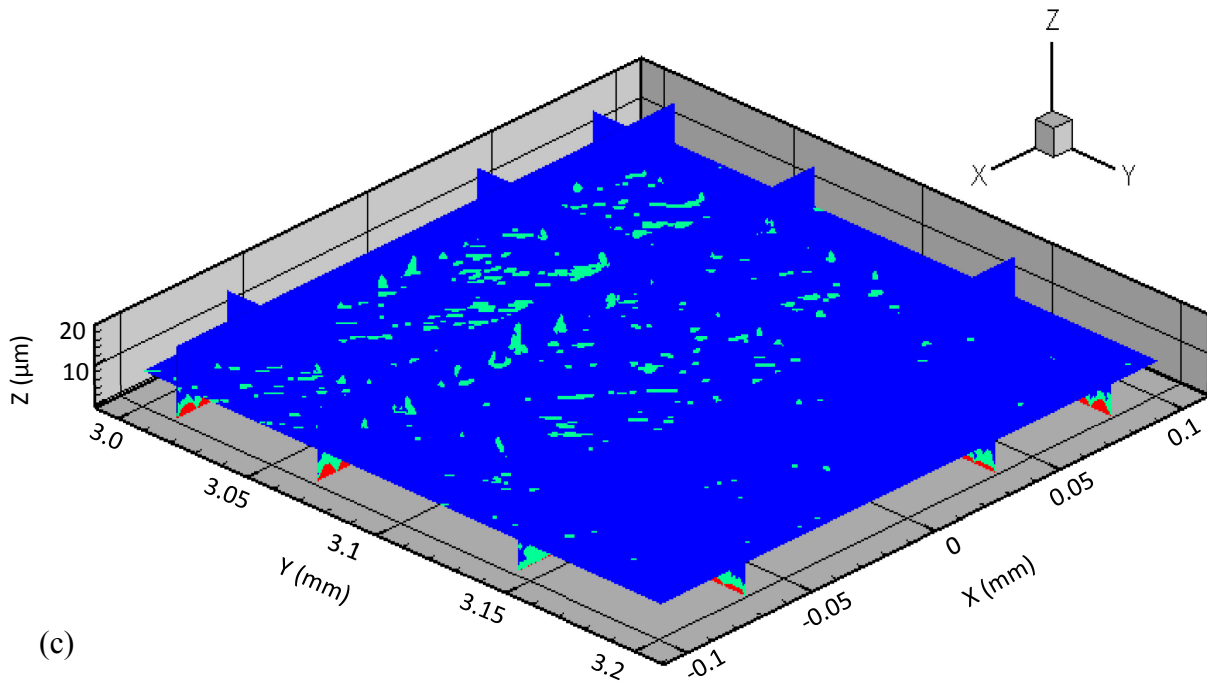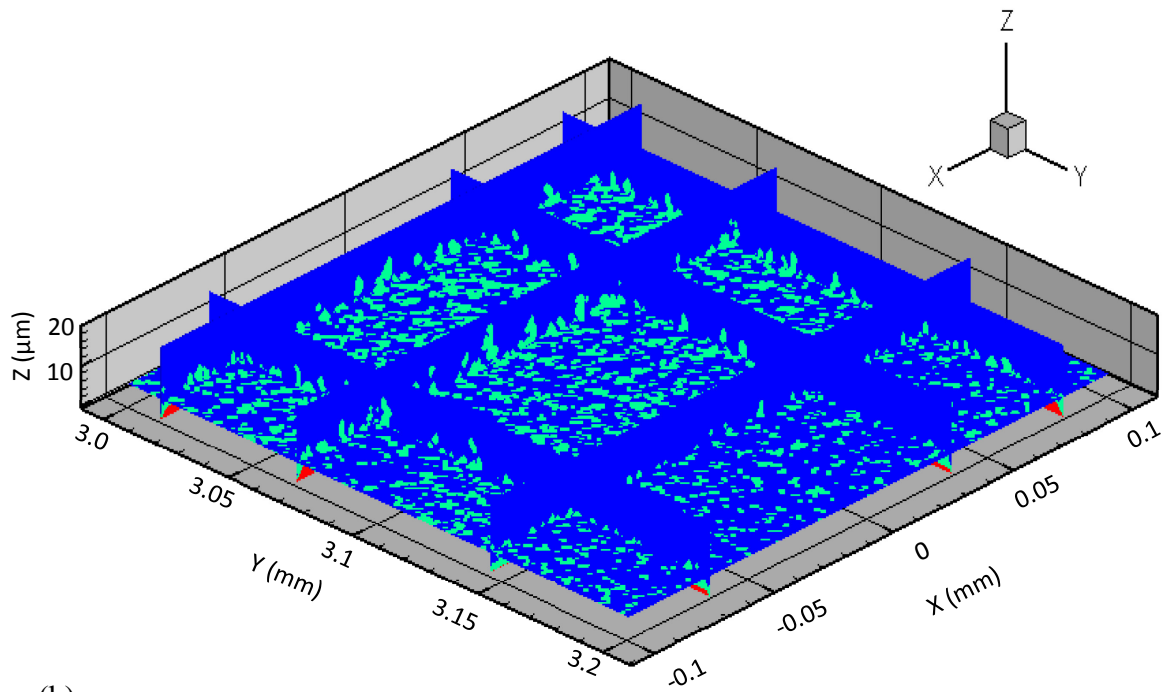
Figure 3-7 Horizontal cross-section view of coating structure at (a) 4 µm (b) 6 µm (c) 9 µm for ten passes.
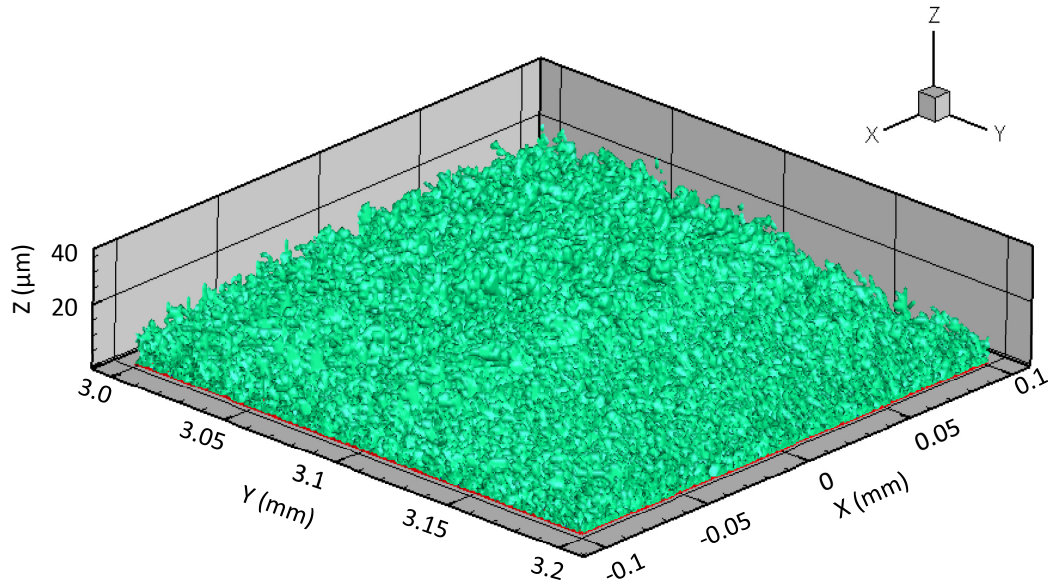
Figure 3-8 3-D Coating structure by moving plasma gun for thirty two passes.

Figure 3-8 shows the three dimensional predicted coating structure after 32 passes. Also, Figure 3-9 shows the *y*-plane and *x*-plane side view of the coating after 32 passes. It seems that the coating thickness is not uniform in both directions which is contrary to our prediction. This could be attributed to the blocking the particles to enter the zone of interest $(200*200\mu^2)$ due to the coatings formation in zone 2 $(600*600\mu^2)$. Also, it could be justified by parcel-based input data resulting from the CFD simulation.

(a)

(b)
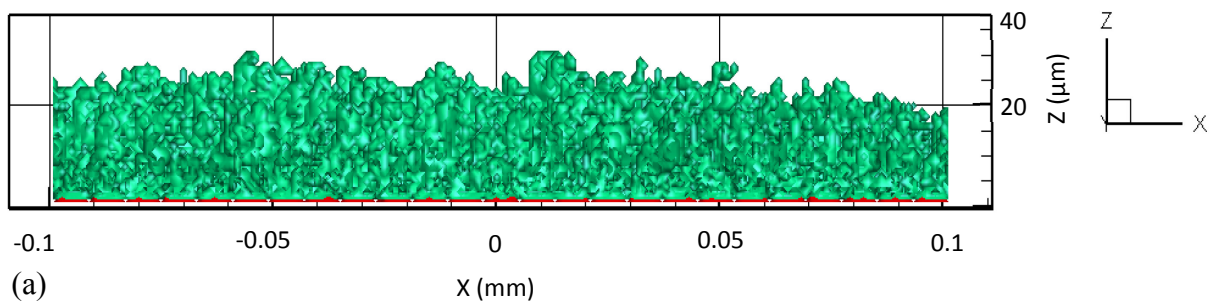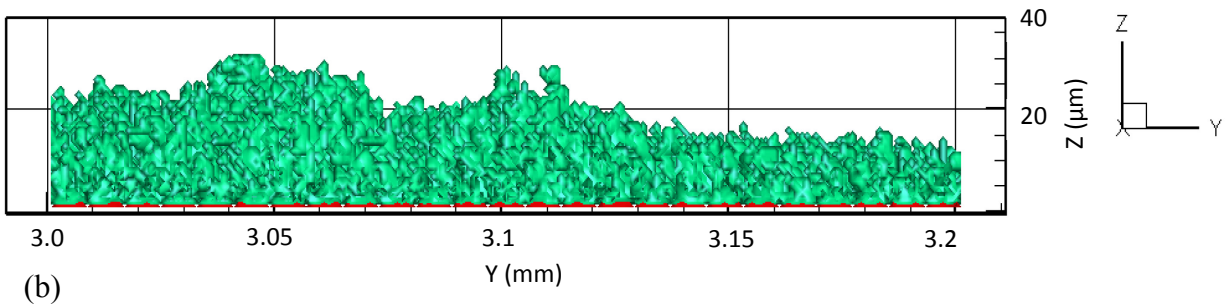
Figure 3-9 Side view of coating structure (a) Y-plane (b) X-plane for thirty two passes.

Figure 3-10 shows the *x*-plane and *y*-plane cross-section views of the coating after 32 passes. As it can be seen, the columnar structures form in the *y*-direction from right to left which is more significant than what it is seen after 10 passes. Moreover, Figure 3-11 shows the horizontal cross-section view at various heights of 4, 6, and 9 μm above the substrate. As can be seen in Figure 3-11, like for the case of ten passes, the coating density decreased by moving up in *z*-direction. This is due to the fact that the coatings microstructure is formed from bottom to up by stacking of particles on top of each other. However, by comparing Figure 3-7 and Figure 3-11, it is obvious that the coating density at the same level is significantly more in the case of coating after 32 passes than that in 10 passes. Thus, an increase in the number of passes not only leads to a thicker coating, but it also results in the higher density at different levels through the thickness.
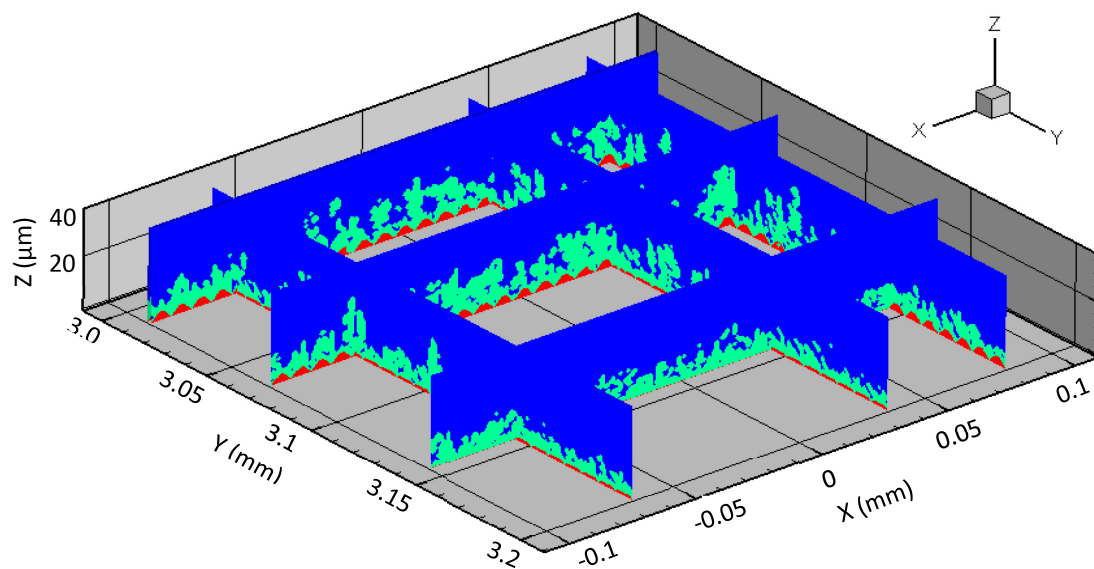
Figure 3-10 Cross-section view of coating structure for thirty two passes.

(a)

(b)

(c)
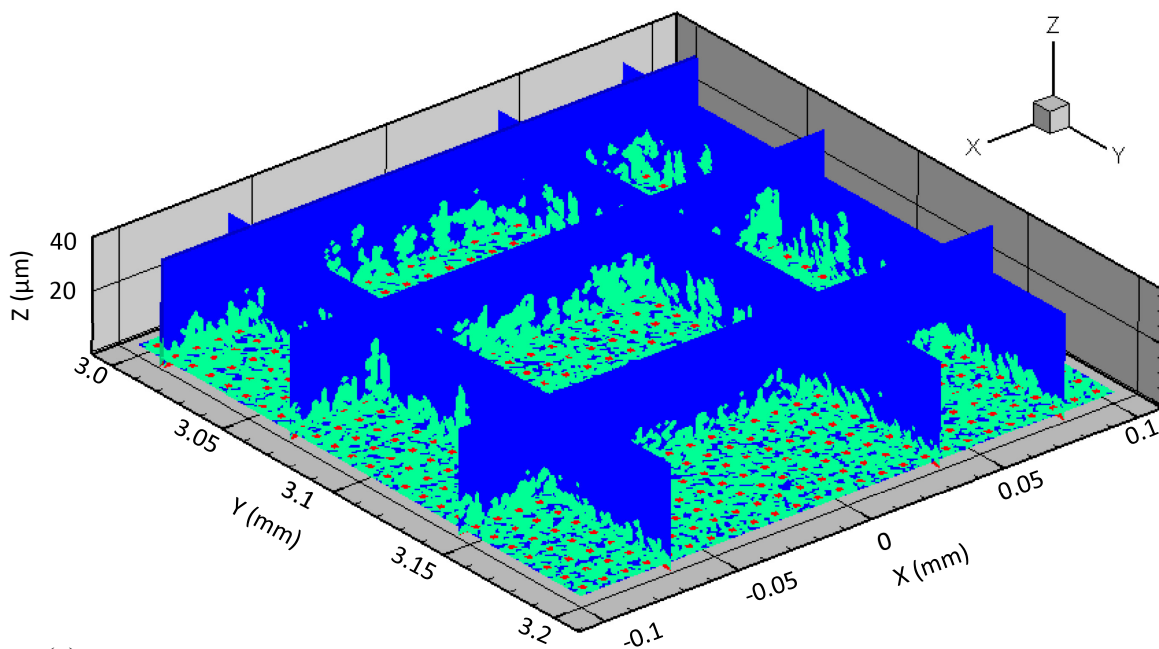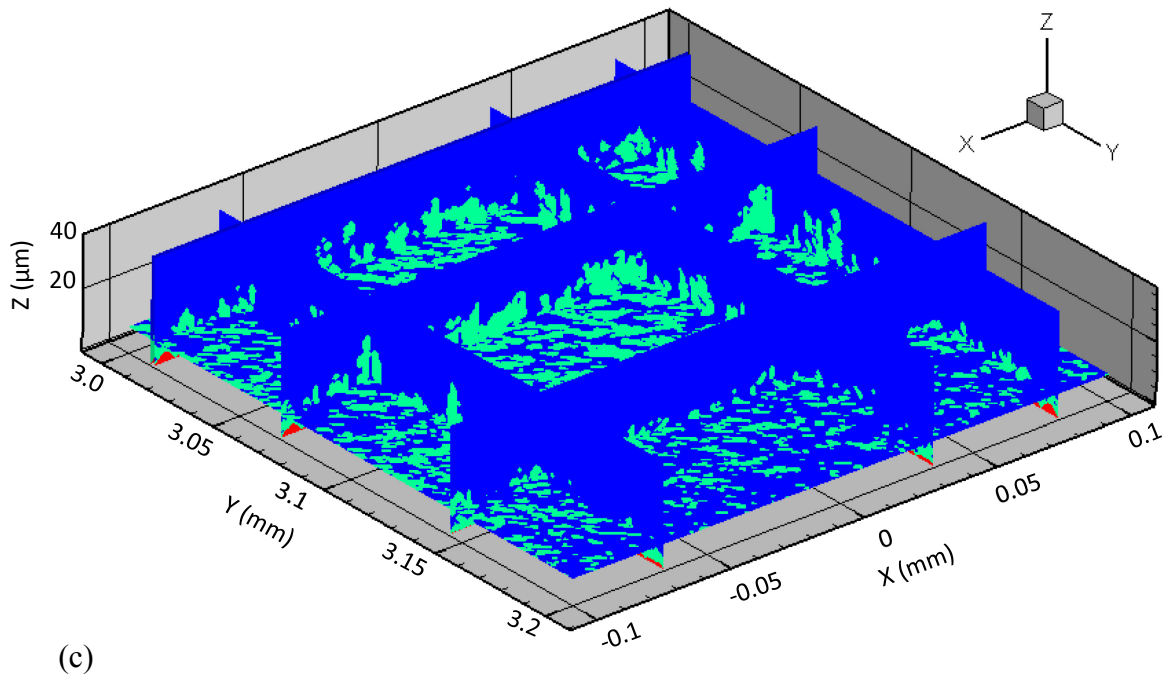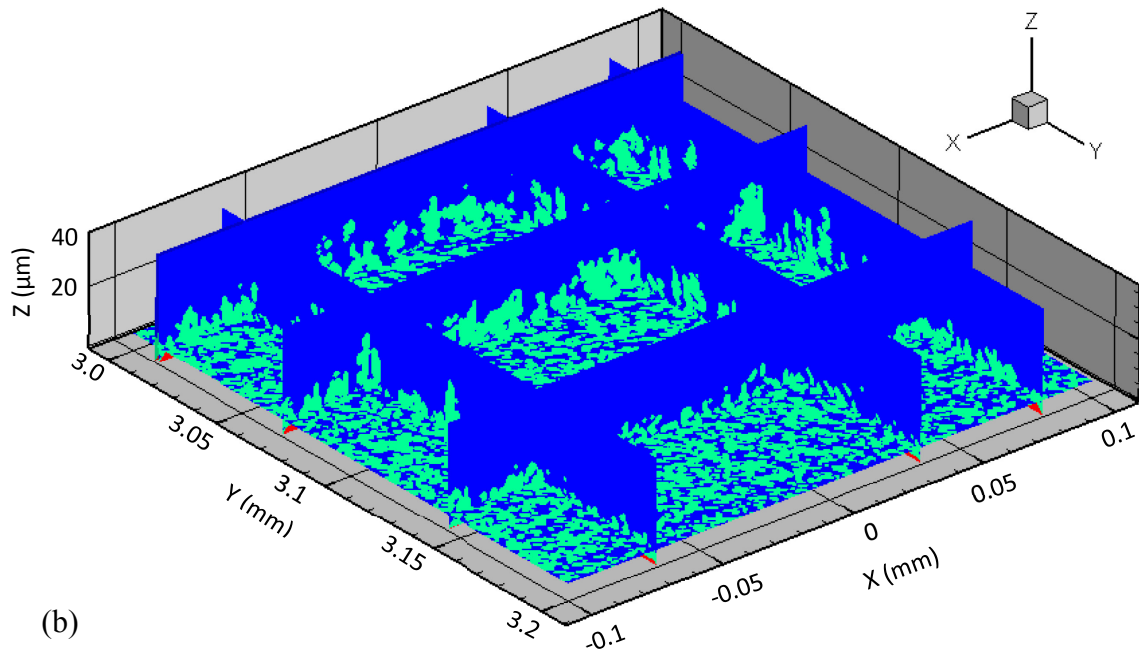
Figure 3-11 Horizontal cross-section view of coating structure at (a) 4 µm (b) 6 µm (c) 9 µm for thirty two passes.

4 Conclusion and Future Work

The suspension plasma spray microstructure involves extremely complicated phenomena with various influential parameters. Thus, various microstructures can be obtained, depending on the suspension interactions with the plasma plume, deposition situation, powder types, solid concentration in suspension, substrate preparation method, plasma spray setup, spray distance, powder feed rate, and some other factors. Furthermore, making a controlled structure with desirable characteristics requires thorough studies of different cases. It was proven that conducting experiments is a time and cost consuming process. Hence, a coating build-up simulation as one of the subsets of experimental trails enables us to save the time and money as well as increasing the accuracy of our work. It also could predict coatings quality and modify coating parameters for the specific application. It is of great interest to simulate the SPS microstructure within the context of these parameters. Therefore, in the first step in SPS coating build-up simulation, a three dimensional computational code was developed to capture and predict the columnar structure observed in SPS coatings.

In this work, the impact property values of each particle are obtained from a computational fluid dynamics (CFD) simulation of a radial suspension injection into a Metco-3MB plasma gun conducted by Pourang et al. [14]. Then, the trajectory of each particle upon the impact is calculated to determine the final location of an impinged particle on the substrate or previously deposited particles. It is assumed that particles stick to the impinging location based on the prescribed scenarios. The coating structure is specified using a variable known as the $f_{i,j,k}$ which is zero once the cell is empty and equals unity when the cell is filled with the coating material.

The model predicts a rather uniform thickness for 10 passes in both x and y-directions for 200*200 μm^2 area near the plasma torch center line and 3 mm in the +y-direction. However, it is not uniform for 32 passes. The columnar structures evolve in the y-direction from right to left. The predicted trends are consistent with the experimental results since the injection penetrates in plasma radially in z-direction from the top and the small particles mostly deviate and follow the trajectory of plasma and impact with the oblique angle.

The phenomena involved in suspension plasma spraying process is vast and complex. Therefore, predicting the coatings structure is intensely controversial and difficult. The results in this research are obtained through a preliminary study that shows the columnar structure. However, we made few assumptions based on phenomena involved in suspension plasma spraying and deposition mechanism process. The spreading and solidification of particle after impact is neglected. Also, the particle size is assumed uniform and $f_{i,j,k}$ takes only a value of zero or one. Additionally, the number of selected particles from pool per time step are considered constant. These assumptions result in less column width compared to actual one and also less precise porosity in the structure. It is notable to mention that although the aforementioned assumptions are made to simplify the complex phenomena and decrease the computational time, time is still a major challenge for this study. In fact, these assumptions enable us to come up with reasonable solution and make it more appealing and precise by considering further steps in simulation. It would be interesting to expand this research for future investigations such as:

- Decreasing the computational time.
- Considering the effect of spreading and solidification. In this research, it is assumed that particles stick to impinged location with uniform shape.

- Refining the mesh size and defining $f_{i,j,k}$ value between zero and one will give more precise result compared to merely zero or one in our case.

- Investigating various particle sizes as another improving factor in SPS coating.

- Coating modelling using a full scan gun movement rather than a one-direction linear gun movement.

- Varying number of selected particles from pool per time step considering gun location.

References

[1] P. L. Fauchais, J. V. R. Heberlein, and M. I. Boulos, "*Thermal Spray Fundamentals,*" *Springer Science, Business Media, pp* 452, 2014

[2] J. R. Davis, "Introduction to Thermal Spray Processing," in *Handbook. Therm. Spray Technol.*, pp. 3–13, 2004.

[3] P. Fauchais and A. Vardelle, "Thermal Sprayed Coatings Used Against Corrosion and Corrosive Wear," *Adv. Plasma Spray Appl.*, pp. 3–38, 2012.

[4] W. Fan and Y. Bai, "Review of suspension and solution precursor plasma sprayed thermal barrier coatings," *Ceram. Int.*, vol. 42, no. 13, pp. 14299–14312, 2016.

[5] A. Ganvir, N. Curry, N. Markocsan, P. Nylén, and F. L. Toma, "Comparative study of suspension plasma sprayed and suspension high velocity oxy-fuel sprayed YSZ thermal barrier coatings," *Surf. Coatings Technol.*, vol. 268, pp. 70–76, 2015.

[6] P. Fauchais, R. Etchart-Salas, V. Rat, J. F. Coudert, N. Caron, and K. Wittmann-Ténèze, "Parameters controlling liquid plasma spraying: Solutions, sols, or suspensions," *J. Therm. Spray Technol.*, vol. 17, no. 1, pp. 31–59, 2008.

[7] O. Rezania, "Anelastic Behavior of Suspension Plasma Sprayed Ceramic Coatings," Master Thesis, Concordia University, 2016.

[8] H. Kassner, R. Siegert, D. Hathiramani, R. Vassen, and D. Stoever, "Application of suspension plasma spraying (SPS) for manufacture of ceramic coatings," *J. Therm. Spray Technol.*, vol. 17, no. 1, pp. 115–123, 2008.

[9] L. Pawlowski, "Suspension and solution thermal spray coatings," *Surf. Coatings Technol.*, vol. 203, no. 19, pp. 2807–2829, 2009.

[10] B. Bernard, L. Bianchi, A. Malié, A. Joulia, and B. Rémy, "Columnar suspension plasma sprayed coating microstructural control for thermal barrier coating application," *J. Eur. Ceram. Soc.*, vol. 36, no. 4, pp. 1081–1089, 2016.

[11] F. Tarasi, M. Medraj, A. Dolatabadi, J. Oberste-Berghaus, and C. Moreau, "Effective parameters in axial injection suspension plasma spray process of alumina-zirconia ceramics," *J. Therm. Spray Technol.*, vol. 17, no. 5–6, pp. 685–691, 2008.

[12] G. Mauer, R. Vaßen, and D. Stöver, "Comparison and applications of DPV-2000 and accuraspray-g3 diagnostic systems," *J. Therm. Spray Technol.*, vol. 16, no. 3, pp. 414–424, 2007.

[13] M. Jadidi, M. Mousavi, S. Moghtadernejad, and A. Dolatabadi, "A Three-Dimensional Analysis of the Suspension Plasma Spray Impinging on a Flat Substrate," *J. Therm. Spray Technol.*, vol. 24, no. 1–2, pp. 11–23, 2014.

[14] K. Pourang, C. Moreau, and A. Dolatabadi, "Effect of Substrate and Its Shape on in-Flight Particle Characteristics in Suspension Plasma Spraying," *J. Therm. Spray Technol.*, vol.

25, no. 1–2, pp. 44–54, 2016.

[15]   E. Moreau, C. Chazelas, G. Mariaux, and A. Vardelle, "Modeling the Restrike Mode Operation of a DC Plasma Spray Torch," *J. Therm. Spray Technol.*, vol. 15, no. 4, pp. 524–530, 2006.

[16]   E. Meillot, D. Guenadou, and C. Bourgeois, "Three-dimension and transient D.C. Plasma flow modeling," *Plasma Chem. Plasma Process.*, vol. 28, no. 1, pp. 69–84, 2008.

[17]   K. Remesh, S. C. M. Yu, H. W. Ng, and C. C. Berndt, "Computational Study and Experimental Comparison of the In-Flight Particle Behavior for an External Injection Plasma Spray Process," *J. Therm. Spray Technol.*, vol. 12, no. 4, pp. 508–522, 2003.

[18]   Y. Shan, T. W. Coyle, and J. Mostaghimi, "Numerical simulation of droplet breakup and collision in the solution precursor plasma spraying," *J. Therm. Spray Technol.*, vol. 16, no. 5–6, pp. 698–704, 2007.

[19]   S. Vincent, G. Balmigere, C. Caruyer, E. Meillot, and J. P. Caltagirone, "Contribution to the modeling of the interaction between a plasma flow and a liquid jet," *Surf. Coatings Technol.*, vol. 203, no. 15, pp. 2162–2171, 2009.

[20]   F. Jabbari, M. Jadidi, R. Wuthrich, and A. Dolatabadi, "A numerical study of suspension injection in plasma-spraying process," *J. Therm. Spray Technol.*, vol. 23, no. 1–2, pp. 3–13, 2014.

[21]   C. W. Kang, H. W. Ng, and S. C. M. Yu, "Comparative study of plasma spray flow fields and particle behavior near to flat inclined substrates," *Plasma Chem. Plasma Process.*, vol. 26, no. 2, pp. 149–175, 2006.

[22]   A. M. Worthington, "On the Forms Assumed by Drops of Liquids Falling Vertically on a Horizontal Plate.," *Proc. R. Soc. London*, vol. 25, no. 171–178, pp. 498–503, 1876.

[23]   S. T. Thoroddsen, T. G. Etoh, K. Takehara, N. Ootsuka, and Y. Hatsuki, "The air bubble entrapped under a drop impacting on a solid surface," *J. Fluid Mech.*, vol. 545, p. 203, 2005.

[24]   M. J. Thoraval, K. Takehara, T. G. Etoh, S. Popinet, P. Ray, C. Josserand, S. Zaleski, and S. T. Thoroddsen, "Von Karman vortex street within an impacting drop," *Phys. Rev. Lett.*, vol. 108, no. 26, pp. 1–5, 2012.

[25]   C. Josserand and S. T. Thoroddsen, "Drop Impact on a Solid Surface," *Annu. Rev. Fluid Mech.*, vol. 48, no. 1, pp. 365–391, 2016.

[26]   K. Yang, M. Liu, K. Zhou, and C. Deng, "Recent Developments in the Research of Splat Formation Process in Thermal Spraying," *J. Mater.*, vol. 2013, pp. 1–14, 2013.

[27]   C. Mundo, M. Sommerfeld, and C. Tropea, "Droplet-wall collisions: Experimental studies of the deformation and breakup process," *Int. J. Multiph. Flow*, vol. 21, no. 2, pp. 151–173, 1995.

[28]   M. Fukumoto, E. Nishioka, and T. Matsubara, "Flattening and solidification behavior of a

metal droplet on a flat substrate surface held at various temperatures," *Surf. Coatings Technol.*, vol. 120–121, pp. 131–137, 1999.

[29] M. Fukumoto, E. Nishioka, and T. Nishiyama, "The criterion for splashing in flattening of thermal sprayed particles onto flat substrate surface," *Surf. Coatings Technol.*, vol. 161, no. 2–3, pp. 103–110, 2002.

[30] I. V. Roisman, R. Rioboo, and C. Tropea, "Normal impact of a liquid drop on a dry surface: model for spreading and receding," *Proc. R. Soc. A Math. Phys. Eng. Sci.*, vol. 458, no. 2022, pp. 1411–1430, 2002.

[31] D. Bartolo, C. Josserand, and D. Bonn, "Retraction dynamics of aqueous drops upon impact on non-wetting surfaces," *J. Fluid Mech.*, vol. 545, no. 1, p. 329, 2005.

[32] D. Bartolo, C. Josserand, and D. Bonn, "Singular jets and bubbles in drop impact," *Phys. Rev. Lett.*, vol. 96, no. 12, pp. 1–4, 2006.

[33] I. S. BAYER and C. M. MEGARIDIS, *Contact angle dynamics in droplets impacting on flat surfaces with different wetting characteristics*, vol. 558. 2006.

[34] A. Antkowiak, B. Audoly, C. Josserand, S. Neukirch, and M. Rivetti, "Instant fabrication and selection of folded structures using drop impact," *Proc. Natl. Acad. Sci.*, vol. 108, no. 26, pp. 10400–10404, 2011.

[35] G. Lagubeau, M. A. Fontelos, C. Josserand, A. Maurel, V. Pagneux, and P. Petitjeans, "Spreading dynamics of drop impacts," *J. Fluid Mech.*, vol. 713, pp. 50–60, 2012.

[36] S. Chandra and C. T. Avedisian, "On the Collision of a Droplet with a Solid Surface," *Proc. R. Soc. A Math. Phys. Eng. Sci.*, vol. 432, no. 1884, pp. 13–41, 1991.

[37] M. Pasandideh-Fard, Y. M. Qiao, S. Chandra, and J. Mostaghimi, "Capillary effects during droplet impact on a solid surface," *Phys. Fluids*, vol. 8, no. 3, pp. 650–659, 1996.

[38] K. Range and F. Feuillebois, "Influence of Surface Roughness on Liquid Drop Impact," *J. Colloid Interface Sci.*, vol. 203, no. 1, pp. 16–30, 1998.

[39] C. Clant, C. Beguni, D. Richard, and D. Quere, "Maximal deformation of an impacting drop," *J. Fluid Mech.*, vol. 517, pp. 199–208, 2004.

[40] A. I. Fedorchenko, A. B. Wang, and Y. H. Wang, "Effect of capillary and viscous forces on spreading of a liquid drop impinging on a solid surface," *Phys. Fluids*, vol. 17, no. 9, pp. 1–8, 2005.

[41] C. Ukiwe and D. Y. Kwok, "On the maximum spreading diameter of impacting droplets on well-prepared solid surfaces," *Langmuir*, vol. 21, no. 2, pp. 666–673, 2005.

[42] I. V. Roisman, "Inertia dominated drop collisions. II. An analytical solution of the Navier-Stokes equations for a spreading viscous film," *Phys. Fluids*, vol. 21, no. 5, 2009.

[43] D. C. Vadillo, A. Soucemarianadin, C. Delattre, and D. C. D. Roux, "Dynamic contact angle effects onto the maximum drop impact spreading on solid surfaces," *Phys. Fluids*, vol. 21, no. 12, pp. 1–8, 2009.

[44] J. Eggers, M. A. Fontelos, C. Josserand, and S. Zaleski, "Drop dynamics after impact on a solid wall: Theory and simulations," *Phys. Fluids*, vol. 22, no. 6, 2010.

[45] J. Madejski, "Solidification of droplets on a cold surface," *Int. J. Heat Mass Transf.*, vol. 19, no. 9, pp. 1009–1013, 1976.

[46] P. Sokolowski, S. Kozerski, L. Pawlowski, and A. Ambroziak, "The key process parameters influencing formation of columnar microstructure in suspension plasma sprayed zirconia coatings," *Surf. Coatings Technol.*, vol. 260, pp. 97–106, 2014.

[47] R. C. Seshadri, G. Dwivedi, V. Viswanathan, and S. Sampath, "Characterizing Suspension Plasma Spray Coating Formation Dynamics through Curvature Measurements," *J. Therm. Spray Technol.*, vol. 25, no. 8, pp. 1666–1683, 2016.

[48] S. Wutzke, E. Pfender, and E. Eckert, "Study of electric arc behavior with superimposed flow," *AIAA J.*, vol. 5, no. 4, pp. 707–714, 1967.

[49] J. P. Trelles, E. Pfender, and J. V. R. Heberlein, "Modelling of the arc reattachment process in plasma torches," *J. Phys. D. Appl. Phys.*, vol. 40, no. 18, pp. 5635–5648, 2007.

[50] W. D. Cai and E. J. Lavernia, "Modeling of porosity during spray forming," *Mater. Sci. Eng. A*, vol. 226–228, pp. 8–12, 1997.

[51] H. Fukanuma, "A porosity formation and flattening model of an impinging molten particle in thermal spray coatings," *J. Therm. Spray Technol.*, vol. 3, no. 1, pp. 33–44, 1994.

[52] R. Elsing, "Monte carlo simulation of the lamellar structure of thermally sprayed coatings," vol. 32, pp. 261–271, 1987.

[53] S. Cirolini, J. H. Harding, and G. Jacucci, "Computer simulation of plasma-sprayed coatings I. Coating deposition model," *Surf. Coatings Technol.*, vol. 48, no. 2, pp. 137–145, 1991.

[54] J. H. Harding, P. A. Mulheran, S. Cirolini, M. Marchese, and G. Jacucci, "Modeling the Deposition Process of Thermal Barrier Coatings," vol. 4, no. March, pp. 34–40, 1995.

[55] M. P. Kanouff, R. a. Neiser Jr, and T. J. Roemer, "Surface Roughness of Thermal Spray Coatings Made with Off-Normal Spray Angles," *J. Therm. Spray Technol.*, vol. 7, no. June, pp. 219–228, 1998.

[56] A. Hansbo and P. Nylen, "Models for the simulation of spray deposition and robot motion optimization\r\nin thermal spraying of rotating objects," *Surf. Coatings Technol.*, vol. 122, pp. 191–201, 1999.

[57] R. Ghafouri-Azar, J. Mostaghimi, S. Chandra, and M. Charmchi, "A Stochastic Model to Simulate the Formation of a Thermal Spray Coating," *J. Therm. Spray Technol.*, vol. 12, no. March, pp. 53–69, 2003.

[58] J. Mostaghimi, S. Chandra, and A. Dolatabadi, "Modeling thermal spray coating processes : a powerful tool in design and optimization," *Surf. Coatings Technol.*, vol. 164, pp. 1–11, 2003.

[59] M. Xue, S. Chandra, J. Mostaghimi, and C. Moreau, "A stochastic coating model to predict the microstructure of plasma sprayed zirconia coatings," *Model. Simul. Mater. Sci. Eng.*, vol. 16, no. 6, 2008.

[60] S. D. Aziz and S. Chandra, "Impact, recoil and splashing of molten metal droplets," *Int. J. Heat Mass Transf.*, vol. 43, no. 16, pp. 2841–2857, 2000.

[61] S. Beauvais, V. Guipont, M. Jeandin, D. Jeulin, A. Robisson, and R. Saenger, "Study of the porosity in plasma-sprayed alumina through an innovative three-dimensional simulation of the coating buildup," *Metall. Mater. Trans. A Phys. Metall. Mater. Sci.*, vol. 39, no. 11, pp. 2711–2724, 2008.

[62] T. Wiederkehr and H. Müller, "Efficient Large-Scale Coating Microstructure Formation Using Realistic CFD Models," *J. Therm. Spray Technol.*, vol. 24, no. 3, pp. 283–295, 2014.

[63] T. Merkh, R. Spivey, and T. M. Lu, "Time Invariant Surface Roughness Evolution during Atmospheric Pressure Thin Film Depositions," *Sci. Rep.*, vol. 6, pp. 1–6, 2016.

[64] K. Vanevery, M. J. M. Krane, R. W. Trice, H. Wang, W. Porter, M. Besser, D. Sordelet, J. Ilavsky, and J. Almer, "Column formation in suspension plasma-sprayed coatings and resultant thermal properties," *J. Therm. Spray Technol.*, vol. 20, no. 4, pp. 817–828, 2011.

5 Appendix A

In this section the flowchart and some of the developed codes are presented.

5.1 **The key steps in the coating build-up simulation**

The implementation is demonstrated in detail through a flowchart shown in Figure 5-1.

Define different scenarios

- U<0 , V<0 , 0≤α<30
- U<0 , V<0 , 30≤α≤60
- U<0 , V<0 , 60<α≤90
- U>0 , V>0 , 0≤α<30
- U>0 , V>0 , 30≤α≤60
- U>0 , V>0 , 60<α≤90
- U>0 , V<0 , 0≤α<30
- U>0 , V<0 , 30≤α≤60
- U>0 , V<0 , 60<α≤90
- U<0 , V>0 , 0≤α<30
- U<0 , V>0 , 30≤α≤60
- U<0 , V>0 , 60<α≤90

Velocity in
x and y
directions
& α angle

- 0≤θ<30
- 30≤θ≤60
- 60<θ≤90

$h(i,j) = h_{impact}$

Coating
thickness &
landing cell
height

$h(i,j) > h_{impact}$

- 0≤θ<45
- 45≤θ≤90

$f_{i,j,k} = 1$

Saving the output
matrix to plot
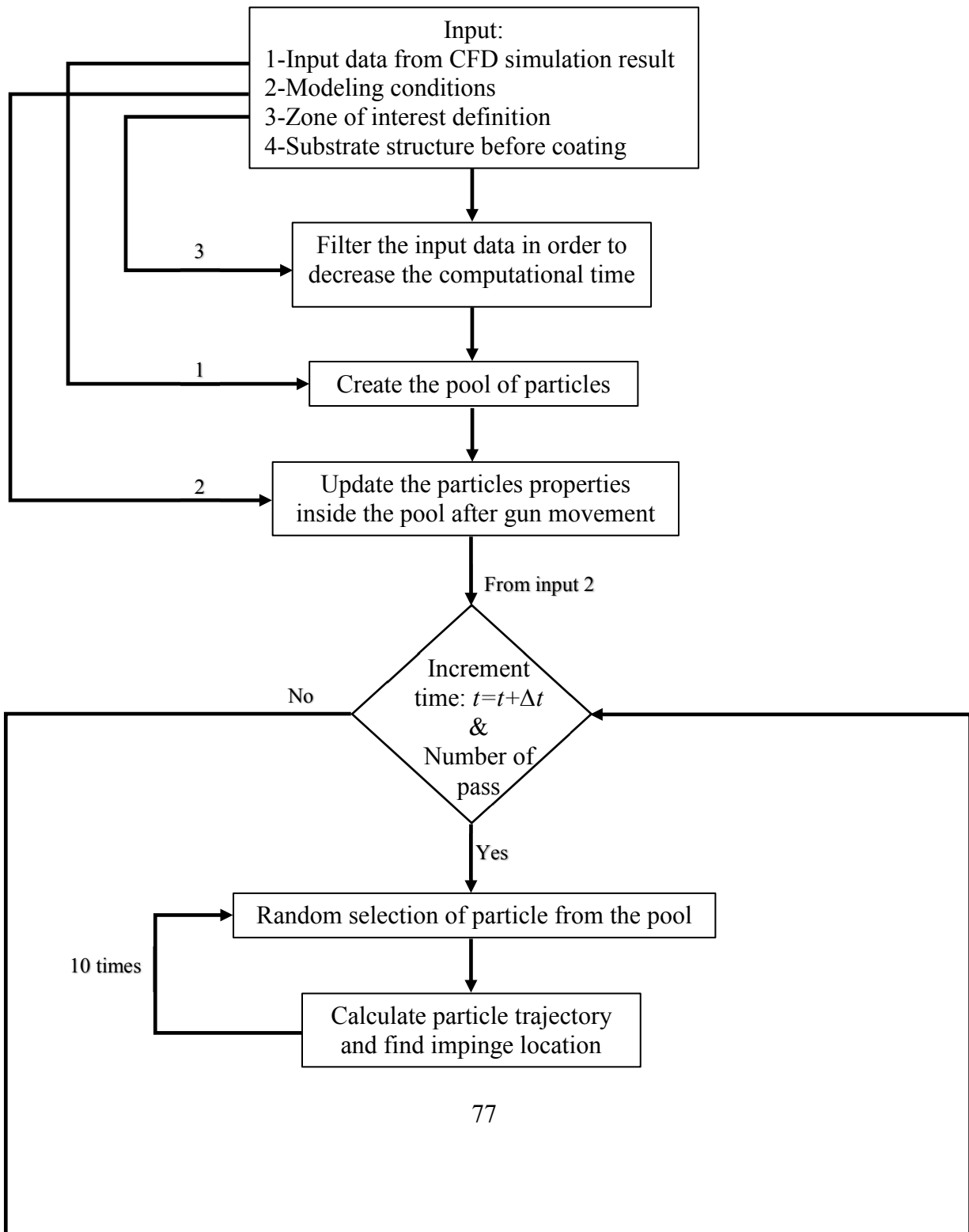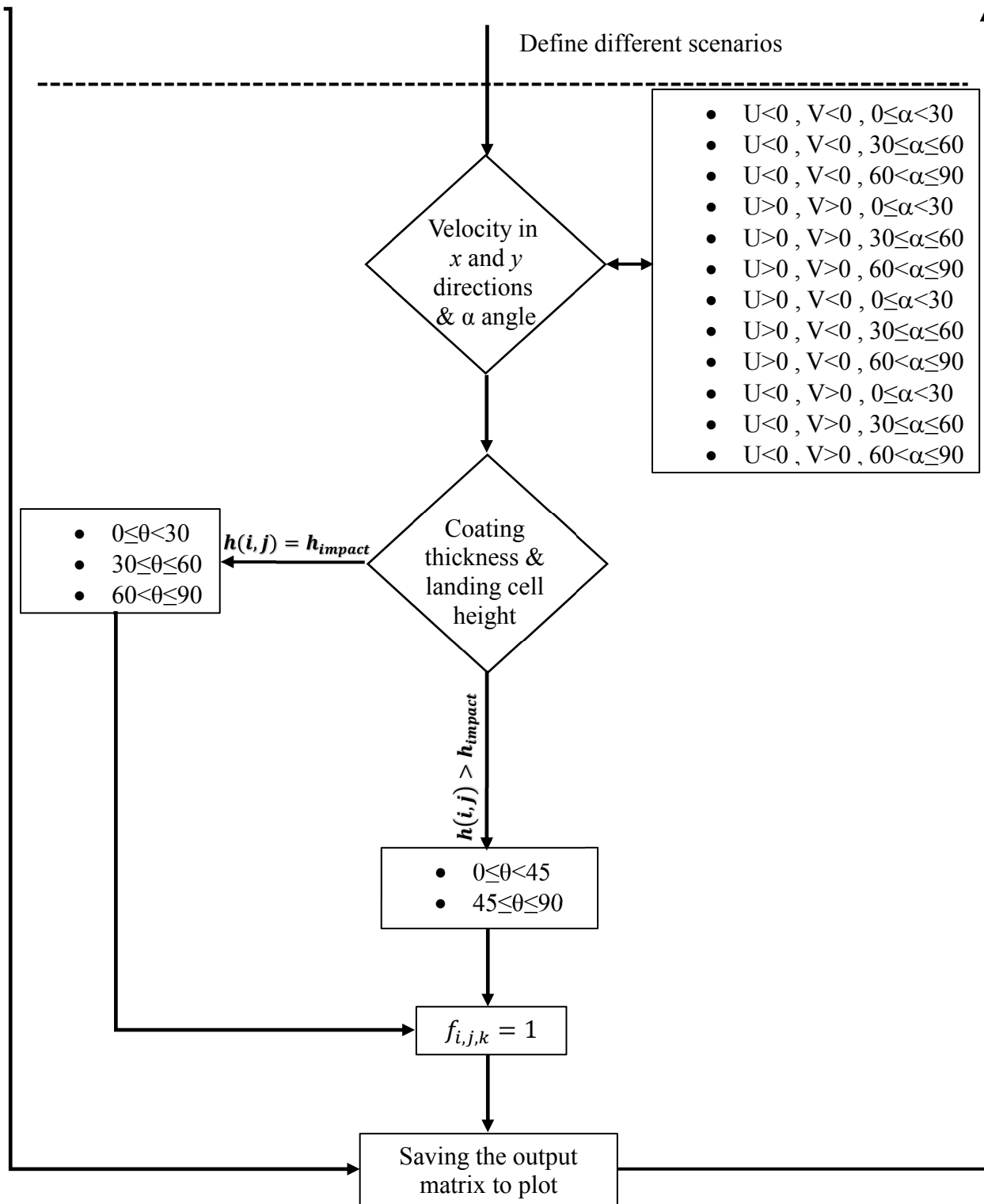
Figure 5-1. The key steps in the coating build-up simulation.

5.2 SPS Coating build-up Matlab code:

```matlab
%*************************************************************************
%*********************Input data from CDF simulation result *************
%*************************************************************************
filename='montecarlo10.xlsx';
sheet=1;
XlRange='A2:A2504';
YlRange='B2:B2504';
SL1lRange='AD2:AD2504';
SL2lRange='AE2:AE2504';
omegalRange='G2:G2504';
tetaalRange='K2:K2504';
ulRange='L2:L2504' ;
vlRange='M2:M2504';
wlRange='N2:N2504';
vellRange='T2:T2504';
dlRange='O2:O2504';
rptlRange='Q2:Q2504';
imptlRange='W2:W2504';
numx0 = xlsread(filename,sheet,XlRange);
numy0 = xlsread(filename,sheet,YlRange);
slope10 = xlsread(filename,sheet,SL1lRange);
slope20 = xlsread(filename,sheet,SL2lRange);
numomega0 = xlsread(filename,sheet,omegalRange);
numtetaa0 = xlsread(filename,sheet,tetaalRange);
numu0 = xlsread(filename,sheet,ulRange);
numv0 = xlsread(filename,sheet,vlRange);
numw0 = xlsread(filename,sheet,wlRange);
numvel0 = xlsread(filename,sheet,vellRange);
numd0 = xlsread(filename,sheet,dlRange);
numrpt0= xlsread(filename,sheet,rptlRange);
numimpt0= xlsread(filename,sheet,imptlRange);
%*************************************************************************
%**************** Modeling conditions and computational domain **********
%*************************************************************************
cxs=1e-06;                  %grid size
cys=1e-06;                  %grid size
czs=1e-06;                  %grid size
resolution=1e-06;           %computational domain
cxry=cxs/cys;               %computational domain
rrcx=resolution/cxs;        %computational domain
rate=10;                    %deposition rate;
np2=70;                     %number of pass
delt=.000001;               %time step
velg=1;                     %gum velocity (m/s)
LS=.025;                    %substrate length (m)
np1=(LS/(2*velg))/delt;     %number of iteration
%*************************************************************************
%**************** Modeling conditions and computational domain *********
%*************************************************************************
lim1=-0.3 mm;
lim2=0.3 mm;
lim3=-0.1 mm;
lim4=0.1 mm;
lim5=2.8 mm;
lim6=3.4 mm;
lim7=3.0 mm;
lim8=3.2 mm;
%*************************************************************************
%******************* Substrate structure before coating ***************
%*************************************************************************
rxs=rrcx*10;
for n1=0:rxs-2:(lim2-lim1+1)+200
```

```matlab
      for n2=0:rxs-2:(lim6-lim5+1)+200
        for i=1:rxs/2
          for ii=1:rxs/2
          h(n1+i,n2+ii)=cxry*czs*min(i,ii);
          for sub1= h(n1+i,n2+ii):-czs:czs
          h1(n1+i,n2+ii)=round(sub1/czs);
          hit(n1+i,n2+ii, h1(n1+i,n2+ii))=2;
          end
          if i<5 || ii<5
          h(n1+rxs-i,n2+ii)=cxry*czs*min(i,ii);
          for sub3= h(n1+rxs-i,n2+ii):-czs:czs
          h1(n1+rxs-i,n2+ii)=round(sub3/czs);
          hit(n1+rxs-i,n2+ii, h1(n1+rxs-i,n2+ii))=2;
          end
          h(n1+i,n2+rxs-ii)=cxry*czs*min(i,ii);
          for sub2= h(n1+i,n2+rxs-ii):-czs:czs
          h1(n1+i,n2+rxs-ii)=round(sub2/czs);
          hit(n1+i,n2+rxs-ii, h1(n1+i,n2+rxs-ii))=2;
          end
          h(n1+rxs-i,n2+rxs-ii)=cxry*czs*min(i,ii);
          for sub4= h(n1+rxs-i,n2+rxs-ii):-czs:czs
          h1(n1+rxs-i,n2+rxs-ii)=round(sub4/czs);
          hit(n1+rxs-i,n2+rxs-ii, h1(n1+rxs-i,n2+rxs-ii))=2;
          end
           end
          end
       end
     end
end

% ****************************************************************************
% ***************************** Input data filtering ***********************
% ****************************************************************************

for slct0=1:rng0
ffdy=ceil(DATA0(slct0,2)/cys);
if  ffdy>lim5 && ffdy<lim6
    DATA01=[DATA0(slct0,1) DATA0(slct0,2) DATA0(slct0,3) DATA0(slct0,4) DATA0(slct0,5) DATA0(slct0,6)
DATA0(slct0,7) DATA0(slct0,8) DATA0(slct0,9) DATA0(slct0,10)  DATA0(slct0,11) ];
else
    DATA01=[];
end
DATA02=[DATA02;DATA01];
end
% ****************************************************************************
% ***************************** Pool of particles ***************************
% ****************************************************************************
numx  =cell2mat(arrayfun(@(x, y) repmat(x, [1 y]), DATA2(:,1)',DATA2(:,11)', 'UniformOutput', false));
numx=numx';
numy= cell2mat(arrayfun(@(x, y) repmat(x, [1 y]), DATA2(:,2)',DATA2(:,11)', 'UniformOutput', false));
numy=numy';
slope1= cell2mat( arrayfun(@(x, y) repmat(x, [1 y]),DATA2(:,6)',DATA2(:,11)', 'UniformOutput', false));
slope1=slope1';
slope2= cell2mat(arrayfun(@(x, y) repmat(x, [1 y]), DATA2(:,7)',DATA2(:,11)', 'UniformOutput', false));
slope2=slope2';
numu= cell2mat(arrayfun(@(x, y) repmat(x, [1 y]),  DATA2(:,8)',DATA2(:,11)', 'UniformOutput', false));
numu=numu';
numv =cell2mat(arrayfun(@(x, y) repmat(x, [1 y]),  DATA2(:,9)',DATA2(:,11)', 'UniformOutput', false));
numv=numv';
numw = cell2mat(arrayfun(@(x, y) repmat(x, [1 y]), DATA2(:,10)',DATA2(:,11)', 'UniformOutput', false));
numw=numw';
numd = cell2mat(arrayfun(@(x, y) repmat(x, [1 y]), DATA2(:,5)',DATA2(:,11)', 'UniformOutput', false));
numd=numd';
numimpt=cell2mat(arrayfun(@(x, y)repmat(x, [1 y]), DATA2(:,3)', DATA2(:,11)', 'UniformOutput', false));
numimpt=numimpt';
numvel= cell2mat(arrayfun(@(x, y) repmat(x, [1 y]), DATA2(:,4)',DATA2(:,11)', 'UniformOutput', false));
numvel=numvel';
```

```
DATA=[numx numy numimpt numvel numd slope1 slope2 numu numv numw];
*******************************************************************************
* Update the particles properties inside the pool after gun movement *
*******************************************************************************
for slct=1:rng02

dom01=ceil(DATA02(slct,1)/cxs);
 if mod(k1,2)==1
   dom1=dom01+((velg*delt*k2)/cxs);
 else
   dom1=dom01+((velg*delt*k2)/cxs)-(LS/2)*1000000;
 end

dom2=ceil(DATA02(slct,2)/cys);
if dom1>lim1 && dom1<lim2 && dom2>lim5 && dom2<lim6
    DATA1=[round(dom1) round(dom2) DATA02(slct,3) DATA02(slct,4) DATA02(slct,5) DATA02(slct,6)
DATA02(slct,7) DATA02(slct,8) DATA02(slct,9) DATA02(slct,10) DATA02(slct,11) DATA02(slct,1) DATA02(slct,2)
];

else
    DATA1=[];
end
DATA2=[DATA2;DATA1];
end
*******************************************************************************
***************** Random selection of particle from the pool***********
*******************************************************************************
Pool=round((1+(rng2-1)*rand(t_max,rate)));
for con=1:t_max
  for  con1=1:rate
    A11=round((0+(.0002-0)*rand(1))/cxs);
    AA11=round((0+(.0002-0)*rand(1))/cys);
    A(con,con1)=round(DATA(Pool(con,con1),1))+A11;
    AA(con,con1)=round(DATA(Pool(con,con1),2))+AA11;
    B(con,con1)=DATA(Pool(con,con1),3);
    VL(con,con1)=DATA(Pool(con,con1),4);
    DD(con,con1)=DATA(Pool(con,con1),5);
    slp1(con,con1)=DATA(Pool(con,con1),6);
    slp2(con,con1)=DATA(Pool(con,con1),7);
    VLu(con,con1)=DATA(Pool(con,con1),8);
    VLv(con,con1)=DATA(Pool(con,con1),9);
    VLw(con,con1)=DATA(Pool(con,con1),10);
    dddd=[dddd,A(con,con1)];
    dddd8=[dddd8,AA(con,con1)];
    dddd1=[dddd1,B(con,con1)];
    dddd2=[dddd2,VL(con,con1)];
    dddd3=[dddd3,DD(con,con1)];
    dddd9=[dddd9,slp1(con,con1)];
    dddd10=[dddd10,slp2(con,con1)];
    dddd11=[dddd11,VLu(con,con1)];
    dddd12=[dddd12,VLv(con,con1)];
    dddd13=[dddd13,VLw(con,con1)];

    end
end


*******************************************************************************
*********Particle trajectory calculation and impinge location *********
*******************************************************************************
z0=max(h(:))+.0001;
z1=-SL1*(x-i)+(z0/czs);
z1=vpa(z1);
y1=-SL2*(x-i)+ii;
y1=vpa(y1);

if    VeLu<0
```

81

```
for i1=i:-1:lim1
x=i1;
yin=subs(y1);
yin=round(yin);
xin=x;
if yin<lim6 && yin>lim5
zin=subs(z1);
if zin<=h(xin,yin) && zin>=0
h3(xin,yin)=ceil(zin/czs);
if hit(xin,yin,h3(xin,yin))==1
    zin=ceil(zin /czs)*czs;
    break
 end
elseif zin<0
 x=floor(feval(symengine,'numeric::solve',z1==0,x,'AllRealRoots'));
 yin=subs(y1);
 yin=round(yin);
 xin=x;
 zin=h(xin,yin);
break
end
end
end


*****************************************************************************
******* Scenario (One specific condition) – U<0 & V<0 & 60°<α≤90°*****
*****************************************************************************
if VeLu<0 && VeLv<0 && abs(SL2)>=1.7321

    if  (h(xin,yin)-zin) = 0

     if j<30 && j>=0

       if h(xin,yin+1)>h(xin,yin)
       h(xin,yin+1)=h(xin,yin+1)+czs;
       h1(xin,yin+1)= round(h(xin,yin+1)/czs);
       hit(xin,yin+1,h1(xin,yin+1)) = 1;
       elseif h(xin,yin+1)==h(xin,yin)
       h(xin,yin)=h(xin,yin)+czs;
       h1(xin,yin)= round(h(xin,yin)/czs);
       hit(xin,yin,h1(xin,yin)) = 1;
       else
       h(xin,yin+1)=h(xin,yin);
       h1(xin,yin+1)= round(h(xin,yin+1)/czs);
       hit(xin,yin+1,h1(xin,yin+1)) = 1;
       end

     elseif j>=30 && j<=60

       if h(xin,yin+1)>h(xin,yin)
       h(xin,yin+1)=h(xin,yin+1)+czs;
       else
       h(xin,yin+1)=h(xin,yin)+czs;
       end
       h1(xin,yin+1)= round(h(xin,yin+1)/czs);
       hit(xin,yin+1,h1(xin,yin+1)) = 1;

     elseif j>60 && j<=90

       h(xin,yin) =h(xin,yin)+czs;
       h1(xin,yin)= round(h(xin,yin)/czs);
       hit(xin,yin,h1(xin,yin)) = 1;
     end

    elseif (h(xin,yin)-zin)> czs

 if j<=45 && j>=0
```

```matlab
    if h(xin,yin+1)<=zin
    if abs(h(xin,yin+1)- zin) <= czs
    h(xin,yin+1)=h(xin,yin+1)+czs;
    else
    h(xin,yin+1)=zin;
    end
    h1(xin,yin+1)= round(h(xin,yin+1)/czs);
    hit(xin,yin+1,h1(xin,yin+1)) = 1;
    elseif h(xin,yin+1)>zin
    h1(xin,yin+1)= round(zin/czs);
    hit(xin,yin+1,h1(xin,yin+1)) = 1;
    end

 elseif j<=90 && j>45

    if h(xin,yin+1)<=zin
    if abs(h(xin,yin+1)- zin) <= czs
    h(xin,yin+1)=h(xin,yin+1)+czs;
    else
    h(xin,yin+1) =zin+czs;
    end
    h1(xin,yin+1)= round(h(xin,yin+1)/czs);
    hit(xin,yin+1,h1(xin,yin+1)) = 1;
    elseif h(xin,yin+1)>zin
    h1(xin,yin+1)= round((zin+czs)/czs);
    hit(xin,yin+1,h1(xin,yin+1)) = 1;
    end
 end
    end
%*****************************************************************************
%********************** Saving the result matrix *************************
%*****************************************************************************
if mod(k1,2)==0
for iatom=201:401
  for jatom=201:401
   for zatom=max(h(:)):-czs:czs
      z1atom=round(zatom/czs);
      result1=hit(iatom,jatom,z1atom);
      result2=[iatom  jatom z1atom result1];
      result3=[result3;result2];
   end
  end
end
 save(['solution_number',num2str(k1),'.mat'],'result3');
```

83